

High field investigations into the electronic state of unconventional superconductors

August 29, 2012

Brendan James Arnold

A dissertation submitted to the University of Bristol in accordance with the requirements for award of the degree of Doctor in Philosophy in the Faculty of Science, School of Physics

Abstract

TODO: (Write an abstract)

Acknowledgements

TODO: (Write acknowledgements)

Declaration

I declare that the work in this dissertation was carried out in accordance with the requirements of the University's Regulations and Code of Practice for Research Degree Programmes and that it has not been submitted for any other academic award. Except where indicated by specific reference in the text, the work is the candidate's own work. Work done in collaboration with, or with the assistance of, others, is indicated as such. Any views expressed in the dissertation are those of the author.

SIGNED: DATE:.....

Contents

1	Introduction	1
1.1	The cuprate phase diagram	1
1.1.1	Mott insulating parent compound	1
1.1.2	Superconducting dome	2
1.1.3	Coherent phase	3
1.1.4	The pseudogap	3
1.1.5	Previous work by the Bristol group	5
1.1.6	Properties of BSCO ₂₂₀₁	7
1.2	The high- T_c pairing mechanism	10
1.2.1	The case against conventional superconductivity in high- T_c	11
1.2.2	Spin-fluctuations	12
1.2.3	Pairing in the pnictides	13
1.2.4	The BaFe ₂ (P _x As _{1-x}) ₂ series	14
2	Theory	19
2.1	Fermi liquid theory	19
2.2	De Haas-van Alphen oscillation	20
2.2.1	Overview	20
2.2.2	Exploring the origin of the oscillations	21
2.2.3	Lifschitz-Kosevitch equation	24
2.2.4	Zeeman-Doppler shifting of oscillations	29
2.2.5	Band mass	29
2.2.6	Final theoretical observations	30
2.3	Spin density wave instability	31
2.3.1	Lindhard susceptibility	31
2.3.2	Notes on practical calculation	33
2.4	Density functional theory	34
2.4.1	The generalised gradient approximation	36
2.4.2	Single particle wavefunction bases	37
2.5	Hall effect	37
2.5.1	Effects of Fermi surface topology	37

3 Experimental Technique	39
3.1 De Haas-van Alphen torque measurement	39
3.1.1 Experimental apparatus	39
3.1.2 Data analysis	42
3.1.3 Measuring the spin mass	46
3.1.4 Extracting effective mass from the temperature dependence	48
3.2 Density Functional Theory	50
3.3 Calculating susceptibility	50
3.4 Measuring charge transport	53
3.4.1 Experimental apparatus	54
3.4.2 Sample size determination	59
3.4.3 Data Analysis	59
3.4.4 Determining the doping	63
4 dHvA measurements on BaFe₂P₂	65
4.1 Sample synthesis	65
4.2 X-Ray Diffraction	66
4.3 Angle dependent measurements	67
4.3.1 Determining experimental parameters	67
4.4 Obtaining the Fermi surface for members of the BaFe ₂ (P _x -As _{1-x}) ₂ series	79
4.5 Harmonic parametrisation of the Fermi surface	81
4.6 Susceptibility calculations	82
4.7 Determining the spin effective mass	88
4.8 Determining the thermal effective mass	91
4.9 Conclusions	94
5 Hall measurements on BSCO₂₂₀₁	99
5.1 Sample growth	99
5.2 Size determination	100
5.3 Doping determination	101
5.4 Temperature sweeps	106
5.5 Hall plots	107
5.6 Conclusions	114
Bibliography	117

<i>CONTENTS</i>	ix
A ‘Microfit’ parameters	123
B Lindhard susceptibility calculation code	125
C Focused Ion Beam (FIB) scans	131

Chapter 1

Introduction

This chapter begins by detailing a suitable interpretation of the high- T_c phase diagram which is consistent with the results presented in later chapters. In particular it outlines some important, apparently conflicting results and some possible means to understand them. Following this is an overview of the pairing mechanisms in high- T_c materials and in particular the pairing due to spin-fluctuations.

1.1 The cuprate phase diagram

The phase diagrams for the high- T_c materials show a remarkable consistency across the cuprates*. However this universality amongst the cuprates comes with an abundance of features which provide for some complex physical interactions and fragile intermediate ‘crossover’ phases. The tuning parameter for the cuprate phase diagram is either electron or hole doping typically performed by elemental substitution at the crystal growth stage or by oxygen incorporation through annealing. As shown in figure 1.1.1, the two types of doping are not symmetric with hole doping generally resulting in more robust superconductivity. For this reason the literature has largely concentrated on the hole doped progression and as a result it is far better characterised. The doping is usually expressed as a p value which represents the amount of additional holes (electrons) per Cu atom.

1.1.1 Mott insulating parent compound

Starting at the middle of figure 1.1.1, the parent compound materials at zero doping are thought to be Mott insulators i.e. the top most filled state on each lattice site contains one electron. In the conventional band picture this

*This is in contrast with the recently discovered pnictide materials which show significant variations in scalings and even composition

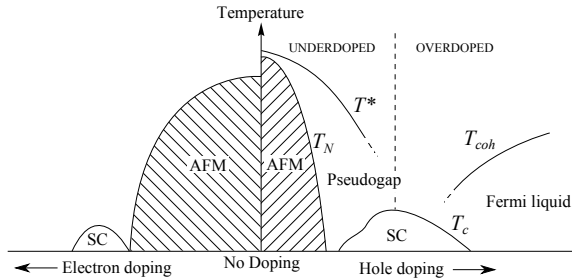


Figure 1.1.1: A schematic phase diagram showing electron doped to the left and hole doped to the right. AFM is the antiferromagnetic Mott insulating phase, SC is the superconducting phase. T^* , T_N , T_c and T_{coh} are the temperature scales for the pseudogap, AFM state, superconductivity and coherent Fermi liquid phases respectively

should be metallic since the bands are only partially filled, however when we consider a local picture of electrons, any movement of an electron to the neighbouring lattice site will cause an energetically costly double occupancy on one site and zero occupancy on another. This causes the electronic density of states (DOS) to become gapped around the Fermi surface and hence suppressed conduction. This is known as the Mott insulating state.

We find that the kinetic energy term is reduced when the ordering of the sites is antiferromagnetic since for any hopping to occur at all, the spins must be antialigned to avoid double occupancy of like spins. This region dominates the low doping portion of the phase diagram and remains antiferromagnetic until either the temperature is high enough to allow transitions from the Fermi energy to the states at the edge of the gap or the doping has introduced enough double occupancy electrons on lattice sites, which can move without the double occupancy energy cost, to overcome the insulating behaviour.

1.1.2 Superconducting dome

With increased doping, the antiferromagnetic state gives way to the superconducting dome at around $p = 0.05$ which itself gives way to a Fermi liquid metallic state at a doping of around $p = 0.3$. The maximum T_c occurs at around $p = 0.16$. Transitions from both the antiferromagnetic and the superconducting state are clearly second order thermodynamic with jumps in the heat capacity for example, however there are other regions in the phase

diagram which are less well defined such as the pseudogap and the Fermi liquid crossover whose temperature scale can depend on the particular probe used and do not feature a clear order parameter.

1.1.3 Coherent phase

To the heavily overdoped side of the phase diagram, beyond the superconducting dome lies the coherent region where the system bears the hallmarks of a conventional metal. The implication is that correlations between electrons are sufficiently weak such that the mass enhanced quasiparticles of Landau's Fermi liquid theory are well defined, leading to conventional metal behaviour. A clear indication of this is a dominant T^2 term in the resistivity. Above this region we observe an anomalous additional contribution which has been modelled both with T^2 plus an additional linear term or by a T^n term where $1 \leq n \leq 2$. This additional term has been observed in heavy Femrion materials and is often associated with proximity to a quantum critical point (QCP) [1].

1.1.4 The pseudogap

Above the antiferromagnetic region and the superconducting state is one of the most controversial regions of the phase diagram, the so called pseudogap phase. This is a region which was first demonstrated in 1989, just a few years after the discovery of the cuprate materials, by nuclear magnetic resonance (NMR) measurements performed at Bell labs [2]. A noticeable fall in the susceptibility occurred at a temperature significantly above T_c which led to conclusion of possible spin pairing before the onset of bulk superconductivity*. The question arose as to what the exact relation of the pseudogap is to the superconducting state — is it a precursor state, from which superconductivity arises or is it a competing phase? — and from a materials development point of view, to obtain higher T_c should we be finding ways to suppress the crossover to the pseudogap state or encourage it? By finding where exactly the T^* energy scale meets the superconducting dome, strong evidence can be found that supports one or the other scenario. However the problem lies in the type of probe used. Select spectroscopic measurements

*Cooper paired electrons in the singlet state have zero net spin hence they do not contribute to the susceptibility, whereas unpaired electrons do. Cooper pairing leads to a reduction in susceptibility, see for example neutron scattering plots.

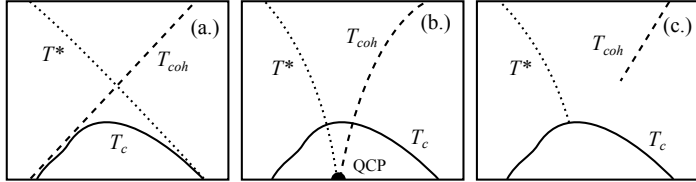


Figure 1.1.2: Three scenarios proposed for the T^* temperature scale behaviour. (a.) the pseudogap as the ‘precursor’ state, (b.) as the ‘competing’ state, (c.) and the ‘transition’ scenario.

including Scanning Tunneling Microscopy (STM), Angle Resolved Photoemission Spectroscopy (ARPES) and Raman spectroscopy on materials of comparable T_c values have found that the T^* overreaches the superconducting dome entirely [3], meeting with the overdoped edge at $T = 0$ K. This supports the precursor state theory illustrated in figure 1.1.2 (a.) where T^* and T_{coh} cross to define a region which is below both temperature scales where the carrier are both coherent quasiparticles and paired leading to the superconducting condensate.

A second scenario is supported by measurements using bulk probes such as heat capacity, magnetic susceptibility and resistivity measurement have shown the T^* energy scale drops into the top of the superconducting dome [4]. This supports the scenario where the pseudogap is in competition with superconductivity for states at the Fermi surface. Once the pseudogap phase is suppressed, scattering from quantum fluctuations at zero temperature leads to the formation of the superconducting phase at a QCP similar to that found in heavy fermion materials. This scenario is supported by the observation of linear scaling of the resistivity with temperature in the region above the superconducting dome which is a hallmark of proximity of a QCP.

A third scenario is one where the pseudogap simply becomes the superconducting gap as it meets the top of the superconducting dome. However this scenario leaves hanging questions as to the roles of the pseudogap, T_{coh} and other phenomena in the phase diagram which would need to be addressed theoretically. Moreover this picture is rendered less compelling by the observation in $\text{La}_{2-x}\text{Sr}_x\text{CuO}_4$ (LSCO) of rapidly increasing, low temperature, normal state resistivity inside of the underdoped superconducting dome which implies the non-superconducting energy gap persists into this

region.

1.1.5 Previous work by the Bristol group

Clearly lots of interesting physics is occurring in and around the superconducting dome and a solid understanding of this region is key to understanding the problem of high- T_c . Prof. N. Hussey has been involved in many efforts to shed light on the situation, of which, two key ones are highlighted here.

Links between anisotropic scattering and T_c

Simply measuring resistance along different axes gives an averaged scattering rate through all conduction paths and so to build a map of the angle dependent scattering rates, a different technique must be used. In Angle Dependent Magnetoresistance (ADMR) a strong persistent magnetic field is applied before resistance measurements are taken. The field serves two purposes; firstly, to suppress superconductivity so the normal state can be probed, secondly to confine the electrons to orbits perpendicular to the field. By detailed analysis of the change in resistance as the field is applied at various angles, a picture of the angle dependent scattering rate can be determined.

After performing measurements on samples of $\text{Tl}_2\text{Ba}_2\text{CuO}_6$ (Tl_{2201}) with dopings ranging from strongly overdoped to slightly underdoped [5], a trend emerged which is illustrated in figure 1.1.3. Here the scattering rate within

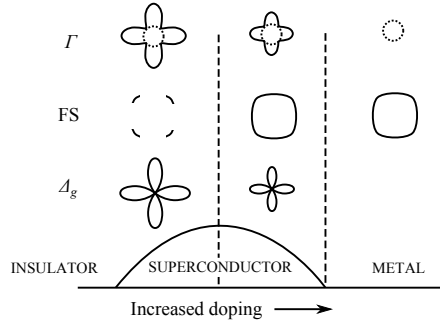


Figure 1.1.3: Schematic of how the scattering rate, Γ , the Fermi surface, FS , and the superconducting gap, Δ_g evolve with doping across the superconducting dome. Based on figure 1 in ref [6]. The dotted line in the scattering is the isotropic part.

the ab -plane, Γ , was found to be composed of two terms; an isotropic term which remained constant with doping (dotted circle) and an anisotropic component which scaled with the superconducting gap, Δ_g . Moreover it was found that the superconducting gap and the anisotropic scattering rate both shared the same shape, being ‘d-wave’. This further ties to ARPES measurement which show that on the underdoped side of the superconducting dome there is a pronounced change in the Fermi surface where at the antinodal points of Γ (and Δ_G) the spectral weight disappears [7] i.e. coherent particles are lost away from the regions of strong scattering.

T-Linear behaviour in the superconducting dome

Previous high-field transport measurements on Sr doped LSCO [8] gave key insights into the nature of the T-linear term as it entered the superconducting term on the overdoped side. In particular it showed that the T-linear term did not funnel down to a point (figure 1.1.4) as is typical of QCP behaviour but instead spread out into the superconducting region. Intrigued as to this unexpected behaviour, we looked to repeat the measurements on $\text{Bi}_{2+z-y}\text{Pb}_y\text{Sr}_{2-x-z}\text{La}_x\text{CuO}_{6+\delta}$ (BSCO₂₂₀₁) which can be doped far more widely without divergence in the resistivity so that we could then see how the T-linear term progressed on the underdoped side, where T^* is undisputed. Performing measurements which would shed light onto which of the

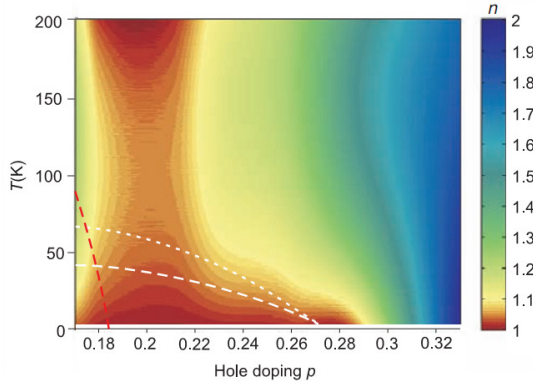


Figure 1.1.4: Plot of the T^n term in the fitted field suppressed normal state of Sr doped LSCO showing the T -linear term extending throughout the superconducting dome and not to a single QCP. Taken from Cooper *et al.* [8]

scenarios shown in fig 1.1.2 is most likely to be correct formed the original

motivation for the investigation of BSCO_{2201} through transport measurements.

A second reason for the study of BSCO_{2201} in particular is that it's van-Hove singularity occurs at a different doping — further from optimal doping — than LSCO. Should similar behaviour be found then we can confidently claim that the unusual QCP behaviour is not due to proximity to the changeover in hole-like to electron-like Fermi surface and is likely universal to all cuprates.

BSCO_{2201} also demonstrates transport behaviours which are consistent with other high- T_c cuprate materials. For example, from magnetoresistance (MR) measurements it demonstrates a similar maximum in the underdoped $d\rho_{ab}/dT$ curve as underdoped YBCO [9]. On the overdoped side, BSCO_{2201} demonstrates a monotonic upward trend in $d\rho_{ab}/dT$ with increasing temperature similar to what has been observed in Tl_{2201} and LSCO [9].

During the course of the investigations however, it became apparent that even with field strengths of up to 60 T in pulsed fields, the upper critical field, H_{c2} of many of the sample at key temperatures could not be reached. However, field strengths were generally strong enough to recover *B*-Linear behaviour in the Hall component.

Previous Hall measurements have been performed on BSCO_{2201} by Ando *et al.* [9, 10] which are shown for comparison in the results section. However these results do not go to low temperatures, being restricted by the onset of superconductivity. Our own results used high field measurements at Laboratoire National des Champs Magnétiques Intenses (LNCMI) and High Field Magnet Laboratory (HFML) to suppress superconductivity and examine the low temperature regions in detail. Moreover our samples are focused on the overdoped region which complements the underdoped data set presented in the Ando papers.

1.1.6 Properties of BSCO_{2201}

The unit cell of the high- T_c , doped cuprate $\text{Bi}_{2+z-y}\text{Pb}_y\text{Sr}_{2-x-z}\text{La}_x\text{CuO}_{6+\delta}$ (BSCO_{2201}) is illustrated in figure 1.1.5. It is made up of layers as follows from the top; a BiO layer, then a SrO layer, then a CuO lattice common to all cuprates, then two BiO layers, a SrO layer, a CuO, SrO and a BiO layer. Variants of BSCO_{2201} include $\text{Bi}_2\text{Sr}_2\text{Ca}_1\text{Cu}_2\text{O}$ (BSCO_{2212}) and $\text{Bi}_2\text{Sr}_2\text{Ca}_1\text{Cu}_3\text{O}$ (BSCO_{2213}) which feature one and two extra CuO layers

respectively. Most closely related in terms of structure is Tl_{2201} which features Tl and Ba in place of Bi and Sr respectively. $BSCO_{2201}$ is orthorhombic with $a = 5.362(3)$ Å, $b = 5.374(1)$ Å and $c = 24.622(6)$ Å [11], Tl_{2201} on the other hand has $a = 5.4580(3)$ Å, $b = 4848(5)$ Å and $c = 23.2014(5)$ Å [12]. Undoped $BSCO_{2201}$ has an excess of holes and lies slightly to the undoped

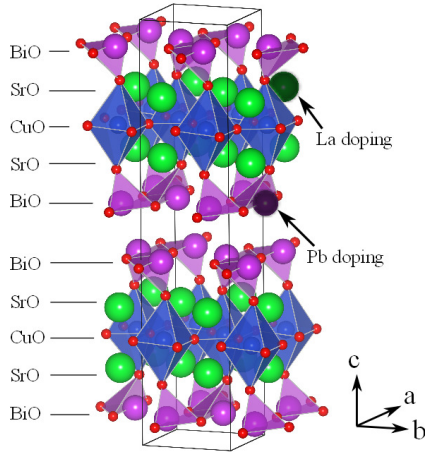


Figure 1.1.5: Unit cell of $BSCO_{2201}$ demonstrating the layers. Tl_{2201} is similar but with La for Bi and Ba for Sr. Note that Pb doping occurs away from the CuO planes.

side of the phase diagram. By substituting in La for Sr, the amount of holes is reduced allowing access to a range of slightly overdoped to underdoped. However, since the substitution takes place adjacent to the CuO planes where all the interesting electronic behaviour happens, La doping introduces a lot of disorder into the system. Pb is also substituted for Bi which increases the number of holes allowing the more overdoped region to be accessed. Since Pb substitutes into the BiO layer which is far from the CuO plane, less disorder is introduced. Sometimes Pb is introduced alongside La even when a more underdoped state is desired to avoid forming structures in the BiO planes which affect ARPES measurements [13]. Furthermore, annealing in oxygen decreases the number of carriers depending on how much additional oxygen is absorbed allowing for even more fine grained tuning of the doping. By adjusting these parameters a very wide range of doping values can be accessed in $BSCO_{2201}$ which makes it appealing for study.

The precise determination of doping from a chemical standpoint is tricky. For LSCO — assuming pure ionic donation — substituting more Sr for La

simply adds one more hole per extra Sr atom per unit cell. However for $\text{YBa}_2\text{Cu}_3\text{O}_y$ (YBCO₁₂₃) and $\text{YBa}_2\text{Cu}_4\text{O}_y$ (YBCO₁₂₄) for example, there exist CuO chains (oxygen deficient CuO layers) which absorb some of the doped charge, in other cuprates the heavy metal atom has a mixed valency meaning that the substitution relation is not so straightforward. Various techniques described in the methods section have been described to determine the doping level but as a rule some a priori knowledge of composition is required.

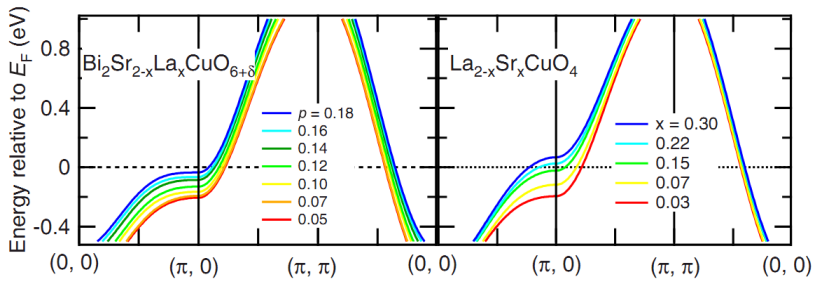


Figure 1.1.6: Band dispersions at the Fermi energy for various dopings. Left panel shows BSCO₂₂₀₁, right panel shows LSCO. Note the saddle points at $(\pi, 0)$ which cause the van-Hove singularity at $p \approx 0.18$ for LSCO and at $p \geq 0.2$ for BSCO₂₂₀₁. Adapted from ref [14].

There is a crossover in overdoped cuprates between a large hole-like Fermi surface to an electron-like Fermi surface that leads to a saddle point in the DOS and consequently a van Hove singularity* as shown in figure 1.1.6, adapted from ref. [14]). This occurs in LSCO at around $p = 0.18$ which is approximately critical doping and may lead one to believe that the critical behaviour is related to the proximity of the van Hove singularity. However the same crossover does not happen at the same doping in BSCO₂₂₀₁, rather it appears to occur at $p \geq 0.2$, relatively far from the critical value of $p \approx 0.16$. For this reason BSCO₂₂₀₁ is an attractive material to study to determine more about the relationship (or lack thereof) between the critical behaviour and the van Hove singularity.

Finally BSCO₂₂₀₁ has a relatively low maximum T_c , being around 36 K at best. Because T_c is so low, this makes BSCO₂₂₀₁ ideal for normal state study since less field will be required to suppress T_c at lower temperatures

*A spike in the ‘acDOS’ brought about by a flat region of the bandstructure at the Fermi level

and there should be a narrower fluctuation region.

1.2 The high- T_c pairing mechanism

The previous section details some of the nuances of the cuprate phase diagram but does not make any statements as to what interaction actually causes the Cooper pairs to couple — the so called ‘pairing glue’. The second half of this thesis detail measurements which investigate the possibility of spin density waves (SDWs) fluctuations as the bosonic scatterer that bind the electrons together.

The charge carrier in a superconducting condensate is a Cooper pair — a quasi-particle comprising of a bound state of two electrons or two holes with opposite spin and momentum. Evidence for this configuration arises as a natural result of the Ginzberg-Landau model which, when applied to a superconducting system, gives the charge of the quasi-particle carriers as $2e$, where e is the charge of an electron. Given that due to their like charges two free electrons repel, it is natural to ask what could overcome the electromagnetic force to cause these electrons to remain bound in this quasi-particle state.

Bardeen, Cooper and Schreiffer established much of the theoretical basis — from which the Ginzberg–Landau model can be derived — in Bardeen-Schreifer-Cooper (BCS) *theory* (named after the authors). Within the framework of BCS theory, Bardeen Cooper and Schreiffer wrote a 1957 paper [15] detailed a pairing mechanism known as the BCS *model* which would explain how these electron remained bound together. The model is based around the concept of phonons scattering off ions which well suited the superconducting materials known at the time. Phenomenologically, the mechanism of attraction is straightforward. Electrons moving through a crystal lattice attract ions on the lattice sites. These heavy ions respond slowly and are drawn in *behind* the electron. This has the effect of both screening the negative electron charge as well as providing an attractive positive potential for any electron following the original electron. The net effect is the leading electron draws the following electron in its wake, thus coupling them with one another. The wavelike distortion of the ions in the lattice can be considered as a phonon, and the interaction between the electrons and the lattice can be modelled as electron–phonon–electron scattering.

The BCS model on top of BCS theory accurately describes what we now know as *conventional superconductivity*, that is pairing which forms a spin-singlet state ($S = 0$) and which has zero orbital angular momentum ($L = 0$). It was not until the discovery of superfluidity* in ^3He in 1972 [17] that it became apparent that there may exist forms of pairing that resulted in spin-triplet pairing state ($S = 1$) with $L > 0$. This was later confirmed when superconducting analogues were found in the form of heavy Fermion materials. What really spurred the explosion in interest though was the 1986 discovery by Bednorz and Müller [18] of high transition temperature (T_c) superconductivity in the cuprates and, more recently, the ‘pnictides’ by Kamihara et al. [19]. The cuprate class of materials that Bednorz and Müller found to be superconducting have transition temperatures far in excess of any previously known superconducting materials and although the BCS model phonon pairing may play a part, the predominant pairing mechanism in the high- T_c materials is likely to be something else entirely.

1.2.1 The case against conventional superconductivity in high- T_c

There is a great deal of evidence in the literature for non-BCS model pairing in the high- T_c and heavy Fermion materials. Although the pairing wavefunction cannot be measured directly with current techniques, experiments indirectly infer *unconventional* i.e. non s-wave, BCS-model, characteristics. For example, analysis on penetration depth measurements of YBCO₁₂₃ show power law behaviour [20], indicating that there exists states within the momentum averaged gap. SQUID measurements and Josephson tunnelling experiments on the same material have confirmed alternating phase of the condensate wavefunction which points strongly to $d_{x^2-y^2}$ -wave symmetry [21] (see also refs. therein). As for other cuprate materials, specific heat measurements on BSCO₂₂₀₁ [22], as well as penetration depth measurements on LSCO [23] have also proved consistent with d -wave pairing.

More evidence against conventional superconductivity include the unusual normal state (i.e. non-superconducting) state properties of the cuprates and heavy Fermion materials. The BCS model is grounded in Landau Fermi

*Superfluidity and superconductivity share much of the same physics although rather than electrons or holes pairing, molecules pair instead. Parallels between the two are discussed in ref. [16]

liquid theory which models interacting itinerant electrons with quasiparticles of heavier effective mass than ordinary electrons and holes. A hallmark of Fermi liquid behaviour is a T^2 dependence of the resistance, however experiments on the cuprate LSCO [8] and a heavy Fermion material [1] have demonstrated fractional power law behaviour, T^γ where $1 < \gamma < 2$, at temperatures above the superconducting transition. Given that the Fermi liquid model breaks down in these examples, it follows that the BCS-model also is likely on shaky ground for these materials.

There are several arguments against phonons as the sole pairing mechanism in the pnictide case, Boeri et al. [24] and Mazin et al. [25] present calculations showing that the magnitude of the phonon pairing strength is not adequate for the high T_c values attained in LaAsOF, Haule et al. [26] note in the same material that the gradient of the density of states (DOS) at the Fermi level is such that you would expect an increase in DOS and hence T_c with hole doping if the BCS model held, however the reverse is true. Non Fermi-liquid behaviour was demonstrated in the $\text{BaFe}_2(\text{P}_x\text{As}_{1-x})_2$ series [27, 28] and although many superconducting pnictides are believed to have a nodeless superconducting gap [29–32] there are many [29, 33–36] including the $\text{BaFe}_2(\text{P}_x\text{As}_{1-x})_2$ series [37–39] which are thought to have nodes.

It is interesting to note that unlike the cuprates which universally show a $d_{x^2y^2}$ gap symmetry, the pnictide materials are not all alike, even pnictides along the same series such as the LiFeAs and LiFeP show a change in gap structure. Consequently, it may prove that the nature of the superconductivity may not be universal amongst the pnictide materials. Irrespective of this, the BCS model pairing alone has been shown to be too weak to explain high- T_c superconductivity.

1.2.2 Spin-fluctuations

One possible alternate pairing mechanism arises from scattering due to spin fluctuations. A common feature of phase diagrams for all of the pnictides and the cuprate materials is close proximity of a SDW magnetic state to the superconducting state. As described in more detail in section 2.3, the SDW state is a general form of magnetic order that describes a periodic modulation of the spins of a system and encompasses antiferromagnetism and arguably ferromagnetism. As a system enters a SDW state, short range, damped, an-

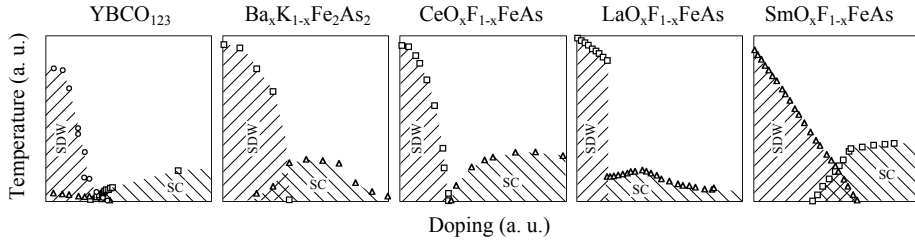


Figure 1.2.1: Phase diagrams for various high- T_c materials adapted from ref. [40] showing the proximity of the superconducting phase (SC) to the spin density wave state (SDW) in all cases

tiferromagnetic fluctuations occur and it is these that are thought to provide the pairing interaction for the Cooper pair states.

Spin fluctuations were originally investigated as a mechanism which *suppressed* conventional, i.e. *s*-wave, superconductivity [41] from ferromagnetic fluctuations and were used to explain why nearly ferromagnetic metals such as Pd has lower than expected T_c . Later however it was found that for symmetries such as *d*-wave that *antiferromagnetic* spin fluctuations could possibly provide an interaction which is attractive and could overcome the Coulomb repulsion [42].

Typically spin-fluctuations occur due to favourable band structure conditions, in particular where there is a *nesting* condition. This is where a hole-like Fermi surface band maps through reciprocal space onto a similarly sized electron-like Fermi surface via a particular vector \mathbf{q} known as the nesting vector. Since strong nesting leads to a stable SDW state, we are looking for only partial nesting in the Fermi surface of superconducting materials so that we get enough spin fluctuations to cause pairing but not too many to cause a full SDW state.

As an aside, nesting is not the only cause of spin fluctuations. For example, frustrated spin systems such as the Kagome triangular lattice can also be a cause of spin fluctuations, however this is thought to occur only in very specific 1D and 2D materials.

1.2.3 Pairing in the pnictides

Soon after the discovery of the pnictide materials, a possible pairing mechanism was proposed based on the above described spin density wave fluctuations. The original paper suggested a s_{\pm} gap symmetry [25] which

features a multi band model based on $\text{LaFeAsO}_{1-x}\text{F}_x$. The spin fluctuation coupling vector couples over the Brillouin zone (BZ) diagonal two separate, approximately cylindrical, Fermi surfaces of opposite phase. Although this is an extended *s*-wave model, the geometry is satisfied by the relative positions of the Fermi surfaces within the BZ.

As already stated, more recent measurements have discovered nodes in the gap structure in many pnictide materials and while no nodes featured in the original Mazin model, there is no reason why the model can be adapted to include them.

1.2.4 The $\text{BaFe}_2(\text{P}_x\text{As}_{1-x})_2$ series

In order to explore the role of nesting in the high- T_c superconductors, an investigation at Bristol was undertaken on the Fermiology of the $\text{BaFe}_2(\text{P}_x\text{As}_{1-x})_2$ series by studying angle resolved de Haas–van Alphen (dHvA) oscillations and in particular the end-member, BaFe_2P_2 .

The $\text{BaFe}_2(\text{P}_x\text{As}_{1-x})_2$ series is one of many that stem from the parent compound BaFe_2As_2 , although unlike the electron doped $\text{BaCo}_{2x}\text{Fe}_{2(1-x)}\text{As}_2$ and the hole doped $\text{Ba}_x\text{K}_{(1-x)}\text{Fe}_2\text{As}_2$ series, the $\text{BaFe}_2(\text{P}_x\text{As}_{1-x})_2$ progression is entirely isovalent meaning that the changes affected due to the P substitution are due to structure and chemical pressure rather than additional charge carriers. Nonetheless, superconductivity occurs with a very similar phase diagram as with the charge-doped examples in the same ‘122’ family of iron-pnictide materials.*.

At $x = 0$ the $\text{BaFe}_2(\text{P}_x\text{As}_{1-x})_2$ series begins at BaFe_2As_2 , a compound which becomes antiferromagnetic at around 138 K, and moves with increasing x towards BaFe_2P_2 which is metallic to low temperatures. Neither end members are superconducting, however as As is substituted for P, the low temperature antiferromagnetic state decays, giving way to superconductivity which kicks in at approximately $x = 0.18$ and increases to the optimal substitution of $x = 0.31$. Superconductivity then decreases until it gives way to a paramagnetic ground state at around $x = 0.71$. Figure 1.2.2 shows the phase diagram adapted from ref. [44] as determined by resistivity measurements. Also detailed in the phase diagram is the structural transition which occurs as the tetragonal $I4/mmm$ cell moves to an orthorhombic cell

*See for example figure 1 in ref. [43]

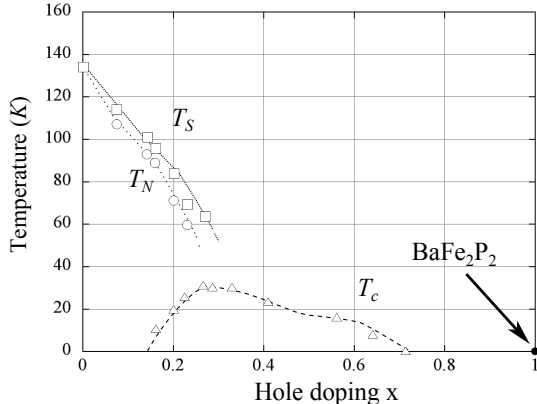


Figure 1.2.2: Phase diagram adapted from ref [44] measured by resistivity. T_s , T_N and T_c are the structural transition, the antiferromagnetic transition and the superconducting transition temperatures respectively.

as it passes below the line marked T_s . This is a feature which is common to many of the ‘122’ pnictide materials.

The progression along the series is isovalent since P and As are in the same periodic group – group V. The net effect of the substitution is to apply an increasing chemical pressure as x moves towards 1. Several reports show that applying high *physical* pressure (~ 5 GPa) to BaFe₂As₂ results in a similar phase diagram with an antiferromagnetic phase and superconductivity up to ~ 30 K [45–47] with Klintberg *et al.* [48] presenting a direct comparison between the two types of pressure. As pressure is applied, the unit cell a axis shrinks slightly less than the c axis ($\sim 3\%$ cf. $\sim 4.5\%$ respectively). Interestingly the c axis shrinking largely occurs in the Fe-Pnictide plane leading to some theories of the superconductivity emerging from the tetrahedral bond angle between the Fe and the pnictogen.

The BaFe₂(P_xAs_{1-x})₂ series from a substitution of $x = 0.41$ –1.0 has been previously measured by members of the group at Bristol using dHvA oscillations[49]. As suggested in the Shishido reference, since dHvA has been observed across such a large range of substitutions, it implies that the material is not prone to disorder as is the case in many charge doped series [50] making the series an excellent candidate for dHvA studies. This could be explained by the fact that the substitution is isovalent and that there is relatively little contribution at the Fermi surface from the pnictide sites*

*See for example, the orbital character for the iron sites from density functional theory

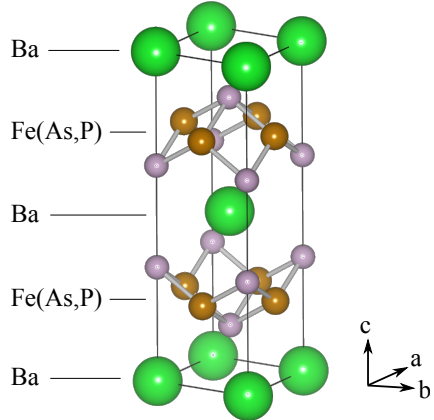


Figure 1.2.3: The tetragonal unit cell of the 122 $\text{BaFe}_2(\text{P}_x\text{As}_{1-x})_2$ series clearly showing the tetragonally bonded $\text{Fe}(\text{As},\text{P})$ layers.

where the substitution takes place, meaning the Fermi surface should not be strongly disrupted when traversing the series. The Fermi surfaces from the Shishido paper have been characterised for x ranging from 0.41 to 1 for electron sheets only but have clearly shown that the DFT calculations consistently overestimate the size of the surfaces. They also show a linear progression of the electron orbit sizes which is proportional to x . Moreover, dHvA measurements on the material with $x = 0.63$ have been performed where one of the hole surface extrema was observed[51] however DFT calculations as well as comparisons with SrFe_2P_2 [52] give evidence for a second hole Fermi surface for materials towards the P end of the series, (towards the As end of the series, there appears this second hole and a *third* hole surface similar but smaller to the other hole sheets). If the electron Fermi surfaces are oversized in the DFT calculations, then the hole Fermi surface volumes should also be oversized in order to remain compensated (electrically neutral). What is not clear though is whether the *shapes* of the hole pockets are also altered in the compounds leading to BaFe_2P_2 . DFT calculations show the larger of the hole pockets in particular undergoing significant geometric changes, specifically in that it becomes much more three dimensional as P substitution becomes more complete. The Fermi surface of the opposite end-member, BaFe_2As_2 , has been fully characterised by previous ARPES measurements[53] and dHvA[54, 55]. Coupled with a full characterisation of

(DFT) calculations presented later in this chapter

the Fermiology of BaFe₂P₂, this data can be used to interpolate Fermiology of the hole pockets between end members thus completing the partial determination of the Fermi surfaces of the intermediary compounds.

The ARPES measurements of the Fermi surface of BaFe₂As₂ below the Néel temperature concluded that despite some k_z dispersion in the Fermi surfaces, there is adequate nesting to form the antiferromagnetic state. Ab-initio DFT calculations[49] of the paramagnetic state have shown the k_z dispersion increasing with increasing P, with the outer hole pockets becoming more three-dimensional through the progression providing the partial nesting conditions necessary for pair forming SDW fluctuations described in section???. One caveat is that these calculations do not take into account the structural changes below T_s , another caveat is that they do not consider Fermi surface reconstruction due to the observed commensurate antiferromagnetic order. To fully settle the issue of the nature of the nesting in the superconducting state, experimental determination of the Fermi surfaces of the series is necessary, a good guide to which can be obtained from study of the end-members.

This thesis presents data which details the full Fermi surface of BaFe₂P₂ including an elucidation of the shape of the 3D outer hole surface. Partial nesting is detailed between the outer hole surface and the inner electron surface with $q = (\pi, \pi, \pi/2)$ meaning the phenomenon persists through to the end member of the series. Also presented are effective mass measurements which show relatively small mass enhancements implying weak carrier correlations.

Chapter 2

Theory

This chapter outlines the theoretical basis for both the concepts and measurements relevant to this thesis. We start with very brief overview of Fermi liquid theory, leading on to the theory behind the dHvA torque technique, then a brief overview of DFT and magnetotransport.

2.1 Fermi liquid theory

The nearly-free electron gas model for ordinary metals* is an extremely coarse approximation to the real situation and yet provides surprisingly good, predictive results in a variety of scenarios. Fermi liquid theory provides the theoretical basis which explains why we can use non-interacting particle models with a simple modification of the masses of the interacting Fermionic particles.

From a mathematical standpoint, Fermi liquid theory considers a gas of non-interacting particles and gradually ‘switches on’ the interactions. Provided the system transitions adiabatically[†] then the ‘particles’ in the resulting system, which is known as a *Fermi liquid*, can be modelled using the same mathematics as the non-interacting system with an adjusted mass. This adjusted mass is known as the *enhanced mass* and encompasses the interactions in the system with the magnitude being an indicator of the interaction strength. The enhanced mass particles are labelled quasiparticles since they no longer share the same mass as an electron at rest and are, arguably, a product of a mathematical abstraction.

At the time of writing, Fermi liquid theory describes what would be considered ‘ordinary’ metals with deviations from Fermi liquid theory generally

* A model which only considers the kinetic energies of the electrons and Pauli exclusion terms

[†]i.e. with no symmetry breaking changes in phase or, in other words, there is a one-to-one mapping of the particles in the initial non-interacting system to the quasiparticles in the final interacting system

considered of interest in a number of systems. Moreover the theory behind measurement techniques such as dHvA — described in the next section — rely on the existence of coherent quasiparticles at the Fermi surface to be valid. The reconciliation of observed dHvA oscillations in cuprates with evidence for reduced quasiparticle weight from ARPES data currently provides one of the interesting challenges of high- T_c research.

2.2 De Haas-van Alphen oscillation

In this section the phenomenon of dHvA oscillations is described. It is not immediately apparent how a ramping magnetic field could cause oscillations in such a wide range of parameters but Lifshitz and Kosevich provided an explanation through their eponymous equation based on a theoretical basis set out by Landau. This was then used to characterise the Fermi surface of many metals and establish the field of ‘Fermiology’. Strictly, only the oscillations in magnetisation are dHvA oscillations and those in resistance are called Shubnikov-de Haas oscillations. Nonetheless they both originate from the same underlying phenomena of oscillations in the free energy of the system.

2.2.1 Overview

For metals, the majority of the interesting physics occurs at the Fermi level and, provided Fermi liquid theory holds true, the electrons at the Fermi level can be modelled to a high degree of accuracy with the Sommerfeld model — that is a Fermi gas of non-interacting electrons in an infinite box. When a magnetic field is applied, the electrons have their usual grid pattern distribution of plane wave k-vectors rearranged such that the electrons move around orbital and helical paths. These rearranged k-vectors form a set of concentric tubes, known as Landau tubes, whose cross-sectional area, a , perpendicular to the field is given by the Onsager relation:^{*}

$$a_{k\perp} = (r + 1/2) \frac{2\pi eB}{\hbar} \quad (2.2.1)$$

^{*}Derivations of the Onsager relation are given in several textbooks including pg. 32 of Schoenberg [56] and pg. 272 of Ashcroft & Mermin [57].

where r is a quantisation number that sets apart each tube. We can see from the relation that as \mathbf{B} increases, so does the cross-sectional area of the tubes. As the magnetic field is ramped, successive tubes periodically pass the Fermi surface causing a spike in the DOS at the Fermi level and also oscillations in the energy of the system, E , which, for geometric reasons explained in the next section, are far stronger at the maximal and minimal (extremal) areas of Fermi surface. Thermodynamic quantities such as magnetic susceptibility ($\chi = \partial E / \partial B$) and heat capacity ($C_V = \partial^2 E / \partial T^2|_V$) or quantities that depend on the DOS at the Fermi level such as electrical resistance all oscillate as the field is ramped. Oscillations in the susceptibility are known as dHvA oscillations, oscillations in the resistivity are known as Shubnikov-de Haas oscillations.

We can relate the ‘frequency’ F (measured in *tesla*^{*}) that the tubes pass the Fermi surface to the extremal Fermi surface area using the following application of the Onsager relation,

$$a_{k\perp} = \frac{2\pi e}{\hbar} F \quad (2.2.2)$$

By varying the direction of the field we can obtain a series of maximal and minimal Fermi surface areas in a variety of orientations in order to build a profile of the Fermi surface topology and size. In practice, there are many possible variations that might fit the model based on areas of cross-sectional slices alone and so typically ab-initio DFT calculations — described in sections 2.4 and 3.2 — are employed to provide a basis which can be tweaked based on the constraints from the measurements.

A more detailed analysis of this process follows, beginning with an illustrative mathematical treatment for oscillations in the magnetisation.

2.2.2 Exploring the origin of the oscillations

We begin by calculating the degeneracy of the Landau tubes i.e. the number of electron states per tube. Because the states under a magnetic field are a one-to-one rearrangement of the states with no field, we can use the Sommerfeld number of states per unit k-space ($V/4\pi^3$) to determine the degeneracy. From the Onsager relation (eqn. 2.2.1) we see that the addi-

^{*}n.b. that it is *tesla* and not *tesla*⁻¹ because, as we shall see later, the oscillations are actually periodic in $1/B$ and *not* B so their frequency counterpart is measured in *tesla*.

tional area for successive tubes is $\Delta a_{k\perp} = 2\pi eB/\hbar$ which we can convert to a volume by integrating over k_\perp . This gives a degeneracy per tube therefore of,

$$D_{\text{tube}} = dk_\perp \left(\frac{2\pi eB}{\hbar} \right) \left(\frac{V}{4\pi^3} \right) = \frac{eBVdk_\perp}{\hbar 2\pi^2} \quad (2.2.3)$$

We continue by writing an expression for the energy of the system, E by summing the energies of the states that lie beneath the cross-sectional area defined by the Fermi surface ($a_{k\perp F}$) for a given k_\perp . To do this, we use the Onsager equation to determine R_\perp — the number of Landau tubes below the Fermi surface at this cross-sectional slice. We then multiply this by the degeneracy of the tubes, D and the energy for states on that particular Landau tube, ϵ_r ,

$$E = D \sum_r^{R_\perp} \epsilon_r = \frac{eBVdk_\perp}{\hbar 2\pi^2} \sum_r^{R_\perp} \epsilon_r \quad (2.2.4)$$

where,

$$R_\perp = \text{floor} \left[\frac{a_{k\perp F}\hbar}{2\pi eB} - \frac{1}{2} \right] \quad (2.2.5)$$

To complete the above equation, we need an expression for the energies of each of the Landau tubes. The procedure for the free electron case is to insert the canonical momentum (i.e momentum of a free electron in a magnetic field) into the non-interacting Schrödinger equation and solve to obtain the following eigenvalues for the energies on the Landau tubes. Full derivations can be found in several textbooks* and so will not be repeated here. Below is the expression for the energy eigenvalues,

$$\epsilon_r = (r + 1/2)\hbar\omega_c + \frac{\hbar^2 k^2}{2m_0} \quad \text{where, } \omega_c = \frac{eB}{m_0} \quad (2.2.6)$$

and is known as the *cyclotron frequency*. The summation term in equa-

*See for examples pg. 32ff. in Schoenberg [56] or pg. 148ff. in Blundell [58].

tion 2.2.4 can now be written,

$$\begin{aligned}
 \sum_r \epsilon_r &= \sum_r^{R_\perp} \left((r + 1/2)\hbar\omega_c + \frac{\hbar^2 k^2}{2m_0} \right) \\
 &= \frac{\hbar e B}{m_0} \sum_r^{R_\perp} r + \frac{\hbar e B}{2m_0} \sum_r^{R_\perp} 1 + \frac{\hbar^2 k^2}{2m_0} \sum_r^{R_\perp} 1 \\
 &= \frac{\hbar e B}{2m_0} R_\perp (R_\perp + 1) + \frac{\hbar e B}{2m_0} R_\perp + \frac{\hbar^2 k^2}{2m_0} R_\perp \\
 &= \frac{\hbar e B}{2m_0} R_\perp^2 + \left(\frac{\hbar e B}{m_0} + \frac{\hbar^2 k^2}{2m_0} \right) R_\perp
 \end{aligned}$$

which can be expanded out and finally substituted back into equation 2.2.4 to finally obtain,

$$E = \frac{e^2 V dk_\perp}{4\pi^2 m_0} B^2 \left[R_\perp^2 + 2R_\perp + \frac{\hbar k^2}{e} \frac{1}{B} R_\perp \right] \quad (2.2.7)$$

Key to the above relation is that, although R_\perp is inversely proportional to B , it remains discrete. This gives rise to the saw-tooth like function shown in figure 2.2.1 for some typical experimental parameters. Also plotted is the function against $1/B$ where we can clearly see that the oscillations are periodic in inverse field hence the frequency being measured in tesla $^{-1}$.

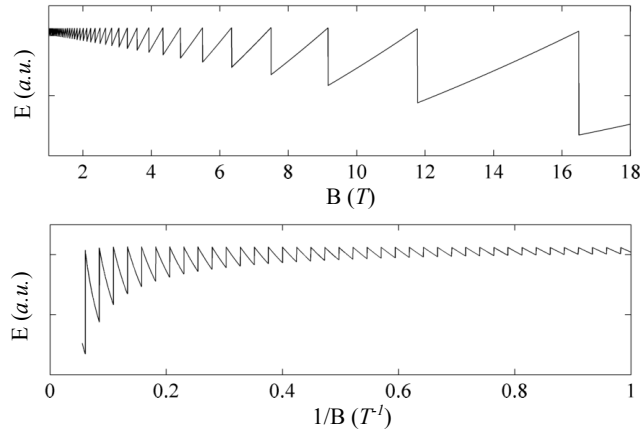


Figure 2.2.1: Theoretical energy oscillations for a Fermi surface orbit which is 5% of a 5 Å cubic BZ between 1-18 T. Kinetic energy term is taken to be for an electron at a level half the size of the Fermi surface.

The above is not a rigorous derivation but is nonetheless illustrative

of the origin of the oscillation in the system energy and how any thermodynamic value which depends on the energy of the system oscillates as a function of field. To continue we need to include correction factors to the oscillation amplitude due to finite electron scattering rates (A_D), temperature (A_T), Zeeman splitting of spins (A_s), doping (A_{dop}), mosaicity (A_{mos}), warping of the Fermi surface (A_{warp}) as well as adjustments due to the fact that the parameter measured was torque of the sample in a field and not the energy or magnetisation directly (A_Γ). For this, we turn to a more solid foundation that was put forward by Lifschitz and Kosevitch and presented by Schoenberg.

2.2.3 Lifschitz–Kosevitch equation

The derivation for the full expression for the Landau thermodynamic potential, Ω^* , begins in a similar way to the previous illustrative example but frames the sawtooth-like function above as a more mathematically manageable Fourier decomposition which also conveniently makes the technique highly amenable to Fourier analysis. For this reason the equation below features higher harmonics which are denoted with the identifier p .

$$\Omega = \left(\frac{e}{2\pi\hbar} \right)^{\frac{3}{2}} \frac{e\hbar B^{\frac{5}{2}}}{m_0\pi^2} \left| \frac{\partial^2 a_{\text{ext}}}{\partial k_\perp^2} \right|^{-\frac{1}{2}} \sum_{p=1}^{\infty} p^{-\frac{5}{2}} A_{\text{tot}} \cos \left[2\pi p \left(\frac{F}{B} - \gamma \right) \pm \frac{\pi}{4} \right] \quad (2.2.8)$$

where,

$$A_{\text{tot}} = A_T A_D A_s A_\Gamma A_{\text{mos}} A_{\text{dop}} A_{\Delta B} \quad (2.2.9)$$

The above equation and derivatives of it are known as the Lifschitz–Kosevitch (LK) equation. To obtain the magnetisation the differential with respect to b is taken to get,

$$M = \left(\frac{e}{\hbar} \right)^{\frac{3}{2}} \frac{e\hbar F V B^{\frac{1}{2}}}{m_0\pi^{\frac{5}{2}}\sqrt{2}} \left| \frac{\partial^2 a_{\text{ext}}}{\partial k_\perp^2} \right|^{-\frac{1}{2}} \sum_{p=1}^{\infty} p^{-\frac{3}{2}} A_{\text{tot}} \sin \left[2\pi p \left(\frac{F}{B} - \gamma \right) \pm \frac{\pi}{4} \right] \quad (2.2.10)$$

To attain the above equations, it was necessary to perform an integral over k_\perp [†] which results in a parameter for an extremal Fermi surface orbit area

^{*}Formally defined as the energy in an open system that is in thermal contact with its surroundings

[†]Similar to the integral in the toy equation from the previous section

perpendicular to the field given by a_{ext} .

Attenuation for non-extremal orbits

Only the extremal (i.e. the largest and smallest) magnetically induced orbits contribute significantly to oscillations in the system energy. This is because F represents a phase factor in the LK equation and at the extremal points $dF/dk_{\perp} = 0$ meaning more orbits near extrema are in phase. However it is not immediately clear how much stronger the oscillations from the extremal orbits will be in comparison to other orbits. Figure 2.2.2 shows examples of the strengths of the oscillations after integrating over a distribution of phases shown in the insets. The panels each show the phases from the distributions

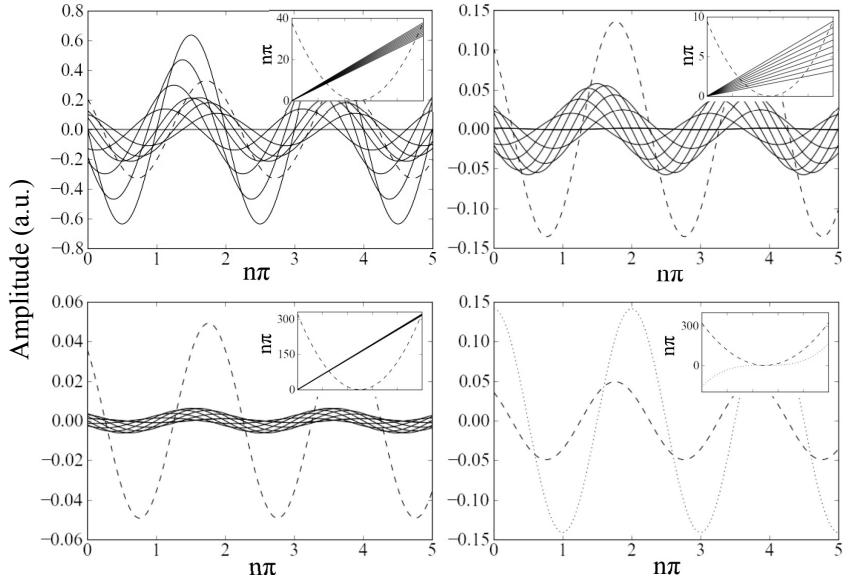


Figure 2.2.2: The sum of 1000 cosines with phase dispersions shown in the insets. Dashed line represents an extremal dispersion, solid lines a spread of linear dispersions and dotted line represent a non-extremal inflection point. Top left, top right and bottom left panels have phase distributions that are scaled from 0 to ~ 1 , ≈ 10 and ≈ 100 Landau tube ‘wavelengths’ respectively.

taken over a range of scales, and it is clear that the phase cancellation is more acute for longer scales. This makes sense if we consider that the Landau tubes passing the Fermi surface are a oscillatory measurement probe like any other and so will be wavelength limited. That is, if the difference between the outermost and innermost orbits are of the order of the Landau tube spacing

as it passes the Fermi surface, then the oscillations will be difficult to pick out. Interestingly this also places a limit on the maximum field that can be used to probe a Fermi surface since, according to the Onsager relation, the larger the field the larger the spacing between tubes. In practice this is simply $\Delta a_{k\perp}$ which means that in terms of F , the resolution is simply the field (i.e. $\sigma_F \sim 18$ T for the Yellow magnet at Bristol).

A final point is that it is not strictly extremal points that contribute significantly to the oscillations, but also inflected stationary points as shown in the last panel of figure 2.2.2 so one could imagine a pathological stepped Fermi surface that would feature several strong orbital oscillations which would not be at turning points.

Variations in the phases can also be put into practice to model the various effects on the LK equation listed towards the end of the previous section. These can be manifest by convolving an appropriate phase distribution function with the cosine oscillatory term. It can be shown* that this convolution results in a relatively simple multiplication factor — hence the various A factors listed in the LK equation which we expand upon below.

Attenuation due to temperature

To find the appropriate phase distribution function for the temperature dependence we start with the Fermi distribution,

$$f(\epsilon) = \frac{1}{\exp((\epsilon - \mu)/kT) + 1} \quad (2.2.11)$$

The differential of this distribution results in the broadening function (which is proportional to the probability that the Fermi energy μ is between ϵ and $\epsilon + d\epsilon$),

$$P(\epsilon < \mu < \epsilon + d\epsilon) \propto \frac{d\epsilon}{2kT(1 + \cosh[(\epsilon - \mu)/kT])} \quad (2.2.12)$$

This is convolved across the Fermi energy to smear it and also the phase through the parameter F . The details of how this is done is given in Schoen-

*See for example, Schoenberg pg 57–59. [56]

berg pg. 59ff [56] with the end result is given by,

$$A_T = \frac{X}{\sinh(X)} \quad \text{where, } X = \frac{2\pi^2 p k T m_T^*}{e \hbar B} \quad (2.2.13)$$

The above factor includes m_T^* , the *thermal effective mass* as a term in a function of T . As a consequence, by studying the temperature dependence of the amplitude it is possible to get a measure of m_T^* of the electrons at the extremal orbit. Techniques for doing this are discussed in section 3.1.4.

The effective mass determined in this way is enhanced subject to the same interactions as in heat capacity experiments — i.e. electron-phonon interactions and spin symmetric correlations — but are probed for a particular Fermi surface orbit, whereas heat capacity is bulk averaged. As we will see later the mass enhancement is different to that from spin measurements. For more one this see Rourke *et al.* [59] and references therein.

Attenuation due to finite quasiparticle lifetime

The *Dingle factor*, A_D , is due to the finite lifetime, τ , of the electron quasi-particles due to scattering. Because of this time scale, there is a smearing of the electron energy through the uncertainty principle with a broadening which is approximately Lorentzian in shape. If we assume τ does not change with energy*, then this can be modelled as a smearing of the Fermi level such that the broadening function is,

$$P(\epsilon < \mu < \epsilon + d\epsilon) \propto \frac{d\epsilon}{(\epsilon - \mu)^2 + (\hbar/2\tau)^2} \quad (2.2.14)$$

and such that after the routine Fourier transform, the end relation is given by,

$$A_D = e^{-\pi p m_b / e B \tau} = e^{-\pi p / \omega_c \tau} \quad (2.2.15)$$

The exponent in the above can be thought of as the number of orbits the electron has completed (i.e. each harmonic p is another successive orbit) divided by the expected number of orbits it will complete, so evidently we expect to see the higher harmonics having an exponentially lower amplitude. The term m_b refers to the *band mass* which will be discussed in detail later

*This is not the case, but at most only a few Landau levels contribute to a particular oscillation and if we assume that the energy does not vary too much between subsequent levels then the assumption is a good one

on.

Attenuation due to spin splitting

Applying a magnetic field causes a Zeeman splitting of energy levels of magnitude,

$$\Delta\epsilon = \frac{ge\hbar B}{2m_e} \quad (2.2.16)$$

where m_e is the free electron mass and g is a factor that is ≈ 2 for free electrons. Rather than smearing, this can be thought of as two separate Fermi surfaces with separate Fermi energies. The attenuation is given then as,

$$A_s = \cos\left(\frac{\pi p g m_s^*}{2m_e}\right) \quad (2.2.17)$$

where m_s^* is the *spin effective mass*. This is subject to a different set of interaction in comparison to the thermal effective mass – notably both spin symmetric and antisymmetric correlations but not the electron-phonon interactions. As such, in materials with strong phonon interactions we may see a strong difference in m_s^* and m_T^* .

Other attenuating factors

Another attenuating factor due to slight misalignments in the crystal structure, (A_{mos}), causing a mosaic polycrystalline structure could be modelled with an appropriate broadening function. Schoenberg suggests a Lorentzian similar to the Dingle factor — there is no solid mathematical basis for this but no other function shape has been observed in experiment. The final form would then look like the following,

$$A_{mos} = e^{2\pi p \Delta F_{mos}/B} \quad (2.2.18)$$

where ΔF_{mos} is a parameter that determines the degree of overall misalignment.

The final attenuating factors mentioned here are $A_{\Delta B}$, the damping due to field inhomogeneity which has an effect depending on the shape of the field and A_{dop} , which is another Lorentzian-like broadening factor due to the doping inhomogeneity in the sample. Neither of which will be considered in the thesis — the material studied is undoped, and the magnet is suitably

large as to have an essentially linear field profile —doping and so will not be explored further*

2.2.4 Zeeman-Doppler shifting of oscillations

One ramification of the spin splitting is that as the field ramps there is a gradual increase and/or decrease in the size of the split Landau levels commensurate with field with $\Delta a \propto B$. In a paramagnetic material we expect there to be a majority of spins aligned with the field meaning the Fermi surface will mostly shrink as the field ramps in one direction and expand as it ramps in the opposite direction. This leads to an apparent extra shift in the frequency which is proportional to B which is of order of the field strength.

2.2.5 Band mass

So far, three different electron masses have been defined, the thermal effective mass, the spin effective mass and the free electron mass. To tie these together a fourth mass is introduced, the *band mass*. This is another effective mass resulting from the electrons being subject to the bandstructure potential as defined by DFT calculations and is given by,

$$m_b^* = \hbar^2 \left(\frac{d^2\epsilon}{dk^2} \right)^{-1} = \frac{\hbar^2}{2\pi} \frac{\partial a_{k\perp}}{\partial \epsilon} \quad (2.2.19)$$

Mass enhancement comes from any kind of interactions the electron has with its environment — i.e. external fields, other electrons and nuclei — resulting in the free electron mass m_e becoming enhanced (renormalised). The bands mass can be determined from DFT and the resulting enhancement is purely from the interaction of the electron with the calculated lattice potential. However DFT calculations typically do not model correlation effects well or dynamic interactions at all. We know that both the thermal effective mass and the spin effective mass incorporate the band mass enhancements plus a unique set of interactions specified previously. Figure 2.2.3 lays out how the effective masses build on each other by incorporating more interactions. because of this particular hierarchy, it is sometimes possible to compare

*If you do want to consider these factors, ref [59] has a passage on doping homogeneity and pg. 64 of Schoenberg discusses field inhomogeneity ??.

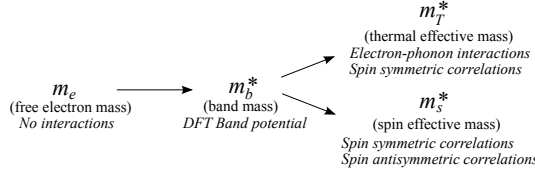


Figure 2.2.3: A diagram showing how the successive electron masses build on the previous interactions. Additional interaction effects are listed in italics.

effective masses to get a sense of scale of the interactions.

A 2D Approximation

Although none of the attenuating factors above have an explicit angle dependence, they do vary as a function of angle through the band mass. A common approximation to simulate the dependency in layered systems is to assume the Fermi surface is two dimensional in shape and therefore cylindrical. The cross section of a cylinder is given by,

$$a = \frac{a_0}{\cos \theta}, \quad (2.2.20)$$

where θ is the angle from the cylinder axis. Increasing the Fermi energy by $\Delta\epsilon$ will cause the cross section at zero angle to change by amount Δa_0 , then the band mass is given by,

$$m_b^* = \frac{\hbar^2}{2\pi} \frac{\partial a_{k\perp}}{\partial \epsilon} = \frac{\hbar^2}{2\pi} \frac{\partial}{\partial \epsilon} \left(\frac{a_0 + \Delta a_0}{\cos \theta} - \frac{a_0}{\cos \theta} \right) = \frac{\hbar^2}{2\pi} \frac{\partial a_0}{\partial \epsilon} \frac{1}{\cos \theta}, \quad (2.2.21)$$

therefore

$$m_b^* = \frac{m_{b0}^*}{\cos \theta} \quad (2.2.22)$$

This means that under this approximation, any factor that includes the band mass, explicitly or implicitly* can be resolved using the zero angle band mass with an angle dependence of $1/\cos \theta$.

2.2.6 Final theoretical observations

Originally dHvA measurements were used to measure the Fermi surfaces of elemental metals and so the initial assumption of a free-electron gas is

Meaning m_T^ and m_s^* which are both enhancements of the band mass

justified based on the fact that elemental metals have a Fermi surface and are considered materials that adhere to Fermi liquid theory. The fact that oscillations have been observed in cuprates and pnictides which have demonstrated non-Fermi liquid behaviour is therefore remarkable and moreover implies the presence of a Fermi surface, at least in the presence of a strong magnetic field.

2.3 Spin density wave instability

Section 1.2 discussed the possibility of high- T_c pairing being due to fluctuations in close proximity to a SDW state. Here we briefly describe the SDW state and some of the theory behind it.

Broadly speaking a SDW is a magnetic state just as ferromagnetism and antiferromagnetism are magnetic states. In its most general sense, a SDW is a periodic modulation of magnetic spins in both space and time hence it being a ‘wave of spin density’. AFM is actually a special case of a SDW which does not vary in time, i.e. is static, and also varies spatially with the periodicity being some multiple of the real-space lattice vector, i.e. is commensurate with the lattice. Ferromagnetism can be thought of as a SDW state with wavevector $\mathbf{q} = 0$ i.e. it has no periodic variation and so is not really a ‘wave’.

Using the mean field Hartree-Fock approximation (HFA) the following expression gives the stability condition for the SDW state [60],

$$2I\chi_0(\mathbf{q}) > 1, \quad (2.3.1)$$

where I is the exchange energy between electron bands and χ_0 is the Lindhard susceptibility. The greater the Lindhard susceptibility, the more stable the state.

2.3.1 Lindhard susceptibility

The Lindhard susceptibility models the Stoner excitations (i.e. electron-hole scattering) of a nearly free electron system. To derive the Lindhard susceptibility, we begin with a Fermi liquid i.e. a Pauli excluded but otherwise non-interacting gas of free electrons. We calculate* the first order

*Not presented here but pg 81 ff. of Dressel [61] has a full derivation.

perturbative linear response of this gas to a magnetic field given by $\mathbf{B} = \exp(\mathbf{q} \cdot \mathbf{r} - \omega \cdot \mathbf{t})$. The resulting equation is often quoted as,

$$\chi_0(q, \omega) = \lim_{\delta \rightarrow 0} \sum_k \sum_{l, l'} \frac{f(\epsilon_{k+q, l'}) - f(\epsilon_{k, l})}{\epsilon_{k+q, l'} - \epsilon_{k, l} - \hbar\omega - i\delta} D \quad (2.3.2)$$

where,

$$D = |\langle k + q, l' | V | k, l \rangle|^2 \quad (2.3.3)$$

and is the matrix transition element for the scattering process. The numerator term contains two Fermi functions — the same as eqn. 2.2.11 — which ensure that the susceptibility is finite for states which scatter across the Fermi energy and zero if they do not — consequently, the Lindhard susceptibility models electron-hole scattering (Stoner excitations) in particular. The Fermi functions also smear the susceptibility dispersion as a function of temperature. The third term in the denominator corresponds to the excitation energy of the perturbing field with ω corresponding to the temporal frequency of the field. The final term in the denominator is an artefact of the adiabatic approximation used to calculate the perturbation with the completed approximation taking the limit of $\delta \rightarrow 0$. The first sum in the Lindhard function is over all k states in the first BZ, the second sum combines each energy band. The real and imaginary parts of equation 2.3.2 are,

$$\text{Re}\{\chi_0(q, \omega)\} = \lim_{\delta \rightarrow 0} \sum_k \sum_{l, l'} \frac{(\epsilon_{k+q, l'} - \epsilon_{k, l} - \hbar\omega)(f(\epsilon_{k+q, l'}) - f(\epsilon_{k, l}))}{(\epsilon_{k+q, l'} - \epsilon_{k, l} - \hbar\omega)^2 + \delta^2} D \quad (2.3.4)$$

$$\text{Im}\{\chi_0(q, \omega)\} = \lim_{\delta \rightarrow 0} \sum_k \sum_{l, l'} \frac{-\delta(f(\epsilon_{k+q, l'}) - f(\epsilon_{k, l}))}{(\epsilon_{k+q, l'} - \epsilon_{k, l} - \hbar\omega)^2 + \delta^2} D \quad (2.3.5)$$

$$(2.3.6)$$

respectively. The real part is important in the context of instabilities in metals, the imaginary part gives the resonance modes for bosonic excitations of energy $\hbar\omega^*$.

The Lindhard function is a simple linear response for a particular static charge configuration. As soon as the charge configuration shifts due to the

*e.g. plasmons, spin density waves, charge density waves, phonons etc.

perturbing field the potential changes and so does the response. To compensate we consider the perturbing field to be adjusted by considering an additional induced field due to the changing charge along with the perturbing field and calculate the linear response in terms of that new combined field. This new form is the *first renormalisation*. This is still not perfect however since now the charge density changes again in a different way due to this new combined potential and so a second induced potential has to be considered giving the *second renormalisation* and so-on. This process of renormalisation forms the basis of linear response theory. In practice the random phase approximation (RPA)* is generally invoked where corrections beyond the first renormalisation are ignored. The RPA response of the Lindhard susceptibility is as follows,

$$\chi(\mathbf{q}, \omega) = \frac{\chi_0(\mathbf{q}, \omega)}{1 - \frac{4\pi e^2}{q^2} \chi_0(\mathbf{q}, \omega)} \quad (2.3.7)$$

Peaks in this function correspond to scattering of states which cross the Fermi energy yet remain close to the Fermi energy. We can derive this function by modelling an oscillatory perturbing field on a system. To solve to get an expression for the second order perturbation, we make the adiabatic limit approximation (i.e. the perturbing potential is gradually increase from zero at $t = \infty$ to v at $t = 0$).

Although knowledge of the susceptibility is useful to model, for example, neutron scattering measurements, for our purposes we will use it as an indicator of possible SDW instability vectors in our example materials. For this reason we make the assumption that the transition matrix elements are unity. This assumption greatly simplifies the calculations at the cost of some structure and as such should be borne in mind that the results are somewhat broad and qualitative.

2.3.2 Notes on practical calculation

Taking the limits of $\delta \rightarrow 0$ of eqn. 2.3.6 which is effectively an ever narrowing Lorentzian distribution, results in an expression for the imaginary part of Lindhard susceptibility, $\text{Im}(\chi_0) \propto \delta(\epsilon_{k+q,l'} - \epsilon_k, l - \hbar\omega)$ where δ here is the

*So called because it is considered that the charge densities in the higher renormalisations are from electron wavefunctions which have randomly shifted phases and so cancel each other out.

Dirac delta function. In a calculation on a continuous energy dispersion, this results in resonances at excitations which match the difference in energies between states. However, in this thesis, the energy dispersions used to determine nesting conditions are not continuous and instead are based on discrete energies obtained from DFT calculations. As such δ will have to remain finite in order to broaden the delta function into a Lorentzian with width comparable to the energy differences between the discrete points – the net result of this will be loss of some fine structure.

Secondly, only bands that lie close to the Fermi energy contribute significantly to the susceptibility. Since the calculations are computationally costly, only bands which are close (within the adiabatic or temperature broadening) to the Fermi energy are input into the calculations.

2.4 Density functional theory

The interpretation of the dHvA measurements presented later in this thesis rely to some extent on the ab-initio calculation of the energy bands of BaFe₂P₂ — the technique used to find these energy dispersions are based on a DFT scheme. The following is broad overview of DFT which is drawn from notes from a series of summer school lectures by M. Lüders [62] and the ‘ABC of DFT’ by K. Burke [63].

Although implementations of DFT rely on various approximations, the theory of DFT itself has been shown to be exact and mathematically rigorous. It comprises of a set of theorems developed and proven by Hohenberg, Kohn and Levy [64, 65] and a methodology for solving to obtain the ground state energies developed by Kohn and Sham. The principle theorem outlined by Hohenberg-Kohn (HK) shows that the ground state external potential, $v_{\text{ext}}(\mathbf{r})$, of a system can be determined by the ground state density, $n(\mathbf{r})$, alone and vice-versa. A second HK theorem outlines a minimisation condition which expresses the ground state energy as follows,

$$\frac{\partial F[n]}{\partial n(\mathbf{r})} + v_{\text{ext}}(\mathbf{r}) = \mu, \quad (2.4.1)$$

where,

$$F[n] = T[n] + V_{\text{ee}}[n] \quad (2.4.2)$$

$F[n]$ is the ‘universal’ functional* and $T[n]$ and $V_{ee}[n]$ are the kinetic and correlation functionals respectively. μ is the chemical potential which is introduced as a normalisation term that ensures that there are an appropriate number of electrons in the charge density. The universal functional is so called because the system is completely defined in the external potential term alone and so $F[n]$ is common to all systems, nonetheless it still requires approximation. For this reason as well as the fact that there are no clues from the HK theorems as to a good starting form for n , still means the problem is intractable.

Kohn-Sham developed a method to find a good starting form for n by showing that there exists a pseudo-potential, v_{KS} , that satisfies the above equation for a *non-interacting* system, i.e. $F[n] = T[n]$, which shares the same n as the original interacting system. This abstract potential, which takes the place of v_{ext} in the above equation, has no strict physical meaning but it allows us to build a common expression for n in terms of a sum of single particle wavefunctions. It is given as follows,

$$v_{KS} = v_{ext}(\mathbf{r}) + \int d^3r' \frac{n(\mathbf{r}')}{|\mathbf{r} - \mathbf{r}'|} + \frac{\partial E_{xc}}{\partial n(\mathbf{r})} \quad (2.4.3)$$

where E_{xc} is the combined particle correlation and exchange energy terms which is approximated according to the type of problem to be solved†. Once an approximate form for the exchange term has been chosen, the above can be used to find the ground state energy by running a self consistency cycle that forms the heart of most DFT codes,

1. Guess an initial $n_{i=0}$
2. Calculate v_{KS} from n_i using eqn. 2.4.3
3. Minimise the non-interacting (Kohn-Sham) form of eqn. 2.4.1
4. Calculate the new n_{i+1}

*A functional maps a function onto a single vector or scalar — typically by integrating over the function — and is commonly denoted with the function parameter in square brackets. Compare this with the definition of a function which maps a series of scalars onto a single scalar or vector.

†Note that in principle, these two terms should be separate but most approximations tend to combine them into a single term.

5. Repeat from step 2 with n_i being adjusted by n_{i+1} until $n_i - n_{i+1} <$ some tolerance

Simply replacing n_i with n_{i+1} can cause the calculation to rapidly diverge and so instead a mixing scheme is used. Typically this incorporates a small fraction of n_{i+1} with the rest made up of the old n_i . A more complex mixing scheme can be employed to ensure more rapid convergence, the Broyden mixing scheme for example uses a Newton-Raphson style root finding mechanism on the Jacobian of the $n_i - n_{i+1}$ [66].

2.4.1 The generalised gradient approximation

The correlation term represents the most significant approximation in the calculation of DFT. For the DFT presented in this thesis, the Generalised Gradient Approximation (GGA) was used which is part of the family of Local Density Approximations (LDAs). The simplest (i.e. lowest order) LDA takes the effects of the electron-electron correlations at point \mathbf{r} to be constant throughout the system with the magnitude based on the charge density at \mathbf{r} . This works particularly well for free-electron-like systems with lots of itinerant valence electrons since the electrons are evenly spread throughout — however it does not work so well for highly localised Hubbard-like systems where there is a high density of electrons at atomic sites, but very little density just off the sites. A step towards improving this comes by raising the order of the approximation so that it modifies the constant local density with the rate of change of the local density as you move off the site (i.e. the local charge density gradient). It turns out however that incorporating the gradient results in less accuracy than the simple LDA due to the LDA ‘accidentally’ cancelling a series of so called sum rules. The GGA builds on the higher order gradient approximation by incorporating the cancelling of the sum rules to obtain a reasonably accurate approximation to the correlation potential.

The precise way to express the GGA however is still a matter of debate though with there being multiple implementations [67, 68], each of which may give slightly different results*. Nonetheless GGAs tends to perform better than zeroth order LDA with inhomogeneous electron densities.

*See for example table 1 in ref. [67]

2.4.2 Single particle wavefunction bases

Typically, close to the atom, electrons tends to have a radial symmetry whereas itinerant valence electrons are more planewave-like. Matching each of these to an appropriate single particle basis set dramatically reduces the amount of calculation time. The augmented plane wave (APW) method defines a series of ‘muffin-tin spheres’ which are centred on each of our atoms. Those well inside are described in terms of radial basis orbitals, those well outside are described in terms of plane waves.

Andersen further simplified the radial basis portion of the APW method by approximating the wavefunctions by a first order Taylor expansion with respect to energy [69]. The result is known as linearised augmented plane wave (LAPW).

2.5 Hall effect

The Hall effect is a simple consequence of the Lorentz force on a moving charge. As an electron (hole) moves along a rectangular slab subject to a perpendicular magnetic field, the electrons (holes) are deflected to one side of the slab. Eventually the charge density one one side becomes high enough that the Coulomb repulsion force of the density on subsequent charge carriers balances the Lorentz force and an equilibrium voltage between either side of the slab is reached. This voltage is known as the Hall voltage, V_H and is given by,

$$V_H = -\frac{IB_{\perp}}{ned} \quad (2.5.1)$$

where I and B_{\perp} are the current and perpendicular magnetic field and n , e and d are the carrier density, charge and slab thickness respectively. V_H is what is measured in our experiment. This is usually further abstracted to the Hall coefficient, R_H , which encapsulates the carrier density as follows,

$$R_H = \frac{V_H d}{IB_{\perp}} = \frac{1}{ne} \quad (2.5.2)$$

2.5.1 Effects of Fermi surface topology

Ostensibly, a hole-like Fermi surface would be expected to demonstrate positive Hall coefficient and an electron-like Fermi surface a negative, however

it is possible to obtain the exact opposite due to the curvature of the Fermi surface [70].

For a 2D metal in the weak field semiclassical limit, Ong determined that the transverse conductivity, σ_{xy} from which R_H is derived can be obtained by integrating the mean free path vector, $\mathbf{l}_k = \mathbf{v}_k \tau_k$ over the Fermi surface (\mathbf{v}_k is the Fermi velocity and τ_k is the momentum dependent scattering rate). This is illustrated in figure 2.5.1 which integrates over a Fermi surface with a long mean free path in the (π, π) direction and shows how the resulting \mathbf{l}_k traces two loops in opposite directions giving rise to a larger ‘negative’ loop from the negative curvature even though the overall surface has a positive curvature. This illustrated scenario is close to what we find in the cuprates

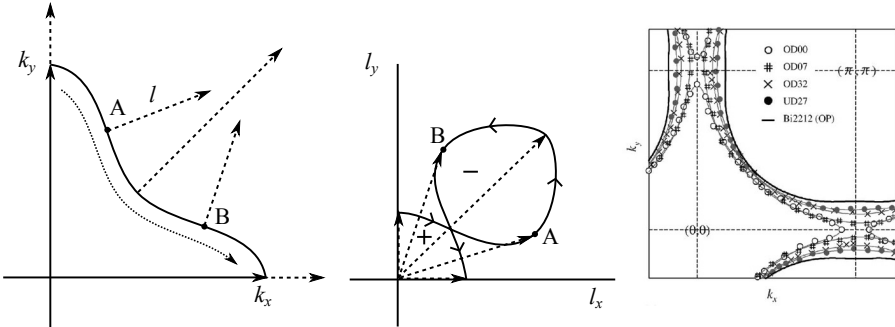


Figure 2.5.1: Left illustrates a negatively curved Fermi surface with a long mean free path along the $k = (\pi, \pi)$ portion and the integral progressing along the dotted line. Middle shows how the mean free path vector changes along the integral line tracing two loops of opposite direction. Adapted from ref. [70]. Right shows the progression of the BSCO_{2201} Fermi surface about the van-Hove singularity. Adapted from ref. [71].

at high doping. Here the mean free path is affected by the anisotropic scattering rate detailed in the introduction section and the proximity of the van-Hove singularity leads to negative curvature in the long flat sides of the Fermi surface as it changes between hole-like and electron-like, as shown for BSCO_{2201} in the right side panel of figure 2.5.1, adapted from ref [71].

Chapter 3

Experimental Technique

This chapter begins with descriptions of how the dHvA measurements were performed, the equipment used and the analysis. Next, a description of the methods and code used to calculate susceptibility is supplied and finally descriptions of the magnetotransport measurements and analysis are detailed.

3.1 De Haas-van Alphen torque measurement

In this section the measurement of dHvA oscillations by the torque method is described. For decades, the measurement of dHvA oscillations provided the principle method of characterising the Fermiology of a material with only relatively recent competition from techniques such as positron annihilation and ARPES in particular. Whilst ARPES can provide direct maps of Fermi surfaces within the BZ, dHvA has some advantages such as the fact that it ignores surface effects such as crystal reconstruction, can determine cross-sectional areas with a relatively high resolution and also provides useful secondary measurements such as effective masses of the quasiparticle carriers. Some disadvantages of the technique include the fact that dHvA cannot locate particular cross-sectional orbits within the BZ (thus relies on secondary knowledge such as DFT calculations) and also that the high magnetic fields could potentially affect the Fermi surface, for example by splitting the energy levels. Regardless dHvA continues to be a reliable technique for Fermi surface characterisation.

3.1.1 Experimental apparatus

Much of the experiment apparatus has already been described in great detail by Dr. C. Andrew in her thesis [72] and so only a broad overview and points of difference will be described here.

Torque cantilever

A highly sensitive measure of torque is required to pick up the moments experienced by the sample due to the field. For this reason a commercial piezoelectric AFM cantilever, provided by Seiko corps., was repurposed to measure this. The sample was placed onto the topside of the lever above the AFM tip. Previously this would be superglued in place but for these measurements we tried successfully with using vacuum grease which freezes the sample in place at low temperatures. This has the added benefit of still being adjustable and removable when warmed back to room temperature. Moreover, when it comes to rotate the sample in the basal plane, this was possible by nudging the sample gently without having to move the cantilever and risk breaking the lever with the sample permanently affixed. Care should be taken not to get grease on the pivot point of the levers since this will freeze the lever in place at low temperatures. The cantilevers fea-

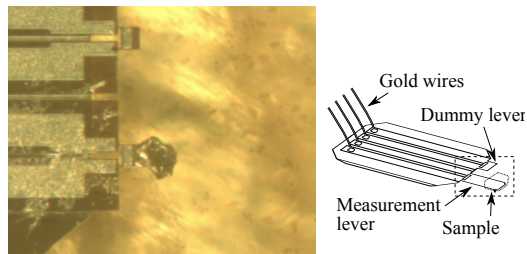


Figure 3.1.1: Photo of the BaFe_2P_2 sample mounted on the measurement lever along with a schematic showing the full cantilever assembly. N.b. the BaFe_2P_2 crystals often cleave along the [110] plane and so despite the apparent 45° rotation, the sample is aligned such that the lever flexes in the [100] plane.

ture a second dummy lever alongside the principle lever where the sample was mounted. Instead of measuring the voltage across the principle lever alone, we measure the difference of the voltages between the two levers using a Wheatstone bridge. This enables some degree of correction due to vibrations and fluctuations in measurement current. The circuit is balanced using a variable resistor and is zeroed as best as possible within the noise before each measurement run.

The voltage is supplied and measured using Stanford SR830 lock-in amplifier. The output is first amplified using an EG&G 5113 pre-amplifier with a gain of $\times 1000$ with a band pass filter which was suitably set for the lock-in

amplifier excitation frequency.

Sample stage

The cantilever is mounted onto the sample stage which is a one axis Swedish rotator fabricated entirely from hysol. This is moved by an external stepper motor controlled by a computer.

The angle of the stage in relation to the field is determined by one of two orthogonal pick-up coils mounted on the sample stage. A weak, oscillating magnetic field is generated by a coil which is wound around the sample space such that it is concentric with the main high field coil. The AC coil induces a voltage in these orthogonal pick-up coils on the stage which is proportional to the sine of the angle they are at with respect to the field. The pick-up coil voltage is measured by a second Stanford SR830 lock-in amplifier after passing through a custom amplifier set to $\times 100$. The lock-in amplifier also drives the oscillating field after passing a custom built current source. An upper bound on the strength is ~ 500 Gauss, based on a typical measured voltage of 2.2 mV after $\times 100$ amplification measured across a coil of ~ 140 turns with an average area of 3.36 mm^2 per loop.

Yellow Magnet

Measurements of the oscillations were all performed in Bristol on the ‘Yellow Magnet’ system which was built by Oxford and can nominally operate up to 20 T with use of the lambda plate, an additional cooling system for the magnet coil, although is more typically operated up to 18 T. The bulk of

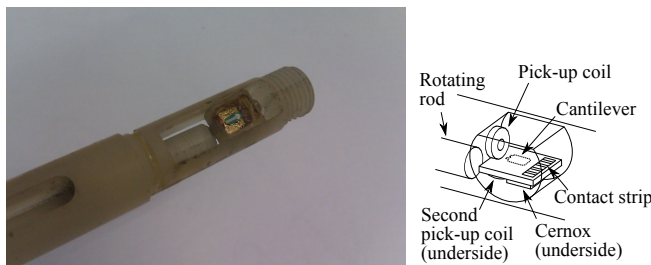


Figure 3.1.2: A photo of the Swedish rotator sample stage with cantilever in place and protective cap removed.

the cryostat sits in a bath of ${}^4\text{He}$ which takes the temperature down to the

helium boiling point of 4.2 K, and then the sealed sample space is additionally immersed in ^3He gas in a Heliox system. This system condenses the ^3He gas at the base of the chamber and pumps on it using a charcoal sorb to lower the sample stage temperature to ~ 0.3 K for several hours before it has to be re condensed. In general measurements are taken at base temperature but higher temperatures can be achieved by heating the charcoal sorb pump thus lowering the pumping rate on the ^3He bath. This technique allows access to temperatures up to approximately 2.1 K. Temperatures greater than this are possible by heating the sample through an electric heater mounted on the magnet, however it is not possible to accurately control temperature as the field ramps due to magnetoresistance effects in the measurement thermometers. Temperature is monitored at the sample by a Cernox thermometer on the sample stage, and a RuO_x thermometer which is mounted in the sample space on the cryostat but is in thermal contact with the tip of the sample stage when the stage is properly seated. Care should be taken that this is the case to ensure good cooling of the sample from the condensed ^3He . A large mismatch in the temperatures of the Cernox and RuO_x thermometers at zero field and base temperature is a good indicator of the sample stage being poorly seated. Further thermometers are situated on the 1 K pot, the sorb and sat on top of the magnet coil although the latter is only monitored when initially cooling the magnet from room temperature. All thermometers and heaters were controlled using two Neocera LTC-21 temperature controllers.

Data is collected by a Viglen Windows PC running custom Delphi software which queues measurements and records data only. No analysis is performed in the collection software. Data is saved to text files.

3.1.2 Data analysis

Angle correction

To perform angle dependent measurements, we need to first of all measure accurately the angle between subsequent measurements and second we need to determine the angle of the field compared to the basal planes of the crystal.

In order to tackle the first problem, the pick-up coils sampling the AC field described earlier are used with the measured voltage begin proportional

to the sine of the angle between the coil and the AC field. By monitoring this voltage, accurate determination of the angle between the sample platform and the field can be made and therefore the angle between subsequent measurements.

The correct angle between the large DC field and the crystal planes in the sample were determined using a post-measurement correction. Since the frequency of the quantum oscillations are field dependent with turning points at the $B \parallel [001]$ direction for approximately two dimensional samples, an even termed polynomial up to fourth order was fitted to the peaks. From the minima of the fits an angular offset was obtained which gave the final correction to the above coil measurements.

The basal angle was aligned on the cantilever by eye. This was coupled with x-ray diffraction (XRD) measurements which determined how the visual features corresponded to the crystal axes. This leads to an estimated error in basal plane alignment of around 5 % although we found evidence for greater misalignment in one case, detailed in the results.

Temperature correction

Effective mass measurements on particular extremal orbits rely on accurate temperature determination at all stages of the field sweep. On the Yellow magnet system, temperature from base of ~ 0.3 K to ~ 2 K is controlled by adjusting the He^3 sorbtion pump temperature and can be considered to be independent of field effect since the thermometer regulating the sorb temperature is outside of the strong field core. However if we consider figure 3.1.3, it is evident that there are magnetic field effects on the RuO_x, which is mounted in the base of the magnet but thermally linked with the sample, and the Cernox thermometer that sits on the sample stage. Readings from both thermometers were taken with field sweeps from zero field up to 18 T at steady temperatures 0.30 K, 0.53 K, 0.64 K, 1.06 K and 1.34 K. By interpolating between this data*, the two thermometers can be corrected to agree within ~ 0.01 K. This interpolation is however limited to temperatures below approximately 1.45 K as is shown in the figure for readings at around 1.6 K. In these cases, the less reliable method of extrapolating the readings back to zero field using a second order polynomial fit are used as demon-

*Performed using multiquadric radial basis functions from the Scipy Python library.

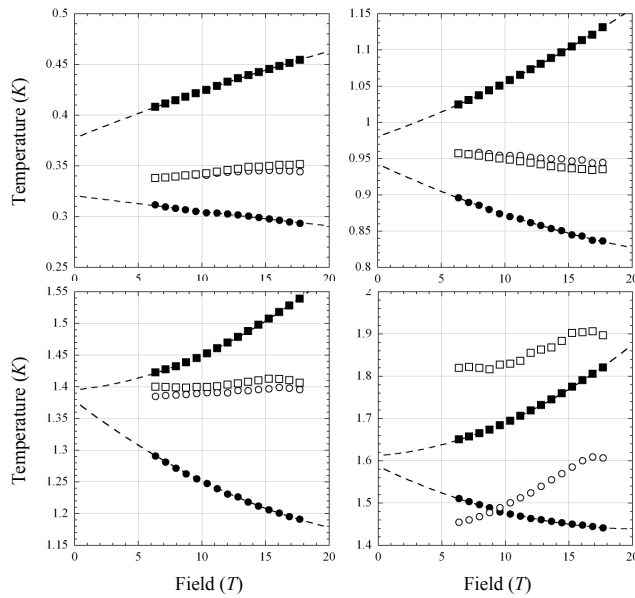


Figure 3.1.3: Some example temperature readings (filled symbols) set using the sorbtion pump heater. Also shown are corrections (open symbols) by interpolating to known values. RuOx thermometer is shown as circles, Cernox stage thermometer is shown as squares. Second order polynomial fits to the data are shown as lines extrapolated to zero to get a rough estimate of the zero field temperature value.

strated with the solid lines in figure 3.1.3. In these cases the temperature is taken to be the mean of the two extrapolated values with the differences defining the error.

Self heating effects

The resistance across the piezo-electric lever is read by driving an AC current through it and reading the voltage across it using the Stanford lock-in amplifier. Larger currents are less prone to noise problems, however too much current results in self heating and subsequently the sample platform and sample could be at a higher temperature than the nearby thermometers suggest. To ensure that this is not the case we measure oscillations at constant temperature with a variety of driving currents. Small currents should not affect oscillation amplitudes, but at some current threshold self heating effects will become apparent and the oscillations are damped as if the entire system was operating at a higher temperature. We then resume measurements using a driving current below this threshold.

Ideally the temperature chosen should be on the steep part of the LK temperature curve (eq. 2.2.13) so that even small changes in temperature manifest in observable changes in the oscillation amplitude.

Attenuation due to torque

An extra attenuation occurs due solely to the nature of the torque oscillation measurement. The attenuation factor is given by,

$$A_{\Gamma(\text{gen})} = \frac{1}{F} \frac{dF}{d\theta_{\perp}} V B \quad (3.1.1)$$

where V is the sample volume and θ_{\perp} is angle from the field direction. This can be simplified for a quasi $2d$ metal to,

$$A_{\Gamma} = |\sin(\theta)| B \quad (3.1.2)$$

where θ is the angle from the cylinder axis (usually in the c direction). This means that along the cylinder axis there will be no oscillations as $A_{\Gamma} \rightarrow 0$.

Background removal

Previous standard practice was to remove a background polynomial fitted to the field or inverse field from the raw data before taking the Fast Fourier Transform (FFT). With reference to figure 3.1.4, raw torque data taken over a range of angles* and a strong B^2 component can be observed as a result of the A_Γ term in the LK equation (marked ‘B’ in the left panel). As shown in the centre and right panels, subtracting a second order polynomial fitted to the *inverse* field leaves a large artificial angle-dependant oscillation in $1/B$ in the residual which may be misconstrued as a signal from a low frequency Fermi surface orbit, especially since there is an apparent angle dependence – no such peak is seen for the flat curves at ‘A’ and ‘C’. For this reason it is recommended to subtract a second order polynomial fitted to field rather than inverse field for torque measurements.

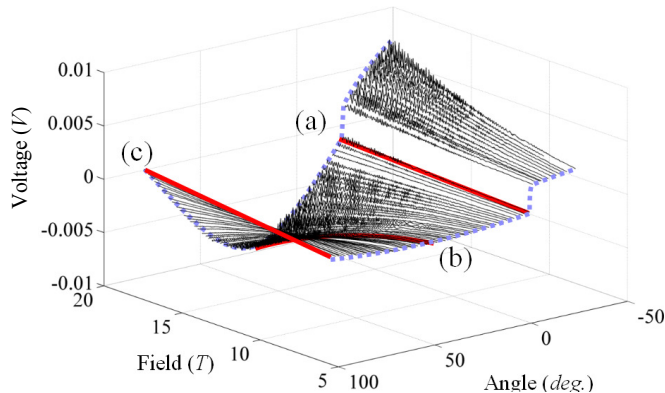


Figure 3.1.4: The angle dependence of the raw torque data clearly showing a negative B^2 background at (b) and for $\theta > 0^\circ$ and a positive B^2 background for $\theta < 0^\circ$. The background flattens out at (a), $\theta = 0^\circ$ and (c), $\theta = 90^\circ$.

3.1.3 Measuring the spin mass

The only terms in the LK equation that cause the amplitude to drop to zero as a function of angle are the torque term, A_Γ which causes a single zero when the field is parallel with the cantilever arm and the spin term A_S^\dagger . By examining the amplitude as a function of angle it is possible to determine the spin effective mass. A good determination requires more than one spin

*See section 4.3 for full details

†The angle dependence of A_S comes from variations in the band mass

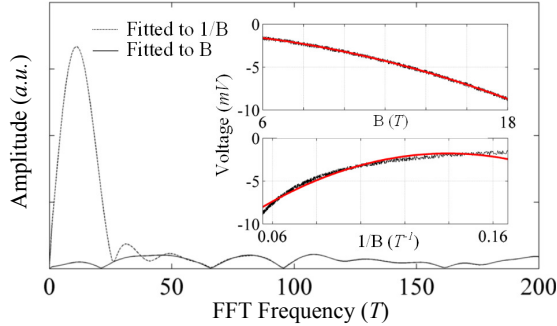


Figure 3.1.5: Insets show a 2nd order polynomials fitted to simulated B^2 background with ~ 0.5 mV of noise, similar in scale to that of (b) in figure 3.1.4. Upper inset is fitted to field and lower to inverse field. The main figure shows the resulting FFTs.

zero (i.e. a non torque term zero) to be measured since the oscillatory nature of the A_S term gives multiple solutions if we only have measured a single zero. We use n to label each of the zeros from the A_S oscillations.

In practice the determination is complicated by the fact that if the Landau levels are very well defined, the double peaks due to Zeeman splitting do not overlap and so do not interfere. This manifests as a splitting of amplitudes which do not necessarily drop to zero. In these cases the zeros have to be best determined as being within the region where a noticeable increase in the number of spin split peaks occurs. Moreover, fitting the overall shape requires all of the LK terms to be considered which makes free parameter fitting very difficult to converge. For these reasons, spin mass for this investigation is found from ansatz guesses for the values which are then fitted by inspection. Upper and lower bounds for the estimations are provided.

To the first approximation, the cylindrical approximation is used to describe the band mass in A_S , however the form of the spin term is relatively sensitive to small deviations and so fits would be much better using a more accurate variation of band mass with angle. Band mass was extracted from DFT results and was performed using Ed's MATLAB code which locates the extremal areas from the corrected BZ energy dispersion at a particular angle. Once located a small shift in energy is applied and the corresponding shift in area is used to determine the band mass using equation ???. A polynomial of appropriate order is then fitted to the curve and used in the fitting routine in place of the band mass. The MATLAB code determines

the masses with some spread in the values which caused higher order polynomial fits to oscillate at low angles within the noise. To alleviate this, a mean value was determined for each angle.

One final note is that the absolute value of the A_S term is used to fit the data since we analyse the height of the FFT peaks of the oscillations which are always positive and not the oscillations directly.

3.1.4 Extracting effective mass from the temperature dependence

Of all the damping terms in the LK equation, only A_T (eqn. 2.2.13) has any kind of temperature dependency. This term also features the thermal effective mass. By measuring oscillations at a fixed angle but with varying temperatures, the effective mass can be determined in a number of ways.

Basic LK formula fitting

The simplest technique to extract the thermal effective mass is to extract the amplitude of the oscillations from FFTs of the data at various T and then perform a least squares fit to eqn. 2.2.13. A particular problem with this approach is that it is not clear what value of B should be used since the FFTs cover a range of fields. Generally the simplest thing to do is to take the FFTs over a small a range as possible and then take the field to be equal to the averaged inverse field*.

There are two problems with this approach. First the amplitude tends to decreases with narrowing field range meaning weak oscillations may require larger field intervals. Secondly wider field ranges mean other attenuation factors — which are also functions of B — affect the amplitude across the field sweep. The primary problem in this case is the Dingle term which has an exponential dependence on B . Nonetheless, simple LK fits are usually the first port of call and serve as a first approximation to the final result. For this investigation though, since we found some disagreement within the data, we employed a couple of additional techniques described below to overcome this shortcoming.

*That is $B_{\text{av.}}^{-1} = \frac{1}{2}(B_{\min}^{-1} + B_{\max}^{-1})$

Retrofitting ansatz LK formulae

One of the primary field-dependant contributions to the oscillation amplitude is the Dingle term scattering (equation 2.2.15) which has an exponential dependence with temperature. The Dingle factor, $\alpha = -\pi pm_0/e\tau$, can be determined by fitting a simplified version of the LK equation,

$$\Gamma_{\text{sim}} = A_D(\alpha, B)\sqrt{B} \sin\left(\frac{2\pi F}{B} + \phi\right) \quad (3.1.3)$$

to oscillations which have been band pass filtered to reduce the number of contributions from other extremal orbits and hence the number of necessary fitting parameters. Once we have the Dingle term and also the peak frequency for a particular orbit, simulated oscillations are generated using the same equation but including the temperature term, $A_T(m_T^*, B)$, for a range of ansatz effective thermal masses. We then fit this to the LK equation as described in the previous section. The mass that results from the fit is different from the actual effective mass used as the LK fit has been affected by the Dingle term contribution. When we find a simulated oscillation that outputs the same effective thermal mass as the plain LK fit on the actual data we then take the ansatz thermal mass for that matching fit to be the corrected thermal mass.

The filtering used to originally separate out the frequencies is band pass FFT using a Hann window. This is adjusted in size and roll off width according to the peak. Occasionally, the peaks are too close together to effectively filter out individually and so two or three peaks were fitted at a time using a linear combination of the simplified equation above.

The initial fits were filtered using a Delphi program written by Prof. Carrington and fits to find α were performed in Kaleidagraph. Ansatz fits were found using a binary search technique using a Python script.

‘Microfitting’ the LK formula

A second technique is to filter out the individual orbit frequency by again using an FFT filter and a Hann window, and this time fitting small sections of sine curve ($\sim 1.5\text{--}3$ wavelengths) directly to the filtered torque data. This gives a field dependent value for the amplitude which can then be fitted to the standard A_T form for many values of B . The result is a plot of mass

values against B . Theoretically, these should plateau to give a constant value for the effective thermal mass.

Calculations were performed using a Python script to filter the data, perform the ‘microfits’ and then perform the LK fits. The script was tested using simulated data.

3.2 Density Functional Theory

Calculations presented in this thesis were performed using WIEN2k version 07.2 (20th Feb 2007) [73] using LAPW without the local orbitals. Unless specified, non-spin orbit calculations are presented although spin-orbit calculations were checked and did not show significant differences. The GGA according to Perdew-Burke-Ernzerhof [67] was used for the exchange distribution.

Preprocessing of the WIEN2k data into voxel form as well as the theoretical angle plots were performed using a modified version of MATLAB code written by Dr. E. Yelland. The basis for the code has been thoroughly field tested within the group over a number of years.

3.3 Calculating susceptibility

Code to calculate the Lindhard susceptibility was written in MATLAB * and early versions were tested with free electron cases in 2 and 3 dimensions with results shown in figure 3.3.1. This matches the expected free electron curves†. One caveat when dealing with the free electron case is that the energy dispersion is not periodic and as such needs to be truncated at some point in a spherically symmetric way. This truncation affects the final calculation but provided it occurs far enough from the Fermi surface then the difference is minimal. The results shown are for a calculated region that was a sphere of radius 1 with a Fermi surface radius of 0.3. Values for $\delta(=1e-9)$ and $\omega(=1e-9)$ are somewhat arbitrary given that the dispersion is simplified with $\hbar^2/2m = 1$ but are given here for posterity.

The code was adapted to accept pre-generated energy dispersions as calculated with the WIEN2k DFT software and post-processed with Ed’s

*Full code is found in appendix ??

†See, for example, page 126 and Appendix F of reference [61]

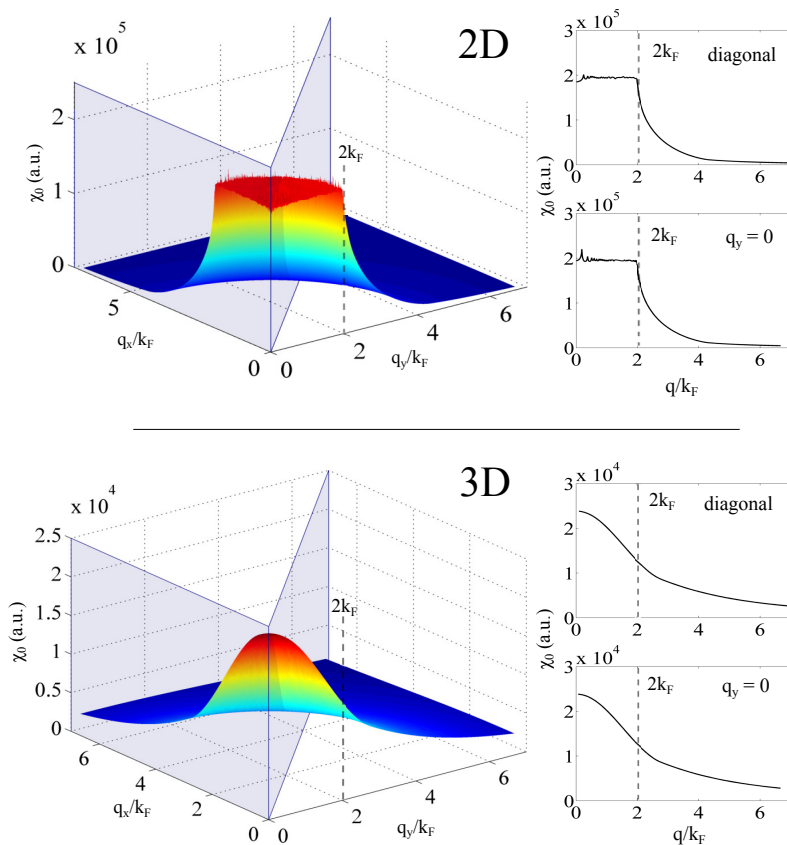


Figure 3.3.1: The real part of the Lindhard susceptibility calculations for a free electron model at $T=0$ K using the MATLAB calc_x0.m code. Top panels are for the 2D case over a 500×500 point grid, the bottom panels are for the 3D case taken over a $100 \times 100 \times 100$ point grid. Panels to the right correspond to slices through the surface plots on the left. Calculations in the 3D case are at $q_z = 0$.

MATLAB code. In this case, the dispersion is periodic and energies at the scattering vector q are obtained by simply ‘rolling’ the 3D matrix of energy values. Testing on this adapted code was performed by re-creating WIEN2k calculations on LaFeAsO_{0.1}F_{0.9} performed by Mazin et al. [25] and then comparing our own susceptibility calculations with those in the Mazin paper. A temperature smearing of 1 mRy was quoted which was equated, using the Boltzman conversion, to a temperature of 157.88 K. A similar amount of points ($55 \times 55 \times 26$) was also used.

Figure 3.3.2 show comparisons of $\text{Re } \chi_0(q, \omega)$ and $\text{Im } \chi_0(q, \omega)$ with the published results. For these calculations the values of $\delta = 1\text{e-}4$ and $\omega = 1\text{e-}6$ were determined to give the closest results from a series of trials*. The comparison shows that some of the finer structure from the Mazin paper is missing from our own calculations, for example the depression in the real part at the Γ point, however the overall shape is very similar.

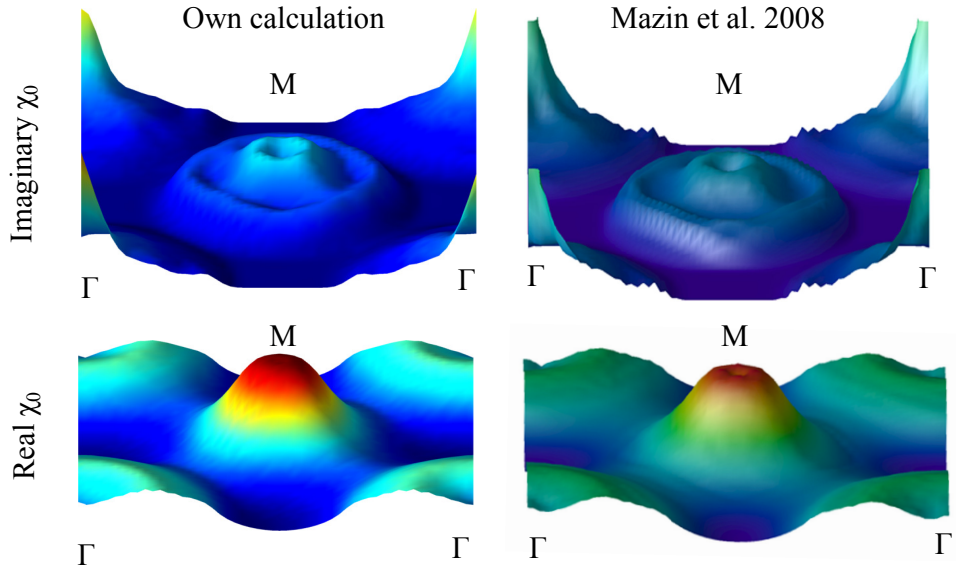


Figure 3.3.2: Right hand panels show the real and imaginary parts of Lindhard susceptibility calculations on LaFeAsO_{0.1}F_{0.9} by Mazin et al. for $q_z = \pi/c$, right panels show the same calculation performed using our own MATLAB code.

The Lindhard function is very sensitive close to the Fermi surface and finite sampling of the energy data can cause imperfect cancellation in the

*There is no indication in the paper as to the values of δ and ω used in their own calculations although we know that they are likely to be of the order of the temperature energy scale (1 mRy) or less.

calculation — particularly in the imaginary part. Applying a temperature smearing to the function is useful to gloss over the finite element size in the calculation which can cause significant spikes in the results. Figure 3.3.3 shows the smearing at a series of temperatures and that a temperature of 158 K corresponds approximately to a smearing over 2 grid intervals at the Fermi surface. An appropriate choice of temperature depends on the granularity of the model as well as the expected fine detail of the results. The Mazin investigation was into a similar quasi two-dimensional pnictide material that used a comparable number of data points and so we also opted to use 158 K for the temperature smearing.

Smearing also occurs when a finite quasi-particle lifetime, δ , is factored in and when the perturbing field is oscillatory with frequency, ω . These values are also not known a priori and so we again look to the energy scale of the spacing between grid points close to the Fermi surface for guidance.

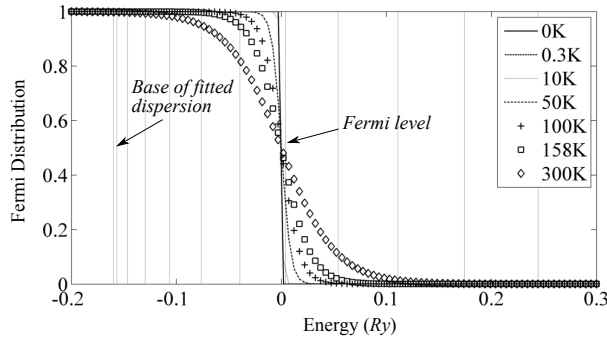


Figure 3.3.3: The Fermi distribution plotted at various temperatures. Vertical lines represent typical grid energy spacings for a free electron distribution fitted to a portion of bandstructure for $\text{LaFeAsO}_{0.1}\text{F}_{0.9}$ which rounds out just below the Fermi surface. We can see that for 158 K, the smearing spans approximately 2 grid intervals at the Fermi energy.

3.4 Measuring charge transport

In this section the Hall measurement technique and analysis of the BSCO_{2201} samples is described. Transport measurements on superconductors have been performed for over a century now and was the technique by which superconductivity was first discovered. The relative technical simplicity of the measurements makes transport measurements highly appealing considering

the wealth of information that can be extracted from a resistance curve.

The charge transport measurements performed for this thesis took place in Bristol in the Green ‘Polo’ magnet for low fields and in the LNCMI pulsed field facility in Toulouse for the high field data. Also included is analysis of data taken by group members* at the HFML in Nijmegen, Netherlands. The overarching six-probe measurement technique is used for all the transport measurements with differences chiefly in measurement geometry and apparatus.

3.4.1 Experimental apparatus

Six probe technique

For accurate measurement of voltage, and hence resistance, across a sample, two wires are not sufficient. The wires themselves have a resistance which is comparable or often larger than the resistance of the sample being measured. A solution to this problem is to instead supply the current for the voltage reading via one set of wires, and then take the voltage reading from another set meaning that a minimum of four wires and four contacts on the sample are required. To measure magnetoresistance we require the voltage wires to be placed upstream and downstream of the current, to measure the Hall effect we require the wires to be placed transverse to the current. Moreover it is useful to be able to take two transport measurements at a time so as to get an idea for the homogeneity of the sample and as well to provide some redundancy in case of breakage. Since the BSCO_{2201} samples that we studied were to have both measurements, six connection points were placed to each sample as shown in figure 3.4.1. The connections were made with $20\ \mu\text{m}$ gold wire for the current and $10\ \mu\text{m}$ gold wire for the voltage leads and attached with DuPont 4929 conductive silver paint which dries at room temperature. As shown in the figure, the sample is raised from the quartz substrate so that when the temperature drops and the wires and sample thermally contract at low temperatures, there is some give so that the ensemble does not pull itself apart.

With the four voltage legs a variety of configurations can be achieved. Measuring across (a) and (b) is the magnetoresistance configuration, (a) and (c) is the Hall configuration. It is also possible to measure across (a) and

*Dr. X. F. Xu, Dr. P. Rourke and I. Mouzoupoulou

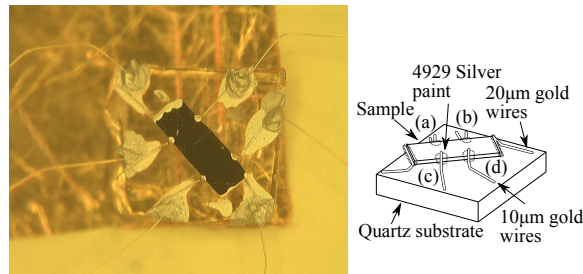


Figure 3.4.1: An example BSCO₂₂₀₁ crystal mounted on the quartz substrate. Voltage legs are labeled (a), (b), (c) and (d).

(d) and provided the field is reversed from positive to negative, both the Hall and the magnetoresistance across the sample can be extracted.

Because the connections may not be exactly aligned and because the silver paint in practice tends to whet over the edge of the sample, magnetoresistance contributions may be found in the Hall configuration and vice-versa. For this reason it is generally advised to sweep both with a positive field to obtain R_{pos} and a negative field to obtain R_{neg} where R is the resistance and separate the two out using the technique described in the analysis section.

Later as the samples has been measured many times and thermal cycling had caused the silver paint to become brittle, it was necessary to attach short, ~ 2 mm, secondary gold wires to each of the contact pads using silver paint and then attach the probe flying leads to the end of these wires. When removing the samples from the probe, this allowed the joins to be immersed in solvent held in the tip of a pair of metal tweezers at a safe distance from the sample ensemble meaning the connection could be dissolved without flexing the contact pads unnecessarily. This was done for the later measurements in the Polo magnet where the minimisation of wire loops was not so important.

Polo magnet

The ‘Polo’ magnet is an Cryogenic cryostat containing a Variable Temperature Insert (VTI) refrigeration device that allows temperature from ~ 1.4 K to room temperature to be achieved. The VTI system is a vacuum sealed chamber in to which the sample probe is inserted and sealed at the top. This chamber is insulated from a bath of ${}^4\text{He}$ in the main cryostat by a

Table 3.1: Operating the VTI under various temperature regimes.

Temperature range	Practice
1.4 K – 4.2 K	Fill VTI chamber with helium, close off needle valve and adjust the pumping rate to tune the temperature.
4.2 K – 300 K	Empty the VTI of helium and open the needle valve slightly, only pump a small amount and use the sample heater to set the temperature.

vacuum jacket. ${}^4\text{He}$ is admitted into the VTI chamber from the bath via an adjustable needle valve and is pumped through the chamber and over the sample by an external roughing pump. By almost closing off the needle valve entirely and applying a heater on the sample stage the full range of temperatures can be achieved. In practice, a couple of temperature ranges are defined which require different operational techniques and are specified in table 3.1. The VTI chamber itself has an electric heater which can be operated separately and is good for rapidly heating the system up to room temperature but is in general too coarse for measurements.

Heating is controlled by a Lakeshore 340 temperature controller with the sample stage heated from the heater output and the VTI heater controlled from the analogue output which has been boosted via a custom built amplifier unit. Sample temperature is monitored by a Cernox mounted onto the sample stage and VTI temperature from a thermometer mounted inside the VTI chamber.

The sample stage can be rotated from an external stepper motor which is supplied from a custom power source. All the instruments mentioned are controlled from a custom PC running a Delphi program written by Dr. M. French which queues runs, records and displays data. Some calculated values based on the raw data values are generated by the software, however these were not configured with the appropriate inputs. For this reason the angle and the current fields should be ignored and instead determined from raw data.

For twin voltage measurements, two Stanford SR830 lock-in amplifiers were used with one supplying the current and measuring voltage and the

second synchronised to the first and also measuring a voltage. The current supplied was supplied through a $1\text{ k}\Omega$ buffer resistor in order to approximate the supply to a current source*. The resulting voltages were passed through two passive Princeton Applied Research model 1900 low noise amplifiers set to $\times 1000$ before measurement although the actual amplification for typical resistances of $10\text{--}100\Omega$ at 33 Hz is $\times 980$.

The sample probe has a rotating stage and so after aligning the sample roughly by eye, a shallow angle sweep in a low field, typically 1 T , was performed before each measurement to make sure the sample was positioned perpendicular to the field. Some samples have an anisotropy in the transport terms and in the case of the Hall component, the effective field drops with the cosine of the angle of misalignment.

The magnet is superconducting and has a limit of 14 T or 16 T when using the additional cooling of the Lambda plate. For this thesis the measurements were only taken to 13 T to minimise the risk of a quench. The field was ramped at 1.4 T/min . The measurements presented in this thesis from the Polo magnet are all taken in the Hall configuration and are obtained by averaging both sets of contacts as described in the analysis section.

As of Feb 2012 it was determined using a Cu sample that a positive reading of the magnet power supply current (and field) corresponds to the magnetic field, B , in the Polo magnet pointing upwards. This was verified with a magnetic compass.

HFML Nijmegen

To access the normal state of the higher T_c materials we require fields larger than the 13 T available in the Polo magnet at Bristol. The HFML facility in Nijmegen has available a continuous field Bitter magnet which can reach 33 T . Data from Nijmegen in this thesis was taken in May 2010 by Dr. X. Xu, I. Mouzoupolou, Dr. P. Rourke and Dr. A. McCollam.

The magnet used at the HFML sweeps at a rate of typically 3 T/min meaning the temperature can drift significantly. The necessary heating supply for temperature control was alternated between a Lakeshore 340 temperature controller which uses input from a Cernox thermometer and a PID algorithm to supply an appropriate current or a Keithley current source

*i.e. if $(R_{\text{sample}} + R_{\text{wires}}) \ll R_{\text{buffer}}$ at all T , then the current is given by $V_{\text{excitation}}/R_{\text{buffer}}$.

which supplies a fixed current. The current source was selected on a sweep-by-sweep basis depending on which gave more stable temperatures. The analysis compensates for small drift using a simple correction described later.

The samples were measured using Stanford SR830 lock-in amplifiers which were supplying via $1\text{ k}\Omega$ resistors with a 10Ω shunt resistor. A 1 V excitation voltage was used for all samples except for B00KOD1a and B16KOD1a where 2 V excitation was used instead. The excitation frequency is set to one of the ‘magic’ frequencies* which in this case were 33 Hz, 77 Hz, 113 Hz and 123 Hz.

Field is monitored using a calibrated Hall sensor mounted on the probe which is measured using another Stanford SR830 lock-in amplifier.

LNCMI Toulouse

To obtain the highest fields we took measurements at the LNCMI pulsed field facility in Toulouse over the course of two separate visits. Here large capacitor banks are discharged through liquid nitrogen cooled copper resistive magnets to achieve short (few tens of microseconds) but strong fields of up to 60 T. Pulses at the stronger end of the scale have more potential for damaging the magnet and take longer to cool down before the next pulse can be taken and so careful consideration is required to the magnitude of pulse undertaken. Typically the cooling time is around 15 to 30 minutes. The field is measured using a calibrated pick-up coil. The first trip took place in June 2009 and involved B. Arnold, Dr. P. Rourke, Dr. B. Vignolle and Prof. C. Proust. the second trip occurred in February 2010 and involved Dr. P. Rourke, Dr. J. F. Mercure, Prof. N. Hussey, Dr. B. Vignolle and Prof. C. Proust.

The results are recorded using a pair of Stanford SR830 lock-in amplifiers after passing through an active INA103 pre-amplifier set to a gain of $\times 200$. The raw signal for the pulse duration is recorded and the lock-in algorithm is post-processed in software to avoid wasted pulses due to incorrect settings. The driving current is supplied by the lock-in amplifier and unless otherwise noted is 5 V through a $1\text{ k}\Omega$ resistor giving a current source of 5 mA. The driving frequency is typically very high to sample the data over the relatively short pulse time and for these experiments is typically 60 kHz. The data

*Frequencies that do not fall near common sources of noise or their harmonics e.g. 50 Hz from mains supply

is streamed via an optical link along glass fibres (so the chamber remain electrically isolated for safety during a pulse) to an external PC.

Cooling down to ~ 1.4 K is possible by pumping on the helium in the magnet bath. Higher temperatures could be achieved by pumping out the exchange gas and heating via a Lakeshore 340 temperature controller. Although pulses are very short lived, there is a risk of the rapidly changing field inducing a current in the leads which cause heating of the sample during the pulse. For this reason great care is taken to minimise current loops by minimising the non-twisted portion of the wires leading to the sample. Furthermore, the sample is physically jolted by the high field which can adversely affect the data, for this reason, vacuum grease is carefully applied to the sample ensemble to reduce movement.

For the first Toulouse visit, the measurements were taken in the magnetoresistance configuration, the second Toulouse visit measured the samples in the diagonal configuration.

3.4.2 Sample size determination

The length and the width of the samples were determined from calibrated optical microscope screen captures. The depth was determined post transport measurements with the help of Dr. P. Heard using a FIB. This images samples by rastering a focused beam of ions onto the sample surface and measuring the amount of ejected electrons or ions form the image. This process causes electrical charging of the surface which can in turn adversely affect the path of the highly focused incoming ions and so the sample to be imaged must be earthed in order to remain electrically neutral. For these samples, a line of 4929 silver paint was drawn between on of the contacts and the sample mounting puck.

3.4.3 Data Analysis

Isolating Hall and MR components

When measuring transport in a sample, there will always be contributions from both the MR and the Hall components due to imperfect geometry of the voltage pick up points. Since the Hall component reverses sign as the polarity of the field reverses whereas the MR component is independent of field polarity, the Hall and MR components can be separated out using the

following relations,

$$R_{\text{Hall}} = \frac{1}{2}(R_{\text{pos}} - R_{\text{neg}}) \quad (3.4.1)$$

$$R_{\text{MR}} = \frac{1}{2}(R_{\text{pos}} + R_{\text{neg}}) \quad (3.4.2)$$

where R_{pos} and R_{neg} are the resistances measured for the positive and negative field polarities. This requires data to be taken from the positive field maximum down to the negative field maximum and so for example with the Toulouse pulsed field apparatus, two pulses are required for each measurement.

Analysis of the Hall angle

In metals the Hall component does not vary with temperature, however high- T_c materials have consistently demonstrated a distinct non-trivial temperature dependence. One way to tackle this problem was pioneered by Chien *et al.* [74] who studied the Hall angle, $\cot \theta_H = \rho(T)/(R_H(T)B)$, of YBCO₁₂₃ doped with Zn impurities and found it to follow $\cot \theta_H = aT^2 + C$ where C is a constant term due to impurities. The Hall angle, $\tan^{-1}(\sigma_{xy}/\sigma_{xx})$, is thought to cancel contributions from the transport scattering rate leaving the only the transverse scattering rate and so provides a way to access the ‘actual’ Hall contribution.

Correcting for temperature variations

Figure 3.4.2 shows a comparison of typical field sweeps for the LNCMI and Nijmegen facilities and the Polo magnet. The LNCMI pulse length is ~ 150 ms and as such is not typically subject to slow temperature drift throughout the duration of the pulse. However the positive and negative pulses are typically taken with at least a 30 min interval in-between pulses meaning the positive and negative pulses may not be at precisely the same temperature. As such, a small offset is applied to bring the zero field data into line between positive and negative pulses. For the longer sweeps such as the Nijmegen data sets, an additional offset was applied to the measurement which is proportional to the temperature as detailed below,

$$R_{\text{corr.}} = R_{\text{meas.}} + F(T_{\text{base}} - T_{\text{meas.}}) \quad (3.4.3)$$

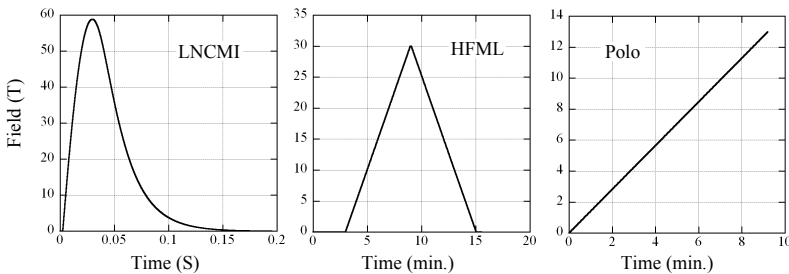


Figure 3.4.2: From left to right: Typical field sweep profiles for a pulse at the LNCMI, Toulouse, a continuous positive sweep at the HFML, Nijmegen and single positive upsweep for the Polo magnet, Bristol

where $R_{\text{corr.}}$ is the corrected resistance, $R_{\text{meas.}}$ is the measured resistance, T_{base} is the temperature that the resistance values are converged towards and F is an empirical scaling factor that brings the upsweep and downsweep data into line. The empirical factor was determined by inspection using the following method.

1. Take data where there is a clear component that is due to the temperature drift and find the appropriate factor so that it disappears. Take these data as reference benchmarks.
2. Where the temperature component is not so clear, use the reference data and make an informed estimate of the factor based on resistance vs. temperature curves in zero field and 13 T

The same factor is applied to both the positive and negative sweeps to avoid introducing artificialities into the Hall gradient. For the Polo data the temperature control was such that no correction was necessary.

Field lag correction

The Polo magnet has no sensor to measure field at the sample, with the field values being calculated from the power supply current. In the data there is evident hysteresis in all sweeps and is illustrated in figure 3.4.3 which suggests that the actual field lags slightly behind the indicated field. To correct for this, the upsweeps and downsweeps were shifted towards each other until they overlapped, typically each by around 0.2 T. Any values which were corrected to less than 0 T or more than 13 T were then not used in the analysis.

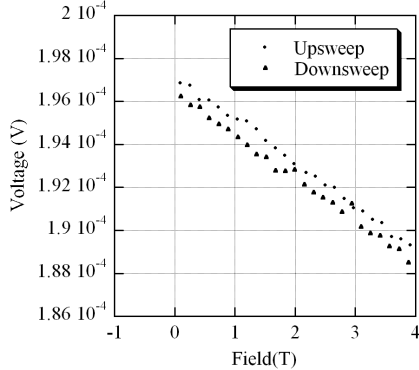


Figure 3.4.3: An example of the measured voltage of separate up and downsweeps which demonstrate the lag in actual field compared to the indicated field

Combining up and downsweeps

For all the data values there is an upsweep portion and a downsweep portion which overlap and are averaged together to reduce noise. However many portions of data have regions which drift due to changes in the out-of-phase component or anomalies such as spikes and so in these cases the regions are recorded in a configuration file and the scripts that combine the sweeps ignore the problem regions and instead use data from the counterpart sweep in isolation. Similarly, when hysteresis is encountered in the pulsed data, by convention the upsweep is ignored since it tends to be more rapid than the downsweep which generally results in more spikes and out of phase problems.

To obtain the Hall and MR components using equation 3.4.1 we need to obtain comparable data points with shared field values. To do this one of two technique was employed. For the high-field data, this is done by binning the data and taking the average of the values in each of the bins so that they share the same field values. The data taken from the Polo magnet is linearly interpolated to a predefined set of field values.

Linear fits to Hall data

Hall data for all samples were fitted using a standard linear least squares fit which was performed using Python for the Polo data and Delphi for the high-field data. A cutoff is specified so that only the data above the cutoff is fitted in the region where the linear behaviour is recovered. The cutoff value

is found by inspection of the Hall data with reference to the MR component. The precise point where linear behaviour is recovered is not always clear and so two cutoffs were specified which defined the upper and lower bounds for the start of the linear region. The limits contribute to the error in the Hall gradient with the final gradient being taken as the average of the fits from the two cutoff limits.

Normalising the high field data

The Polo data was taken in the Hall configuration and so corresponds to the true Hall voltage, whereas the data from the first visit to the LNCMI was on sample measured in the MR configuration and so represent some unknown fraction of the true Hall voltage. Moreover, the rest of the high field data was taken in the diagonal configuration meaning the voltage path was over a different portion of the sample to the Hall measurement which again means the Hall voltage is scaled by some factor. For these reasons the Polo magnet measurements were taken as the canonical absolute values for the Hall data, with the high field data scaled so that concurrent data at higher fields aligned, this process along with the variation between fits using the two different cutoff bounds define the error bars in the data.

3.4.4 Determining the doping

Three techniques have been identified for determining the doping for this thesis. The most simple and well known method for determining the doping of a material utilises the so-called ‘universal’ Tallon relation [75] which links $T_c/T_c(\max)$ to p as follows,

$$T_c/T_c(\max) = 1 - 8.26(p - 0.16)^2 \quad (3.4.4)$$

This relation was established based on measurements of $\text{La}_{2-x}\text{Sr}_x\text{CuO}_4$ (LSCO) which exploit the direct relation between Sr content and the doping (assuming stoichiometric oxygen).

The second technique, particular to BSCO_{2201} , was published by Ando *et al.* [10] in 2000 where samples of BSCO_{2201} were compared with Hall measurements of other cuprates where the carrier concentration is more easily determined, in particular LSCO was used again. The results lead to a very different relation between $T_c/T_c(\max)$ which confined superconducting

samples to a much narrower range of dopings* and is given by the following relation,

$$T_c/T_c(\max) = 1 - 254.3(p - 0.16)^2 \quad (3.4.5)$$

which was extracted from the Ando paper based on dopings determined by La concentrations.

There is however some doubt as to whether it is appropriate to compare LSCO and BSCO₂₂₀₁ measurements across the superconducting dome, especially with regards to Hall measurements, given the proximity of the van-Hove singularity in LSCO which should lead to a depression in the apparent carrier density above $p = 0.18$.

The final technique is by comparing instead BSCO₂₂₀₁ and Tl₂₂₀₁ which have very similar structures, and van-Hove singularities at much higher doping than LSCO[†]. Doping in Tl₂₂₀₁ has been well characterised in the overdoped side through recent dHvA experiments [77] which maps well to where the majority of our BSCO₂₂₀₁ samples lie. Here the doping is determined using the Tallon relation for underdoped to slightly overdoped samples with $T_c/T_c(\max)$ down to 0.71, below this value a linear relation is used: $T_c/T_c(\max) = 2.390 - 7.696p$. Again some a priori knowledge of the approximate location (i.e. overdoped or underdoped) on the superconducting dome is required and further investigation may be required to determine which side of the dome a sample lies.

*The justification being that increasing disorder suppressed T_c as you move away from optimal doping

[†]Tl₂₂₀₁ has a van-Hove singularity at a much higher doping than even BSCO₂₂₀₁. At $p = 0.26$ (or rather $p = 1.26$), ARPES measurements have shown the van-Hove singularity in Tl₂₂₀₁ lies a few eV below the Fermi energy [76]

Chapter 4

dHvA measurements on BaFe₂-P₂

This chapter presents a close to definitive measurement of the Fermiology of BaFe₂P₂ and also presents extensive data and analysis in to the thermal and spin effective masses. Nesting conditions along the (π, π) vector were investigated through calculations based on insight gained from the measurements and partial nesting was found along $q = (\pi, \pi, k_z)$ where $k_z = 0, \pi/2, \pi, 3\pi/2, 2\pi$. Given BaFe₂P₂ is not superconducting this suggests that partial nesting is not a sufficient condition for superconductivity.

4.1 Sample synthesis

The sample measured is a single crystal of BaFe₂P₂ of approximate dimensions $77 \mu\text{m} \times 54 \mu\text{m} \times 15 \mu\text{m}$ determined by optical microscope*. The crystal was grown by T. Shibauchi in Kyoto using the following technique quoted from Kasahara *et al.* [28]

“...Single crystals of BaFe₂(P_xAs_{1-x})₂ were grown from stoichiometric mixtures of Ba (flakes), and FeAs, Fe, P, or FeP (powders) placed in an alumina crucible, sealed in an evacuated quartz tube. It was heated up to 1150-1200 °C, kept for 12 h, and then cooled slowly down to 800 °C at the rate of 1.5 °C/h. Platelet crystals with shiny [001] surface were extracted ...”

For the BaFe₂P₂ sample used in this experiment, only Ba and FeP would be necessary.

* An image of the crystal mounted on the AFM cantilever is shown in the experimental methods chapter

4.2 X-Ray Diffraction

The crystalline axes of the sample were determined by XRD on a Kappa Apex II single crystal diffractometer with the aid of Dr. M. Haddow. The sample was mounted on a glass rod and held in place using vacuum grease. Clear diffraction spots are visible on the example scans shown in figure 4.2.1 although there is some evidence of a second, misaligned phase with the doubling of the spots in a small number of the scans such as the one in the top left panel. There is also further evidence of secondary phases as some peaks are doubled up in the dHvA data presented later. We have no reason to believe however that these speculated misalignments are significantly affecting the rest of the body of results nor that they affect the conclusions in any appreciable way.

Perhaps surprisingly, the straight edge of the crystal was found to lie along the [110] direction and not along the unit cell axis. This was found to be the case for a number of other $\text{BaFe}_2(\text{P}_x\text{As}_{1-x})_2$ crystals which were x-rayed later in the year.

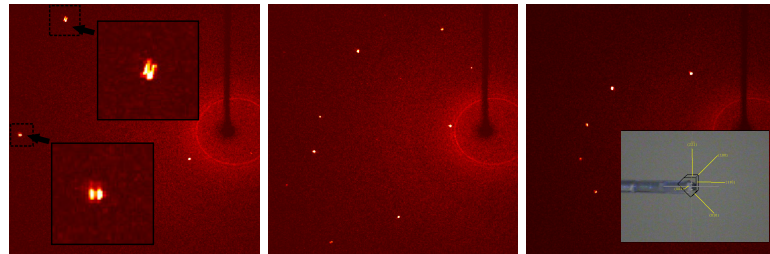


Figure 4.2.1: Panels show example diffraction patterns of the BaFe_2P_2 sample. Left shows a zoomed portion of doubled peaks indicating that there may potentially be a misalignment within the crystal. Right inset shows the labelled crystal axes superimposed on the sample which is mounted on a glass rod.

Lattice parameters are determined using the Apex II software and are presented in table 4.1 along with comparisons to two previous measurements found in the literature. The result agree within the error.

Table 4.1: Lattice parameters from XRD measurements compared with literature.

Source	a (Å)	c (Å)	z_P (% c)
X-ray	3.86(4)	12.42(9)	
Rotter et al.[78]	3.8435(4)	12.422(2)	34.59(1)
Mewis et al.[79]	3.8400	12.4420	34.560

4.3 Angle dependent measurements

4.3.1 Determining experimental parameters

Preliminary measurements showed very strong dHvA oscillations which begin at relatively low field with an example of the raw data shown in figure 4.3.1. Since it is not clear from the raw torque data where the oscillations begin, Fourier transforms were taken with small (1 T) field intervals — the interval where a clear signal is present marks the onset of oscillations. An FFT of the data for the ranges 4-5 T, 5-6 T and 6-7 T are shown in the insets of the figure. The range 6-7 T clearly shows the electron peaks at around 1500 T and 2450 T, with the higher frequency peak disappearing in the 5-6 T range and both peaks disappearing in the 4-5 T range. Further refinement suggests the onset of appreciable oscillations is around 5.6 T for the strongest electron peak. The field was ramped between 6 T and the safe maximum of 18 T for the vast majority of measurements bar some sweeps where the magnet was ramped to or from 0 T following or preceding shutdown of the magnet.

Figure 4.3.2 shows some example Fourier transforms of data taken at various field sweep rates and plotted with the frequencies shifted arbitrarily for ease of comparison. The difference in amplitude between the sweeps at 0.05 T min^{-1} and 0.1 T min^{-1} is less than 1 % whereas the difference when sweeping at 0.2 T min^{-1} is nearly 5 %. Unless otherwise stated, subsequent sweeps were performed at 0.15 T min^{-1} at the edge of where the sweep rate makes a significant difference in amplitude.

In order to make a reasonable determination of the Fermi surface of a material, an appropriate number of angle sweeps need to be made to adequately constrain the shape of the Fermi surface. Since BaFe_2P_2 is a tetragonal sys-

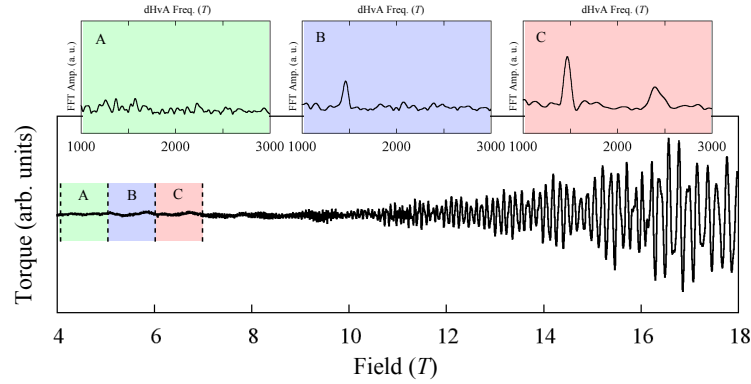


Figure 4.3.1: An example of the torque data taken with field aligned at 26° on the reverse side of the [001] to [100] angle sweep detailed later. Insets show a FFTs of the data between 4-5 T, 5-6 T and 6-7 T respectively. These intervals are marked on the main plot as A, B and C.

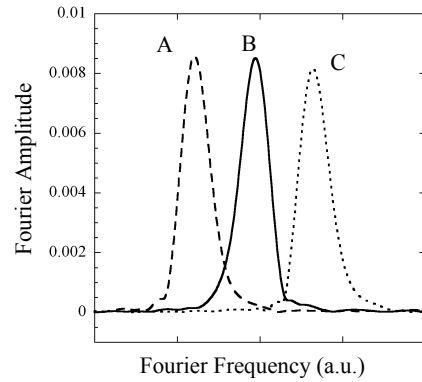


Figure 4.3.2: FFTs showing the peak from the smaller branch of band 3 taken at, A: 0.05 Tmin⁻¹, B: 0.1 Tmin⁻¹ and C: 0.2 Tmin⁻¹. The peaks are arbitrarily shifted in frequency for ease of comparison. Measurements taken with H at 10° from [001] in the [110] direction.

tem, any sweep from the azimuthal direction [001] down the polar plane effectively expands to four due to the fourfold symmetry. Measurements were taken at one degree intervals from $H \parallel [001]$ down to $H \parallel [100]$ and from $H \parallel [001]$ down to $H \parallel [110]$ which, in this system, effectively amount to eight sweeps.

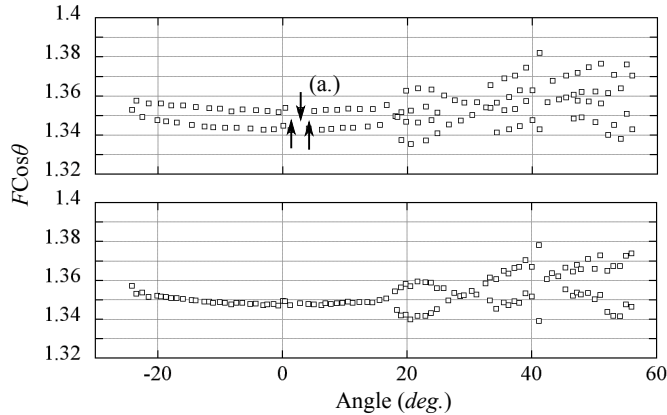


Figure 4.3.3: The plots show the $F \cos \theta$ for the α branch in the [100] direction. Top panel shows the branch with the hysteresis due to field sweep direction, the bottom panel shows the data after the linear adjustment described in the main text. Arrows at point (a.) show how the points were shifted.

In general, runs were performed with an excitation voltage of 1 V. To ensure that there was no self heating effects, runs were also performed with an excitations voltage of 0.5 V and 2 V at $T \approx 0.6$ K (where we expect the LK curve to be steep) and no change in oscillation amplitude due to heating was observed.

The magnetic field was alternatively ramped up and then down meaning subsequent measurements were generally performed with the magnetic field ramping in opposite directions. Although in theory this should not affect the results in any way, subsequent FFT peaks appeared to alternately be shifted by up to $\sim \pm 21$ T with the magnitude of the shifts being roughly proportional to frequency. Assuming that the shifts were an artefact of the measurements, a linear correction determined by visual inspection was applied of $F_{\text{corr.}} = 3 + \frac{10}{8000} F_{\text{meas.}}$ for the sweep in the [100] direction and $F_{\text{corr.}} = 0 + \frac{21}{8000} F_{\text{meas.}}$ and $F_{\text{corr.}} = 0 + \frac{18}{8000} F_{\text{meas.}}$ for the two sets of measurements performed to complete the sweep in the [110] direction. Figure 4.3.3 shows an example of these hysteretic shifts and the subsequent correction

applied.

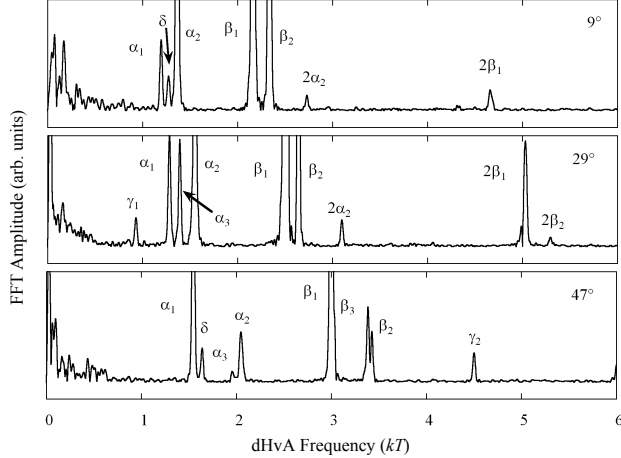


Figure 4.3.4: FFT after a second order polynomial background was subtracted at various labelled angles between [001] and [110]. The labels for peak identification are explained in the next section.

Figure 4.3.4 shows three example FFTs which show peaks from all the principal bands identified the next section. They also show first and second harmonics*. The low frequency region in figure 4.3.4 shows noise from the cantilever, but according to DFT fits performed in the next section, this region also likely contains signal from the minimum of band 1. Given that the signal from electron bands is generally small due to high scattering rate, we were not able to extract a convincing Fourier peak.

Figure 4.3.5 shows the FFT frequency of peak data multiplied by $\cos \theta$ after having the angle determined as described in section 3.1.2. Signal can be observed up to relatively high angles with peak observed almost up to 80° in the [110] direction which, along with the observation of third harmonics, and the onset of oscillations in relatively low field is testament to the high quality of the crystal.

The left panel in figure 4.3.6 shows the measured rotation data (circles) for the plots towards the [100] direction and in addition the data from the $x = 0.63$ data in the $\text{BaFe}_2(\text{P}_x\text{As}_{1-x})_2$ series multiplied by amounts commensurate to the expected shifts in the Shishido paper [49] (black squares). We can see that while the size of the areas changes between the two values, the overall shape of the $x = 0.63$ data matches reasonably well with the

*Third harmonics were also identified in other FFTs, these are shown in figure 4.3.5.

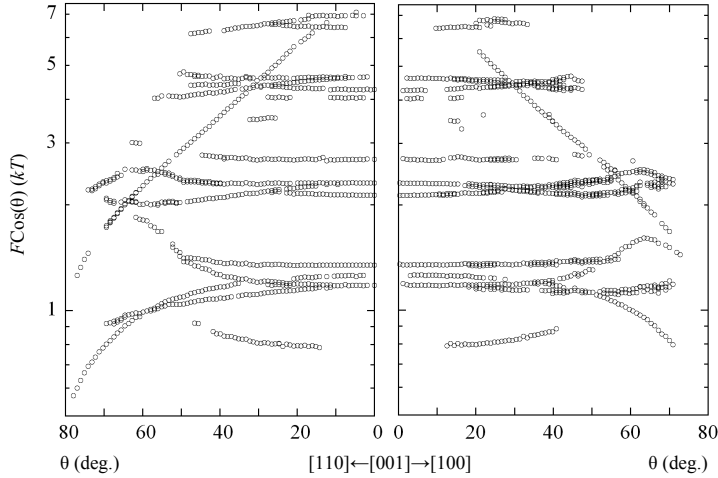


Figure 4.3.5: Peaks identified by varying the field range, window type and background polynomial. Left panel shows data taken with the field parallel to [001] down to [110], the right panels shows [001] to [100].

data for $x = 1$ for bands 2, 3 and 4 at least. Assuming that nothing exotic happens in the intermediary, we can extrapolate the shape of these Fermi surfaces across the range by applying the known electron Fermi surface areas and the compensation condition. This is explored further in the next section.

Rigidly shifting the calculated DFT energies

The right panel of figure 4.3.6 shows the DFT calculations performed using the augmented plane wave method plus local orbits method method as implemented in the WIEN2k package [73]. The unit cell used was that measured by Mewis et al. which are listed in table 4.1 and the subsequent DFT calculations were processed into rotation plots using Ed's MATLAB code. Results are shown superimposed over the measured data. By factoring the frequency with $\cos \theta$ it becomes clearer which of the orbits is a maximal extrema and which is a minimal extrema. Using this knowledge as well as clues from the Fourier amplitude of the measured data, it was possible to separate out individual bands which have been colour coded and labelled — according to literature convention — as specified in table 4.2. Minimal extrema are sub-labelled 1, maxima are sub-labelled 2. The points marked in grey are the harmonics which were identified by overlaying the measured

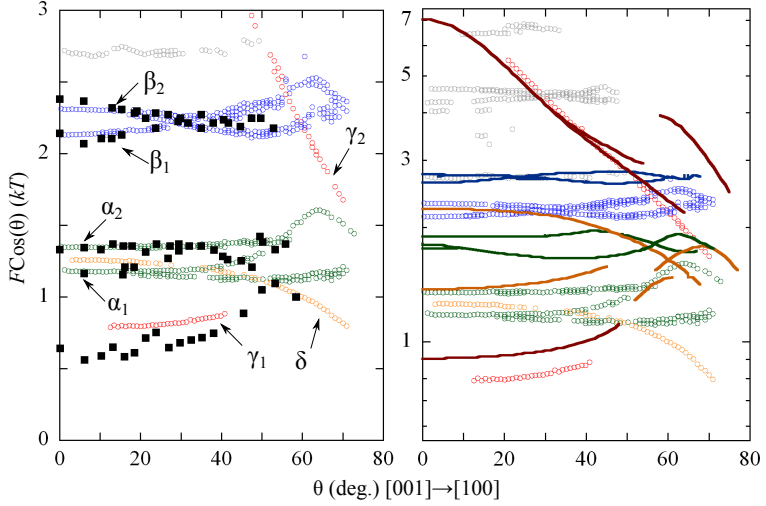


Figure 4.3.6: Left panel shows the measured data with points overlaid from $\text{BaFe}_2(\text{As}_{0.37}\text{P}_{0.63})_2$ [51] with the α and γ frequencies multiplied by 1.33 and β frequencies multiplied by 1.19 commensurate with known shifts from literature. Right panel shows DFT calculations (lines) overlaid on top of measured FFT data (circles). Data is colour coded according to the corresponding bands. Points in grey are harmonics.

data on itself after doubling and tripling of the frequency.

As with previous DFT calculations in the $\text{BaFe}_2(\text{P}_x\text{As}_{1-x})_2$ series, the calculated values are consistently higher than the measured values [49]. The exception in this case is γ_2 which is not much different from the calculated values.

As is shown in the right panel of figure 4.3.6, the rotation plots from the DFT calculations match up qualitatively with the data but do not match up quantitatively – the electron bands overestimating the size of the measured

Table 4.2: A summary of the Fermi surface labelling used.

Band Num.	Label	Colour	Type
1	δ	Orange	hole
2	γ	Red	hole
3	β	Blue	electron
4	α	Green	electron

Table 4.3: Rigid energy shifts required to match the DFT calculations with the measured data.

Band	Energy Shift (Ry)
1	-0.0083
2	Wide 0.0
	Narrow -0.0038
3	0.0043
4	0.0050

extremal orbits.

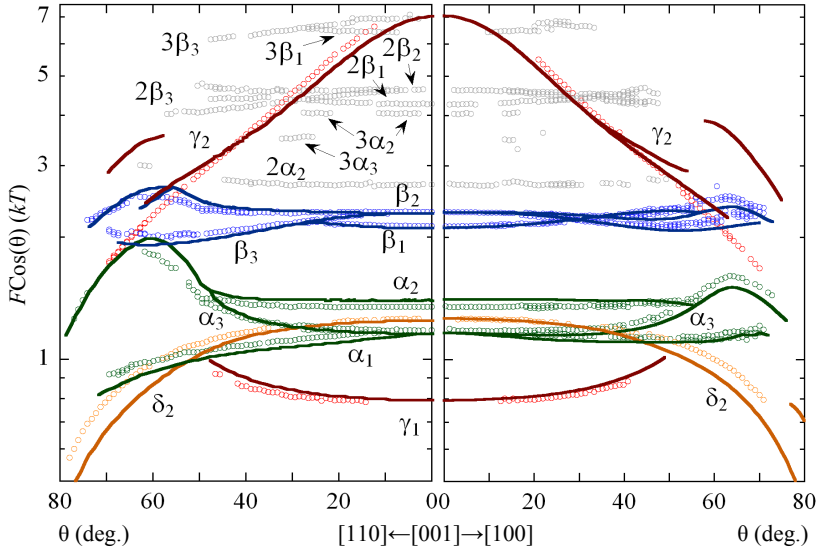


Figure 4.3.7: dHvA frequencies multiplied by $\cos(\theta)$. Solid lines are rigidly shifted DFT calculations, open circles are measured data. H field directed along [001] towards (a.) [001] → [100] and (b.) [001] → [110].

In order to obtain the correct shape of Fermi surface, the DFT calculations need to be tweaked. One technique is to apply small band-specific rigid energy shifts, which, in most cases is enough to bring the DFT in line with the experimental data. Figure 4.3.7 shows the rotation plots which rotate towards both the 100 and 110 directions along with appropriately shifted calculations. Table 4.3 lists those energy shifts.

Band 2 in this case has two separate shifts specified in two different

regions of the BZ. The rotation plot for the wider orbit located at the edge of the BZ was calculated with no energy shift and the narrow part of the Fermi surface around the Γ point was calculated with a shift of 0.0038 Ry. This provides a reasonable match for the rotation plot where we can apply the shift to the two regions discretely, however it proves problematic when we wish to study intermediate areas since it is not clear how the Fermi surface varies between the two regions. A technique for applying appropriate energy shifts throughout the BZ is explored in the next section.

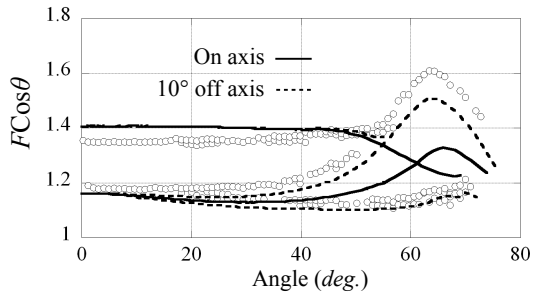


Figure 4.3.8: Portion of the measured FFT peaks taken towards the '[100]' direction. Superimposed is angle plots calculated from DFT. Solid is calculated for the field rotating down to [100], dotted is rotated down to 10° off [100] in the basal plane.

For the [100] direction it became apparent from the fact that the DFT and the measured curves were qualitatively different that the field was not perfectly aligned with the [100] axis of the sample. Figure 4.3.8 shows how the measured data (circles) does not align well with the plots calculated for rotations towards [100] (solid) but does align well with plots towards an axis which is rotated 10° within the *ab*-plane from the [100] direction. A 10° misalignment is within the estimated basal alignment error for the microscope images. The data will continue to be labelled as in the [100] plane however for convenience.

In the first place, these shifts were applied as they conveniently and effectively corrected the Fermi surface energies, however the question arises as to whether there is any physical significance to be attached to them. The technique of rigid energy corrections has been applied to previous measurements on LaFePO [80] and SrFe₂P₂ [52] both of which are highly two dimensional systems that exhibit relatively strong nesting characteristics. This is

in contrast with measurements on CaFe₂P₂ [81] which has a highly three dimensional Fermi surface and no nesting vector. Furthermore the bulbous area of the three dimensional hole surface in BaFe₂P₂ which does not nest requires no shifting of the Fermi surface to match DFT calculations, whereas the nested neck portion does require a shift. This correlation between nesting and shifts in calculated energy make the spin-density-wave fluctuations that are associated with the nesting phenomena an obvious candidate for the cause of the discrepancy between DFT calculation and experiment.

Shifting the DFT calculations proportional to orbital character

Figure 4.3.9 shows the partial orbital character for each of the bands along the path of Fermi surface contour in a [110] slice through the BaFe₂P₂ BZ as a function of k_z . The top row of plots show the character broke down by atomic contribution, the middle row is broken down by the *s*, *p*, *d* and *f* contributions to the iron contribution and the bottom row breaks down the iron *d* character into its sub orbitals.

The interstitial regions account for about 20–32 % of the electron band character along suggesting that they may have higher mobility than the hole bands. Which would explain why the oscillations from the electron bands are much stronger in the dHvA. The hole bands range between 8–18 % with band 1 being more mobile around the Γ point whilst band 2 being higher around the Z point at the top edge of the BZ.

We can see the vast majority of Fermi surface character is due to the iron atomic contributions with some phosphor for bands 2 and 3 which corresponds well to the notion of FeP conducting planes. For all the bands, the overwhelming majority of the contribution from the iron atoms is from the *d* orbitals and so other contributions are ignored.

Band 2 has very little basal-plane d_{xy} and $d_{x^2y^2}$ character close to the Fermi level but shows a significant amount of d_{z^2} character at the wide region of the Fermi surface and $d_{xz}+d_{yz}$ character at the narrow region. Evidently, energy shifts could be applied which are scaled to either the d_{z^2} and $d_{xz}+d_{yz}$ orbital character in order that we obtain a smooth energy shift transition between the narrow and wide regions discussed previously.

Energy shifts were applied across the full three dimensional BZ for band 2 using the following two scalings which were determined by trial and error

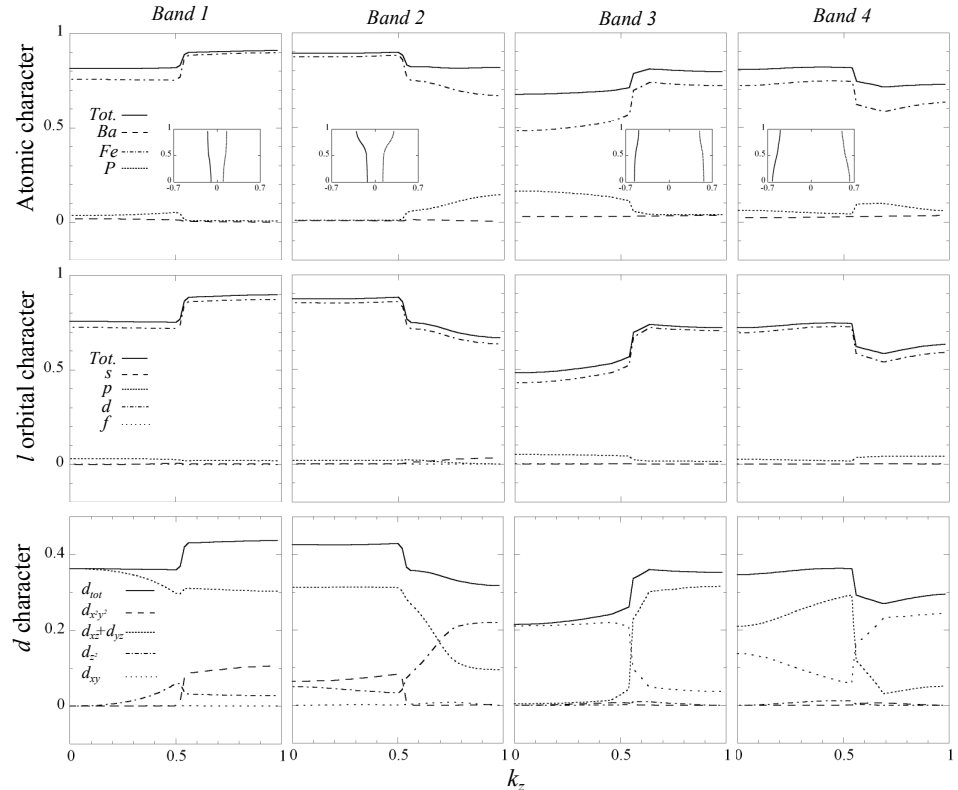


Figure 4.3.9: Partial orbital characters along the Fermi surface contour in the 110 slice (shown in insets) vs. k_z . Top row is the character broken down by each atom, middle row is the iron contribution broken down into the l orbital contributions, the bottom row is the iron d orbital contributions broken down into its suborbitals. The leftover region in the top row is made up of the interstitial regions outside of the muffin tin spheres which are not associated with any particular atom.

fitting of the data,

$$d_{z^2} : \Delta\epsilon = 0.002 - 0.0052 \left[1 - \frac{\epsilon - 0.033}{0.2205 - 0.033} \right]$$

$$d_{xz} + d_{yz} : \Delta\epsilon = 0.002 - 0.0052 \left[\frac{\epsilon - 0.0946}{0.3135 - 0.0946} \right]$$

Note that these scalings ensure that the energy shift applied varies between -32 mRy and 2 mRy which are slightly different to the values applied when rigidly shifting the band. This is due to the fact that the Fermi surface area measured in the narrow region is affected more and more by the size of the Fermi surface in the wide region (and vice-versa) as the azimuthal angle gets higher. The calculated area deviates from the measured area which results in the crossing of the calculated rotation plot with the measured rotation plot shown in the first panel of figure 4.3.10. So when the rigid shifts were being determined, values were chosen which best lines up along the full length of the curve – one which will be slightly lower than if we were to match the plots exactly at $\theta = 0^\circ$.

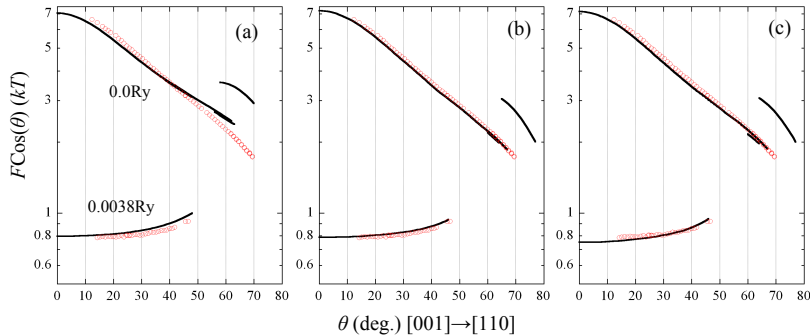


Figure 4.3.10: dHvA frequencies for band 2 multiplied by the cosine of the angle of the H field. H field directed along $[001] \rightarrow [110]$. Open circles are measured data, solid lines represent (a) rigidly shifted DFT calculations, (b) DFT calculations shifted proportional to d_{z^2} orbital character, (c) DFT calculations shifted proportional to $d_{xz} + d_{yz}$ orbital character.

The second and third panels of figure 4.3.10 show the rotation plots calculated with the energy shifts applied proportional to d_{z^2} and $d_{xz} + d_{yz}$ orbital character respectively. We observe a much better alignment of the measured and calculated data for all angles. Figure 4.3.11 shows the Fermi surfaces before and after shifting using the rigid energy shifts for bands 1,

Table 4.4: Volumes of the shifted and unshifted Fermi surfaces as a percentage of BZ volume.

Band	Unshifted	Shifted d_{z^2}	Shifted $d_{xz}+d_{yz}$
1	5.54%	2.28%	2.28%
2	10.37%	9.74%	9.64%
3	(-)9.58%	(-)7.89%	(-)7.89%
4	(-)6.39%	(-)4.49%	(-)4.49%
Total	-0.065%	-0.352%	-0.450%

3 and 4 and using shifts scaled to d_{z^2} orbital character for band 2. Figure 4.3.12 shows the assembled unit cell for BaFe_2P_2 from the corrected DFT calculations and figure 4.6.1 shows the shifted band structure for the bands that cross the Fermi level.

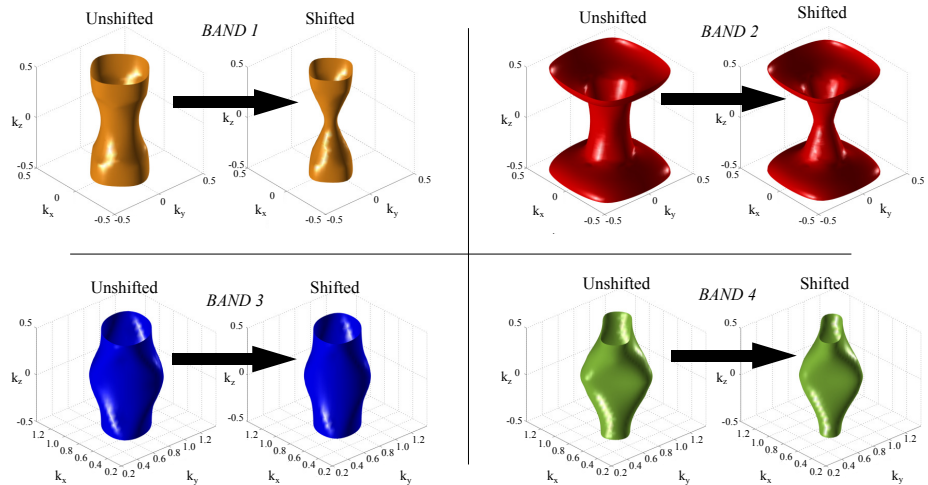


Figure 4.3.11: Comparison of Fermi surfaces according to DFT calculations both before and after shift corrections are applied. Rigid shifts are applied to bands 1, 3, 4 and shifts proportional to d_{z^2} character are applied to band 2.

The final corrections show the DFT calculations being adjusted in size only for the electron and inner hole surfaces with overall shrinking of volume, the outer hole surface is adjusted in shape as well. Volume calculations as a percentage of the BZ are given for each of the Fermi surfaces before and after shifting in table 4.4, The volumes compensate better before the shifts

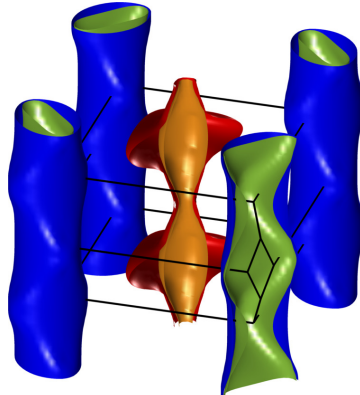


Figure 4.3.12: Fully assembled Fermi surface in the first BZ of BaFe_2P_2 as determined by DFT calculations corrected by either rigid energy shifts (bands 1, 3, 4) or shifts proportional to d_{z^2} character (band 2)

by a small amount ($\sim 0.4\%$) with the shifts proportional to $d_{xz}+d_{yz}$ being slightly closer to the unshifted volume.

4.4 Obtaining the Fermi surface for members of the $\text{BaFe}_2(\text{P}_x\text{As}_{1-x})_2$ series

We can use existing literature measurements of the Fermi surface at $x = 0.38$ from Yoshida *et al.* [82], $x = 0.63$ from Analytis *et al.* [51] and a range between $0.4 < x < 1.0$ from Shishido *et al.* [49] to obtain an approximate relation for the size of Fermi surface orbits across the $\text{BaFe}_2(\text{P}_x\text{As}_{1-x})_2$ series. Figure 4.4.1 shows the maximum and minimum orbit sizes with the field along the c -axis from these papers along with data presented in this thesis. It may be possible to apply a linear scaling to determine the intermediate orbit sizes however there are a number of assumptions that need to be made.

Firstly we cannot apply Vegard's law beyond a structural transition in the series meaning we cannot extrapolate to the orthorhombic state at the low x end of the phase diagram. The measurement by Yoshida et al. at $x = 0.38$ roughly coincides with the edge of the orthorhombic transition as shown in figure 1.2.2 but was found to be tetragonal and so we can use to to define the lower limit for the extrapolation at low temperatures. There is also a so called 'collapsed tetragonal phase' which occurs in the BaFe_2 -

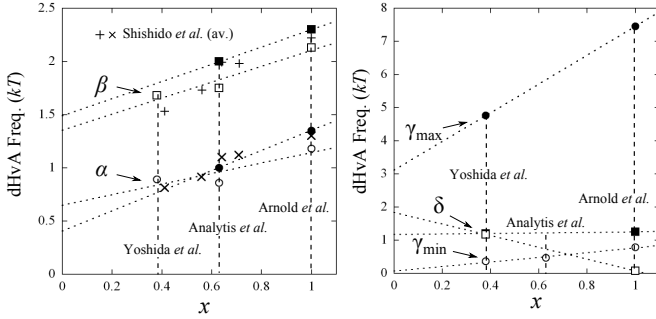


Figure 4.4.1: Left panel shows the trend in electron orbit size at $\theta = 0^\circ$ over the series, right panel show the hole orbit size trends. Dotted lines show linear fits to the data.

As_2 at a pressure 27 GPa [83] at 33 K which could present a problem as we apply chemical pressure. The optimal T_c of BaFe_2As_2 under pressure is ~ 5 GPa [46] and optimal T_c for the $\text{BaFe}_2(\text{P}_x\text{As}_{1-x})_2$ series is $x \sim 0.3$, and so we can very approximately place $x = 1$ corresponding to ~ 7 GPa which is about half of that required for the collapsed phase transition. Moreover the author is not aware of any reports of the collapsed phase being observed in the $\text{BaFe}_2(\text{P}_x\text{As}_{1-x})_2$ series at atmospheric pressure and so we assume that this is the case.

There is also the problem of the third hole surface around the Γ point which appears in DFT calculations. Although it has not been observed in any of the measurements, this is to be expected since electron surfaces generally scatter more and so have a weaker signal to electron pockets and also it may be close in size and shape to other hole surfaces making it difficult to pick out with current ARPES resolution.

Looking at figure 4.4.1 we see some inconsistencies which may also throw some doubt onto such a linear fit. Key points from Yoshida *et al.* are measured from ARPES and not dHvA. As they were measured at 10 K, this means that the Fermi surface is measured in the superconducting state and not the field suppressed normal state which is the case for the dHvA data. It is not clear if this results in different Fermi surfaces. It also should be noted that a linear extrapolation of δ suggests that it will become more three dimensional as it goes below $x = 0.38$, however this does not appear to be supported by the DFT results which show it remaining quasi-two dimensional.

Table 4.5: Linear relations to determine orbit sizes. Coefficients are of the form $F = mx + c$.

Orbit	m	c
δ_{\max}	0.081	1.169
δ_{\min}	-1.766	1.841
γ_{\max}	4.339	3.111
γ_{\min}	0.698	0.071
β_{\min}	0.749	1.352
β_{\max}	0.811	1.489
α_{\max}	0.495	0.646
α_{\min}	0.946	0.404

With the above (many) caveats in mind, we can determine a series of linear laws which would approximately determine the orbit sizes for $0.38 < x < 1.0$ by applying fits to the data in figure 4.4.1. The results of these fits are given in table 4.5.

4.5 Harmonic parametrisation of the Fermi surface

An analytic form for the Fermi surface can be obtained using a harmonic expansion of sin and cosine functions as described by Bergemann *et al.* [84]. Primarily this was done so as to provide a convenient way to reconstruct the Fermi surface without necessitating DFT calculations however the coefficients also bear some relation to the tight binding model hopping integrals. For strongly correlated systems the tight binding model is generally a poor one to use as it entirely ignores electron correlations. Nonetheless the expansion is as described as,

$$k_F(\phi, \kappa) = \sum_{\substack{\mu, \nu \geq 0 \\ \mu \text{ even}}} k_{\mu\nu} \cos \nu \kappa \begin{cases} \cos \mu \phi & (\mu \mod 4 = 0) \\ \sin \mu \phi & (\mu \mod 4 = 2) \end{cases} \quad (4.5.1)$$

where k_F is the Fermi surface in k-space, $\kappa = ck_z/2$, c is the unit cell height and ϕ is the polar angle.

The two dimensional fits were performed using a least square fitting

routine using MATLAB on the DFT data shifted as described in the previous section. The number of terms for the fits were increased until the residuals ceased to change appreciably. Fit parameters are presented in table 4.6. Due to the skewed nature of the k_z dispersion of the outer hole surface 20 terms were necessary to obtain a reasonable fit to the corrected DFT data however electron surfaces could be fitted well with 9 terms and the inner hole surface with 10 terms. The final analytical function was then used to create a false energy dispersion on a discrete grid of k -points. Extremal orbits were then calculated as a check of how well it matches the original data. The results of this are presented in figure 4.5.1. As you can see, although the fits were to the modified DFT calculations, the fits are also reasonably accurate at modelling the measured data.

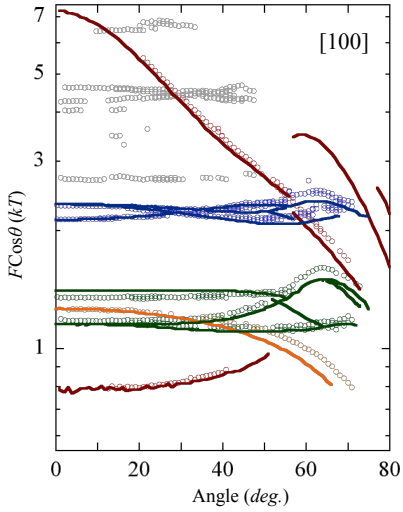


Figure 4.5.1: Rotation plots for the tight-binding fits calculated from the c-axis down towards [100].

4.6 Susceptibility calculations

To verify that we do get enhanced susceptibility, which may lead to a spin-density wave state, the q -dependant susceptibility – described in section 2.3.1 – was calculated. Since the Lindhard function takes the sum over all energies in the BZ, there may be some concern that the rather crude adjustments to the DFT calculations performed in the previous section – which have

Table 4.6: Harmonic expansion fit parameters performed on the shifted DFT Fermi surfaces

Factor	α	β	γ	δ
k_{00}	1.90796e ⁻¹	2.59538e ⁻¹	2.58282e ⁻¹	1.35031e ⁻¹
k_{02}	-1.32049e ⁻²	-1.01956e ⁻³	0	0
k_{04}	9.24279e ⁻⁴	4.28603e ⁻⁴	-1.01085e ⁻²	1.95065e ⁻³
k_{20}	4.30196e ⁻⁴	-1.51226e ⁻⁴	-1.46090e ⁻¹	-6.75502e ⁻²
k_{22}	3.23365e ⁻⁴	1.91896e ⁻⁴	0	0
k_{24}	-9.30815e ⁻²	-4.23320e ⁻²	1.13859e ⁻²	-5.31077e ⁻³
k_{40}	-1.64499e ⁻²	5.02893e ⁻³	6.15148e ⁻²	-5.70262e ⁻³
k_{42}	-1.49159e ⁻²	-7.07858e ⁻³	0	0
k_{44}	-6.14076e ⁻⁴	-2.86767e ⁻⁴	-9.49526e ⁻³	5.28982e ⁻³
k_{60}	0	0	-1.85170e ⁻²	-1.22242e ⁻³
k_{64}	0	0	-9.04247e ⁻⁴	-2.82851e ⁻⁴
k_{80}	0	0	-6.79607e ⁻³	-2.22767e ⁻³
k_{84}	0	0	1.61746e ⁻³	-1.90500e ⁻³
k_{100}	0	0	1.07007e ⁻²	0
k_{104}	0	0	7.97948e ⁻⁴	0
k_{120}	0	0	-3.89161e ⁻³	0
k_{124}	0	0	-1.57292e ⁻³	0
k_{140}	0	0	-1.81052e ⁻³	0
k_{144}	0	0	3.81207e ⁻⁴	0
k_{160}	0	0	3.04268e ⁻³	0
k_{164}	0	0	1.14420e ⁻³	0
k_{180}	0	0	-1.07753e ⁻³	0
k_{184}	0	0	-4.92181e ⁻⁴	0

only been verified to be correct for energies at the Fermi surface – may give erroneous results. However the nature of the Lindhard function means that far greater weight is given to energies that are near the Fermi surface. Figure 4.6.1 shows the ‘spaghetti plot’ with the energies tweaked as described in the previous section. We see that there are discontinuities in band 2, most notably between Z and Σ_1 , due to the correction applied proportional to the d_{z^2} character, however these are reasonably far from the Fermi level and so should not affect the calculations significantly.

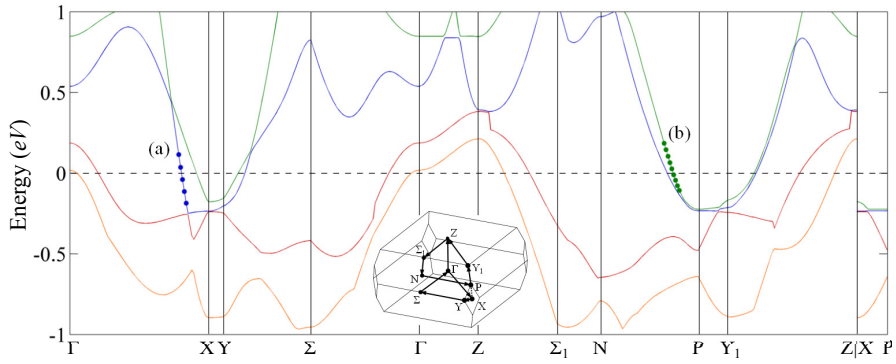


Figure 4.6.1: Band structure for the bands that cross the Fermi surface shifted to fit the dHvA data. (a) and (b) give an idea of the granularity of the WIEN2k calculation at the Fermi surface. Inset shows the path around the BZ.

Calculations were performed using the `calc_x0.m` code described in section 3.3 using a $93 \times 93 \times 93$ grid of energy values that covered the first BZ. We will need to smooth over the granularity of the WIEN2k band model since for the imaginary part at least, the calculation is very sensitive to slight imperfections in cancellation near the Fermi energy. Referring to figure 4.6.1, there are two regions in the marked (a) and (b) which show points around the Fermi level as they are spaced in the $93 \times 93 \times 93$ model. (a) is particularly steep and has a $\Delta\epsilon/\Delta\text{pt.} = 0.0760 \text{ eV}$ and (b) is more typical of the gradient at the Fermi level and has $\Delta\epsilon/\Delta\text{pt.} = 0.0368 \text{ eV}$. So the energy scale that will need to compensated is $\sim 2\text{-}5 \times 10^{-3} \text{ Ry}$.

Susceptibility was calculated for a wide range of magnitudes of δ and ω in order to gauge qualitative behaviour with the resulting plots shown in figure 4.6.2. Both the real and imaginary parts undergo qualitative changes as the parameters are adjusted above the spacing corresponding to the typical gap in energy between points. The imaginary part also undergoes a qual-

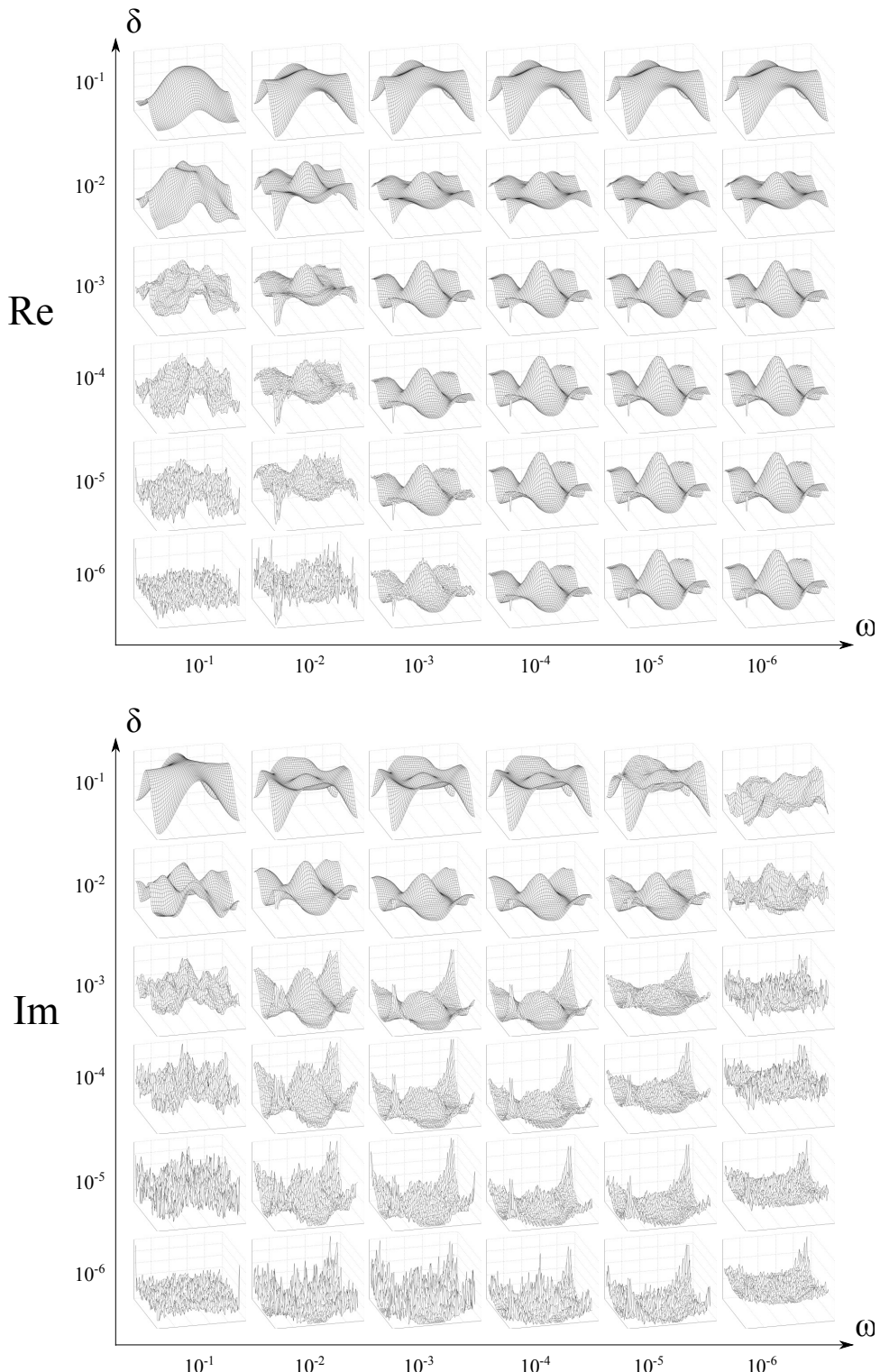


Figure 4.6.2: Qualitative plots of the real and imaginary part of the Lindhard susceptibility calculated at $k_z = \pi$ for $T = 157$ K and a range of δ and ω values.

itative change when ω falls below 1×10^{-5} Ry and there is also an increase in noise when δ falls below a similar energy threshold. We continue using $\delta = 1 \times 10^{-3}$ and $\omega = 1 \times 10^{-3}$ which correspond approximately the energy scale of the spacing as well as the energy scale of the temperature smearing.

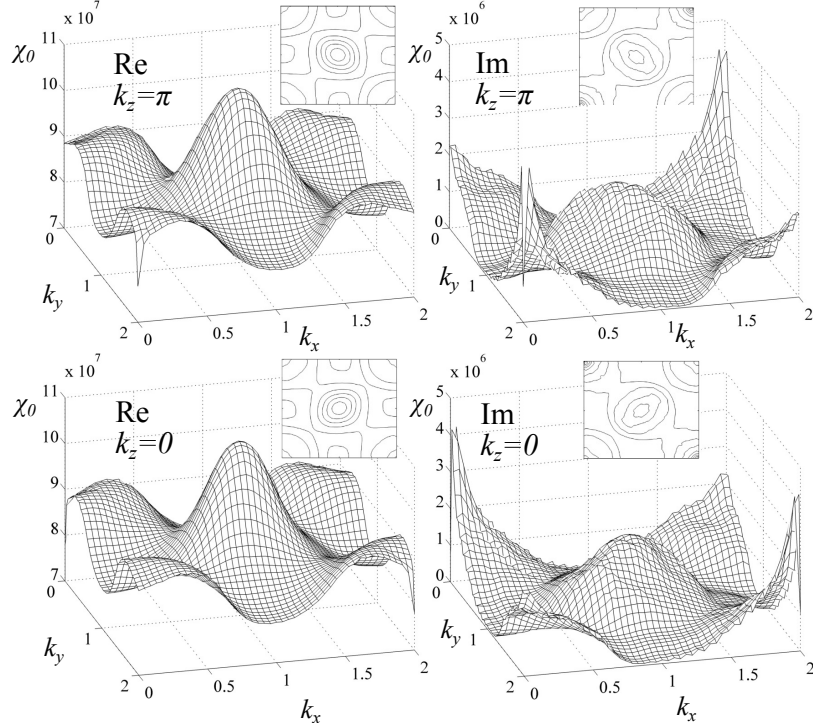


Figure 4.6.3: Real and imaginary part of the Lindhard susceptibility are plotted on the left and right respectively. Upper panels are at $k_z = \pi$ and lower are at $k_z = 0$. For these calculations $\delta = 1 \times 10^{-3}$, $\omega = 1 \times 10^{-3}$ and $T = 157.88$ K. Insets show contour plots for the respective surface plots.

The upper panel of figure 4.6.3 shows the quantified plots for the real and imaginary parts of the susceptibility at the chosen values of δ and ω . The contour plots in the insets show the two-fold symmetry due to the choice of $k_z = \pi$. Unlike LaFeAsOF where the two dimensional approximation is a good one, this is not necessarily the case for BaFe_2P_2 which features a strongly three-dimensional hole band and some warping of the electron bands. The lower panels present the same calculation performed at $k_z = 0$ which shows little change other than a rotation of the susceptibility bias due to the screw symmetry of the electron bands.

To verify that there is indeed a nesting conditions at some k_z for $q =$

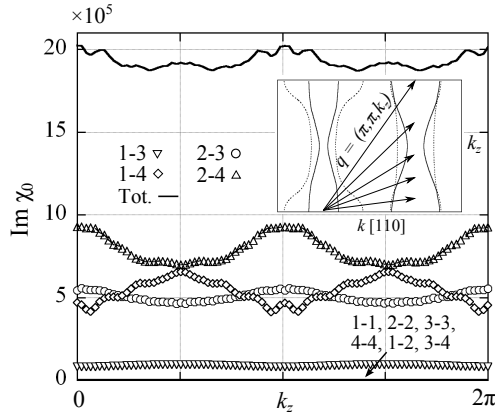


Figure 4.6.4: Left panel shows the imaginary part of the Lindhard susceptibility between bands summed with their reciprocals for $q = (\pi, \pi, k_z)$ over the height of the BZ. We see enhancements at $k_z = \pi/2, 3\pi/2$ for bands 1-4 and 2-3 and at $k_z = 0, \pi, 2\pi$ for bands 2-3 and 2-4.

(π, π, k_z) figure 4.6.4 presents the imaginary part of the susceptibility vs. k_z for a range of nesting vectors. Each coupling of bands is summed both ways — e.g. 4-1 is summed with 1-4 — and plotted in order to obtain the residual difference due to ω . Unsurprisingly, we see that self coupling results in very little weight with hole-hole and electron-electron coupling also resulting in little weight. The strongest component is due to bands 2-4 which also demonstrates a strong enhancement of around 25% at $k_z = 0, \pi, 2\pi$. Band 2 also couples strongly with band three at the same q vectors with around a 17% enhancement. Band 1 couples strongly with band 4 but at $k_z = \pi/2, 3\pi/2$ with the largest enhancement of around 38%. Band 1 also couples less strongly with band 3 at the same k_z with an enhancement of around 15%. The total susceptibility is determined mostly by the coupling of band 2 but only has a relatively moderate enhancement of around 7.4% at $k_z = 0, \pi, 2\pi$.

Figure 4.6.5 shows cross sections of the final corrected Fermi surfaces showing the basal-plane at the bottom of the unit cell ($k_z = 0$), quarter of the way up, ($k_z = 0.25$) and halfway up ($k_z = 0.5$). The inner hole surface (band 1) at $k_z = 0.5$ directly matches the size and shape of the inner electron surface (band 4) at $k_z = 0.25$ which is the likely cause of the strong enhancement observed in the susceptibility. Moreover, the bands share similar predominant $d_{xz} + d_{yz}$ orbital character. The strong enhancements between

bands 2 and 4 are also shown in the figure as a dashed arrow.

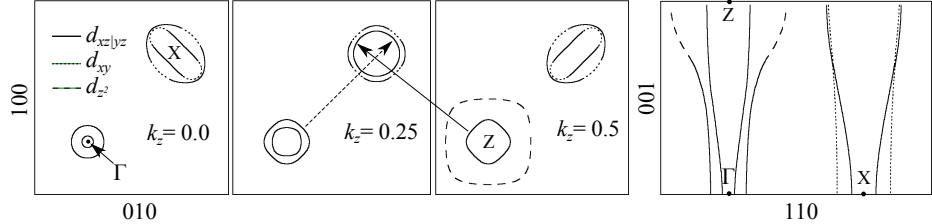


Figure 4.6.5: Cross sections of the corrected Fermi surface in the ab plane (panels 1, 2 and 3) and in the $[110]$ plane (panel 4). Markings correspond to the orbital character of the Fermi surface slices. Two nesting vectors are shown as long arrows.

These enhancements at $q = (\pi, \pi)$ show that partial nesting does indeed occur in this material demonstrating that this condition alone is not sufficient for superconductivity to occur. This concludes the Fermiology results, we now move onto the mass enhancements.

4.7 Determining the spin effective mass

Following the method in section 3.1.3, only a couple of portions of the data are suitable for analysis in that they feature more than one identifiable zeros in the oscillations due to the spin term which are suitably strong and well separated from other data. These are a maximal area of the α curve in the $[100]$ direction and a maximal area of the β curve in the $[110]$ direction.

We begin by looking at the β data by using the cylindrical approximation and then move onto using an expression for m_b^* derived from a polynomial fit to band masses calculated from DFT. Figure 4.7.1 shows the two fit forms for the band mass used — an eight order polynomial and the cylindrical approximation — used as well as in the inset the particular portion of the α band data that was used in the following investigation. As we can see from the inset, we use a relatively small portion of the measured data curve. Detailed in the panels to the right of the figure are the parameters for the two equation forms for the band mass. Beginning with the cylindrical approximation, figure 4.7.2 shows the FFT amplitudes for the said portion of the α electron pocket over a range of angles towards the $[100]$ direction as open circles. The shaded areas delimit where we believe the amplitudes go to zero as determined by inspecting the overall shape of the curve and

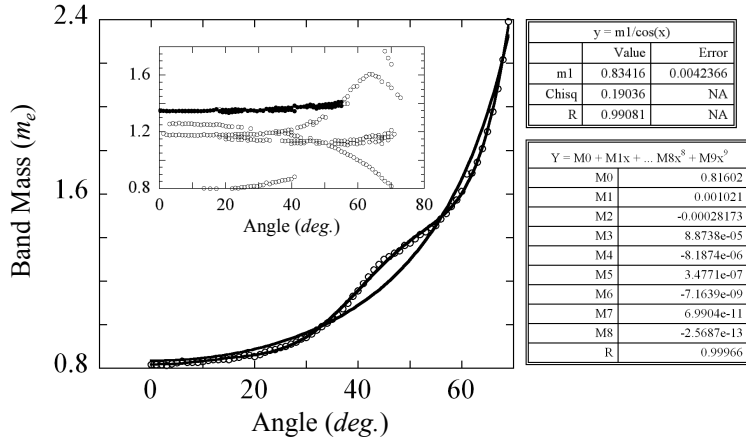


Figure 4.7.1: Band masses calculated from DFT of band 4 taken over a range of angles rotating towards the [100] direction. A fit to an order 8 polynomial is shown as well as a comparative fit using the cylindrical approximation.

the splitting of the peaks. The upper panel shows the $n = 5$ oscillation, with dotted lines showing the bounds using the cylindrical approximation for the band mass. The $n = 5$ oscillation most closely matches the zeros in the data with the $n = 6$ oscillation which fits reasonably well presented in the middle panel. The lower panel shows the next ($n = 7$) and previous oscillations ($n = 4$) in order to demonstrate that the A_S curves no longer align well with the data. We note that for negative angles (i.e. where the sample was rotated back beyond $B \parallel [001]$) the amplitude is not symmetric as expected. This has been observed previously for measurement using a similar technique [59] and the cause has not yet been fully determined. Some possible explanations could be changes in the resistance response of the cantilever as it transitions from flexing upwards to flexing downwards however further investigation will be required to determine this. Taking $g = 2$, the spin masses obtained using the cylindrical approximation from the presented curves are $5.01 \pm 0.05 m_b^*$ for $n = 5$ and $6.07 \pm 0.06 m_b^*$ for $n = 6$. We now contrast this with a spin mass determination using a band mass calculated from DFT. Figure 4.7.3 shows the revised curves with the upper panel showing $n = 4$ to be the best fitting with the lower panel demonstrating $n = 3, 5$ do not fit well to the measured data. Now the fit values gives a spin mass of $4.02 \pm 0.06 m_b^*$. The second suitable portion of data analysed is that of the maximal extrema of β where the field is rotated

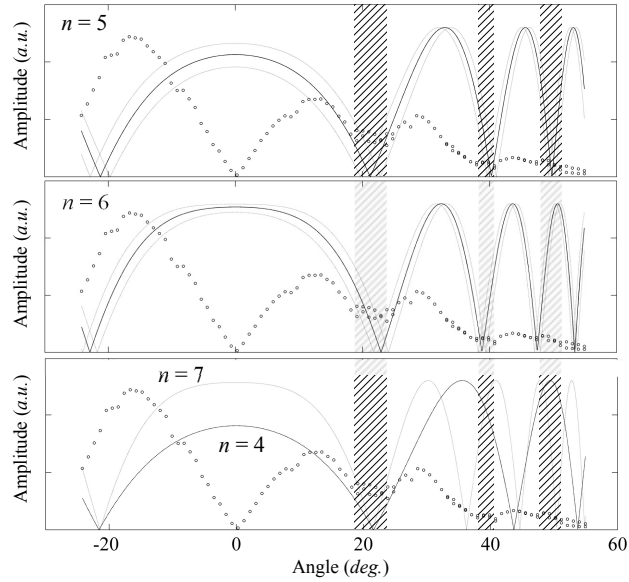


Figure 4.7.2: A_S curves calculated for various oscillations using the cylindrical approximation. Open circles are FFT amplitudes for α band rotating towards the [100] direction.

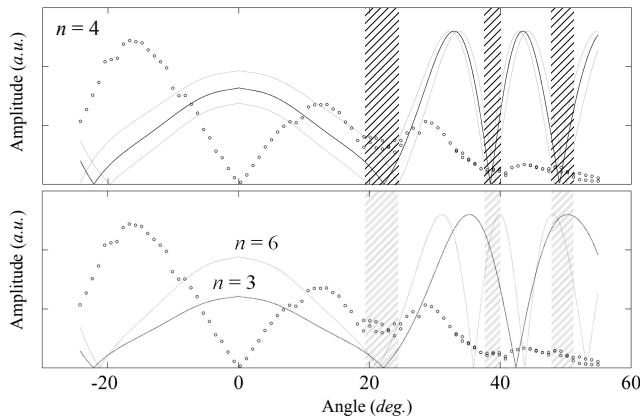


Figure 4.7.3: A_S curves calculated for various oscillations using the polynomial fit to DFT calculated band masses. Open circles are FFT amplitudes for α band rotating towards the [100] direction.

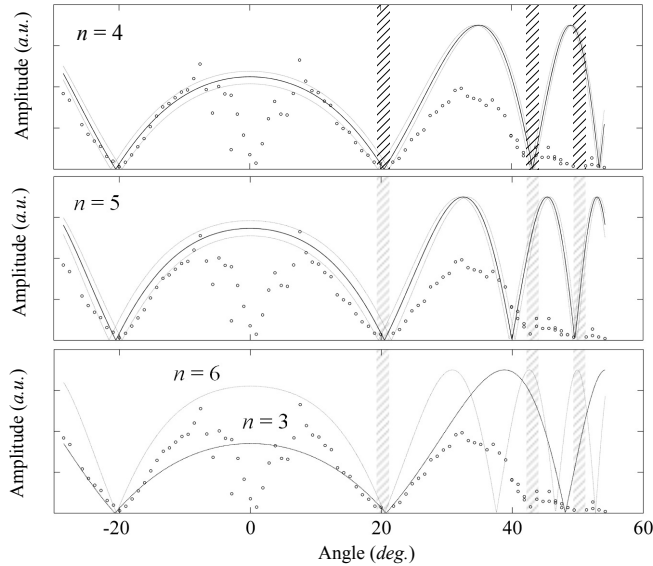


Figure 4.7.4: A_S curves calculated for various oscillations using the cylindrical approximation. Open circles are FFT amplitudes for β band rotating towards the [110] direction.

towards the [110] direction. The DFT does not follow exactly the shape of the measured data and leads to a discontinuous jump in the band mass if we strictly follow the maximal orbits — for this reason we elect to only use the cylindrical approximation since the portion shown appear relatively two-dimensional. Figure ?? shows the reasonable fits for $n = 4$ and $n = 5$ with the lowest panel showing the oscillations $n = 3$ and $n = 6$ are clearly not aligned with the measured data. The oscillations $n = 4$ and $n = 5$ correspond to spin masses of $3.46 \pm 0.02 m_b^*$ and $4.44 \pm 0.03 m_b^*$ respectively.

4.8 Determining the thermal effective mass

Basic LK formula fitting

A series of field sweeps were taken with H at 12° , 28° and 46° from [001] in the [110] direction. These were performed at a variety of temperatures from base (≈ 0.3 K) to above 2 K. Corrections were applied as detailed in section 3.1.2. Figure 4.8.1 shows the Fourier amplitude of various peaks as a function of temperature along with fits to equation 2.2.13. The field range for the FFT was necessarily large enough that individual peaks did not

overlap and also could be observed across a reasonable range of temperatures but also small enough so that the B dependent Dingle factor did not play too large a role and so an average B field can be assumed. The results from these fits are shown in table 4.7 along with the fit ranges. All FFTs in the plot were taken over an interval of 12-18 T with the exception of the γ_2 fit which was taken between 16-18 T so as to attain an appreciable peak. The standard deviation as calculated by randomly varying the temperature values by the estimated error (0.06 T) 1000 times and then taking the standard deviation of the fitted m^* values. Table 4.7 also shows gives a result, marked with a dagger, taken with a different field range. These fits give quite different values for the effective mass, indicating that the average field approximation is not a valid one.

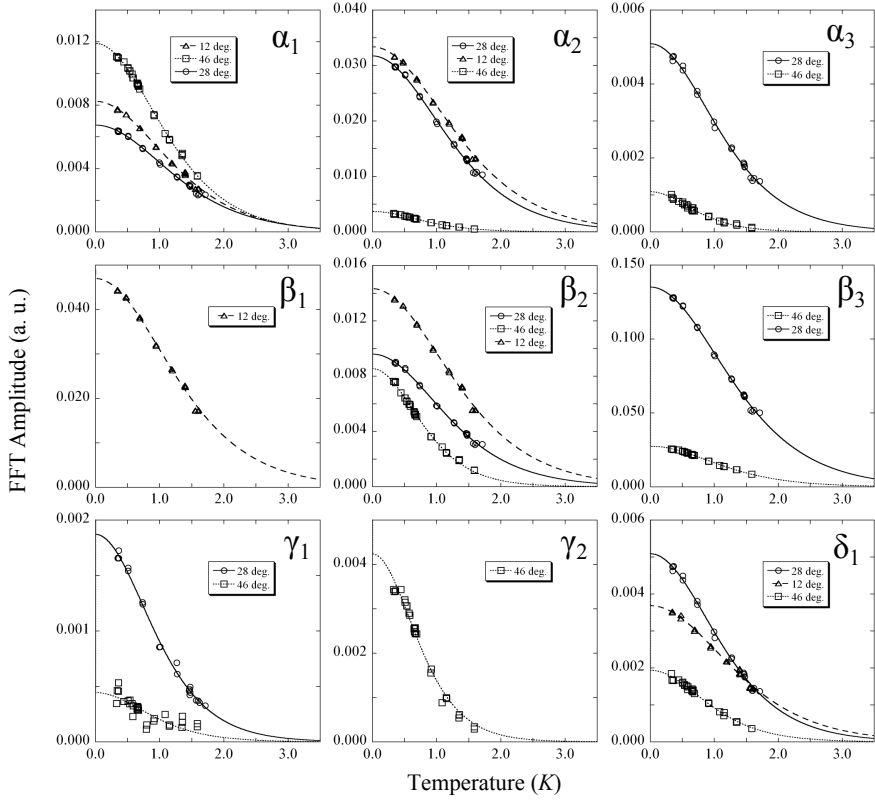


Figure 4.8.1: Fits to the temperature dependant part of the LK formula.

a dagger, taken with a different field range. These fits give quite different values for the effective mass, indicating that the average field approximation is not a valid one.

Retrofitting ansatz LK formulae

The measurements presented in the previous section were further refined using the ansatz LK formulae as described in section 3.1.4. Figure 4.8.2 shows some sample fits used to extract the Dingle terms used in the ansatz fit functions. Table 4.7 lists the extracted Dingle terms for each peak of the

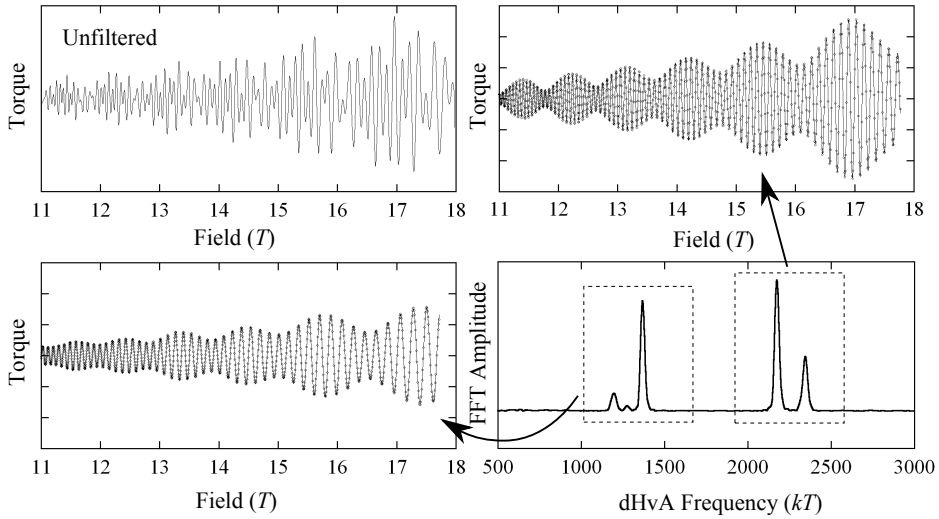


Figure 4.8.2: Top left panel shows torque data for data taken at 12° towards the [110] direction at 0.35 T with a polynomial background subtracted. Bottom right shows the FFT and the two filter windows to produce the filtered torque plots in the top right and bottom left. Filtered plots are fitted to extract the Dingle term for each frequency.

Fermi surface and the subsequent results of the retrofitted calculations for the effective masses. The various field limits were chosen in order to either obtain a clearly delimited peak in the lower field cases or to obtain a signal from a weak peak in the higher field cases.

‘Microfitting’ the LK formula

A second attempt at refining the LK fits was performed by applying the microfit technique described in section 3.1.4. 1.5 oscillations were fit at a time. Filtering the data beforehand is not always straightforward due to close proximity of neighbouring peaks. The stronger peaks from the α and β Fermi surfaces show banding of the masses and a clear trending of the results to one of a few values which have been highlighted in yellow. Data

in these regions were averaged to give the values in table 4.7.

All filtered using function $F_{\text{filt}}(x) = F(x) \times 1/2[\tanh(\pi(x - x_{\text{low}})/w) + \tanh(-\pi(x - x_{\text{high}})/w)]$ where F is the Fourier transform of the torque data, x is the dHvA frequency, x_{low} and x_{high} are the lower and upper limits of the filter range respectively and w determines the trail off slope of the filter function. For all measurements $w = 10$.

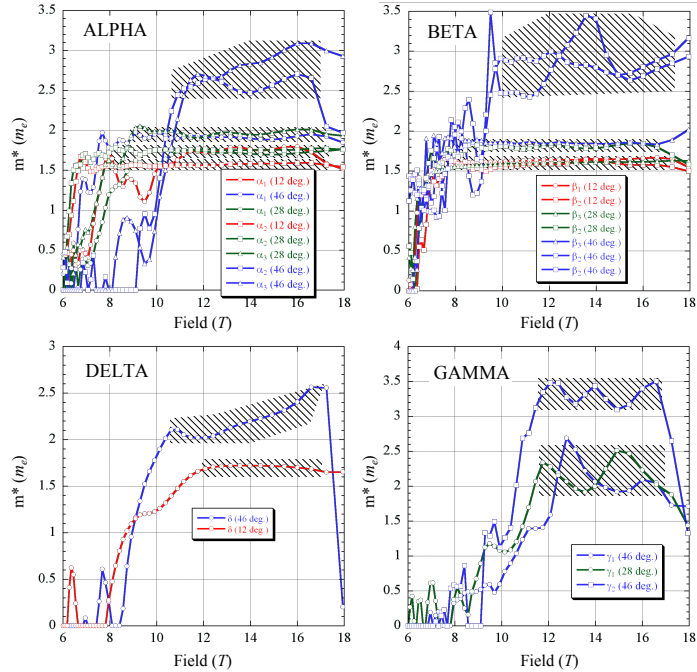


Figure 4.8.3: Effective temperature dependant masses extracted from fits to between one and three dHvA oscillations in the measured data. See Appendix A for a full list of parameters for each set of fits.

4.9 Conclusions

The BaFe₂P₂ crystal and the subsequent angle dependent dHvA measurements are of very good quality as evidenced by a number of traits including the presence of second and third harmonics in the FFTs, the hole orbits showing up over a wide angular range, the early onset of oscillations at 6 T and the observation of the Zeeman splitting of the FFT peaks. The crystal appears to be a very clean single crystal although there is some evidence of some misaligned domains, for example from some of the Bragg spots dou-

Table 4.7: Comparison of the three effective mass calculation techniques. First grey band shows the plain LK fitted results, following white band details the retrofitted effective mass calculations, following grey band details the microfitted results, and the final band details the band masses from DFT calculations and the three results normalised to these band masses. Result marked with a dagger is repeated with a different field range. Entries marked ‘NA’ had a signal too weak to extract an α value and so microfitting was not possible.

Angle	Freq.	Label	m_{LK}^*	$m_{\text{ret.}}^*$	α	$B_{\text{min.}}$	$m_{\text{mic.}}^*$	$B_{\text{max.}}$	$B_{\text{min.}}$	Filt.	Width	m_{b}^*	$\frac{m_{\text{LK}}^*}{m_{\text{b}}^*}$	$\frac{m_{\text{ret.}}^*}{m_{\text{b}}^*}$	$\frac{m_{\text{mic.}}^*}{m_{\text{b}}^*}$
12	1210	α_1	1.49(2) [†]	1.69	58.68	8	NA	NA	NA	NA	1.04	1.43	1.63	NA	NA
12	1210	α_1	1.71(3)	1.75	58.68	12	1.75(3)	17.0	11.0	1100-1240	1.04	1.64	1.68	1.68	1.68
28	1269	α_1	1.64(2)	1.68	59.60	12	1.72(2)	17.0	11.0	1200-1310	0.90	1.83	1.88	1.92	1.92
46	1532	α_1	1.86(3)	1.90	48.79	12	1.92(2)	17.0	9.0	1430-1585	1.00	1.86	1.90	1.92	1.92
12	1372	α_2	1.54(2)	1.58	45.99	12	1.57(1)	17.0	8.0	1320-1440	0.84	1.83	1.88	1.86	1.86
28	1530	α_2	1.69(2)	1.74	72.35	12	1.75(2)	17.0	8.0	1450-1650	0.93	1.81	1.87	1.88	1.88
46	2017	α_2	2.49(5)	2.56	61.06	12	2.55(11)	16.8	10.5	1970-2100	1.83	1.36	1.40	1.40	1.40
28	1365	α_3	1.85(3)	1.93	115.49	12	1.97(3)	17.0	9.5	1320-1440	1.18	1.56	1.63	1.67	1.67
46	1930	α_3	2.87(7)	3.04	149.39	12	2.75(24)	17.0	10.7	1890-1970	1.00	2.87	3.04	2.75	2.75
12	2180	β_1	1.61(2)	1.65	51.12	12	1.63(2)	17.0	8.0	2100-2270	0.98	1.64	1.68	1.66	1.66
12	2350	β_2	1.56(3)	1.62	102.36	12	1.57(3)	17.0	9.0	2270-2450	0.86	1.81	1.88	1.82	1.82
28	2605	β_2	1.30(2)	1.87	102.36	6	1.81(2)	17.0	8.5	2555-2670	1.03	1.68	1.71	1.76	1.76
46	3347	β_2	1.73(2)	1.76	34.08	12	2.86(8)	17.3	10.0	3250-3370	1.80	1.44	1.50	1.59	1.59
46	3381	β_2	2.59(6)	2.69	94.57	12	2.78(32)	17.3	10.0	3365-2500	1.80	0.88	0.90	1.55	1.55
28	2475	β_3	1.58(2)	1.61	48.81	12	1.59(2)	17.0	8.0	2400-2560	0.93	1.95	2.00	1.71	1.71
46	2970	β_3	1.82(3)	1.86	40.03	12	1.86(1)	17.0	8.5	2850-3100	1.03	2.07	2.15	1.80	1.80
28	912	γ_1	2.13(5)	2.22	104.38	12	2.17(18)	16.8	11.3	850-970	-1.49	-1.03	-1.10	-1.46	-1.46
46	1320	γ_1	2.19(3)	2.30	129.82	12	2.00(37)	16.8	11.3	1270-1370	-2.04	-0.91	-0.95	-0.98	-0.98
46	4497	γ_2	3.31(8)	3.32	91.06	16	3.31(13)	16.8	12.2	4400-4600	-1.89	-1.17	-1.23	-1.75	-1.75
12	1270	δ	1.54(2)	1.64	173.00	12	1.71(1)	17.0	12.0	1250-1310	-0.91	-2.41	-2.53	-1.88	-1.88
28	1370	δ	1.85(3)	1.93	115.49	12	NA	NA	NA	NA	-0.98	-1.89	-1.97	NA	NA
46	1626	δ	2.22(4)	2.33	126.02	12	2.17(15)	17.0	10.5	1590-1690	-1.10	-3.00	-3.01	-1.96	-1.96

bling up in the XRD and multiple peaks observed in the FFT at particular angles – see for example α towards the [100] direction above $\sim 20^\circ$ in figure 4.3.5. There are approximately half a dozen separate peaks observed at this location which implies a similar amount of misaligned domain orientations. This misalignment however does not appear to affect the overall data which largely does not resolve the extra domains.

The Fermiology is largely solved by the angle plots with only a few minor ambiguities. The $F \cos \theta$ angle dependent plots clearly show approximately level curves for the two hole Fermi surfaces demonstrating that α and β are approximately two-dimensional. The hole surface, γ , deviates at high angles and δ is strongly three dimensional. Although we cannot say for certain whether γ is pinched off or not, based on the rigidly shifted DFT we expect that the minima to be small but not zero and was not observed due to low frequency noise in the oscillations.

Previous dHvA measurements on BaFe₂(As_{0.37}P_{0.63})₂ by Analytis *et al.* shown in figure 4.3.6 identified the branch of the dHvA angle data at around 500 T as the neck of the 2D hole pocket. In our own analysis, it made much more sense to attribute this curve to the neck portion of the 3D hole band, with the neck of the 2D pocket being buried in the low frequency noise. These two different statements are not necessarily incompatible. Since the DFT data for the entire series suggests that whilst the 2D hole pocket retains the same shape along the BaFe₂(P_xAs_{1-x})₂ series, the 3D hole pocket narrows considerably at the Γ point and switches from being concentric with the 2D pocket at $x = 1$ to crossing through the 2D pocket as x is reduced. However when the spin-orbit interaction is considered in the DFT calculations, the crossing of the surfaces causes the bands to be redefined such that the bands do not actually cross, in which case there would not be a Yamaji point as specified in the Analytis paper since the similarly sized orbits at 50° angle are not from the same band. An attempt was made to see if there was an enhancement of the oscillation amplitude at the corresponding putative Yamaji point in the BaFe₂P₂ data but the close proximity of the strong oscillations from the electron pockets made this intractable with this particular data set.

Although the Fermi surface appears to nest at the $q = (\pi, \pi, \pi/4)$ as shown in figure 4.6.5, the corresponding imaginary part of the susceptibility data shows stronger enhancements at the $q = (\pi, \pi, \pi/2)$ vector, primarily

due to the nesting between the 3D hole Fermi surface and the inner electron surface. However the susceptibility calculations do not take into account the orbital character of electrons at these nesting vectors. The dominant character at $q = (\pi, \pi, \pi/2)$ is between regions of $d_{xz} + d_{yz}$ on the narrow portion of the 3D surface and regions that switch between d_{xy} and $d_{xz} + d_{yz}$ on the electron surface. This will suppress the scattering between the two due to considerations of angular momentum. Nonetheless the susceptibility shows there are significant enhancements of the imaginary part of the susceptibility response between the electron and hole surfaces and the partial nesting conditions required for spin fluctuations are satisfied. Given that the system becomes more two dimensional as we approach the superconducting region, this suggests that the nesting is enhanced and the fluctuations become stronger.

Like previous measurements of band structure by dHvA in the $\text{BaFe}_2(\text{P}_x\text{As}_{1-x})_2$ materials, the Fermi surfaces are smaller than predicted by DFT calculations [49, 51]. Ortenzi *et al.* [85] posits an explanation based on interband scattering which leads to shrinking of the electron and hole pockets and an enhancement of the effective mass based on relaxing an assumption on the chemical potential being far* from the electron/hole band edges. Similar moderate effective mass enhancements to what we found in BaFe_2P_2 of around $1.4m_e$ were calculated — albeit modelled on a more two dimensional pnictide, LaFePO — along with the fact that the theory predicts stronger shifts where interband coupling occurs is supported by the BaFe_2P_2 data. The nested portions of the 3D δ hole band, for example, is strongly shifted where it nests with the electron band but the bulge which does not nest with anything is not shifted at all. Similar shifts between the measured data and calculations were observed for the sister 122 compound SrFe_2P_2 [52] which is also a partially nested material and yet shifts are notably absent for the non-nested 122 pnictide compound CaFe_2P_2 [81] which matched the DFT calculations with no adjustments to the energies.

It is not clear at this stage whether the shifting of the Fermi surface proportional to the electron character for the 3D hole δ band performed in section 4.3.1 represents anything physical or is simply a convenient and reproducible way to obtain the correct band topology. Settling this question will require further investigation. However it is interesting to note that the

*i.e. greater than the scattering boson energy scale

energy shifts for the 3D hole surface are proportional to the d_{z^2} and $d_{xz}+d_{yz}$ characters, suggesting there may be a link between the k_z scattering component and energy enhancements. Recalling that the 3D hole surface is where we expect to see the strongest nesting component this also suggest that the scattering between layers may play a part in suppressing superconductivity.

The wide bulge in the 3D hole surface ensures that several terms are needed for the harmonic fits represented in section 4.5. For this reason, the harmonic fits simply represent a convenient way to obtain the Fermi surface topology in the case of the 3D hole pocket.

Chapter 5

Hall measurements on BSCO_{2201}

Low temperature Hall measurements are presented on BSCO_{2201} over a wide doping range spanning the slightly underdoped to the far overdoped. A novel doping assignment scheme based on new Tl_{2201} data is trialled and was found to give reasonable dopings for BSCO_{2201} . The Hall data at low temperature shows possible linear behaviour at low temperature and interesting evolution of the low T Hall parameters which place constraints on an expected low temperature anisotropic term in either the scattering or the carrier density.

5.1 Sample growth

The samples were grown and initially characterised by Prof. Takeuchi's group in Sendai University, Japan in May 2009 using the floating zone technique. Here powders of the correct stoichiometry are compacted into a rod and fed slowly through a furnace where it becomes a viscous melt. The melt solidifies epitaxially on a seed crystal with impurities held in the melt portion of the crystal which gradually moves up, along the rod until it reaches the end of the rod and the growth is over. The end portion, containing the impurities is then removed. Similar samples have already been extensively studied through ARPES and STM by members of the Sendai group [13, 86].

Table 5.1 lists the nominal stoichiometries for the sample growth as well as the annealing conditions. Also listed are the *nominal* T_c values for the source crystals which are used in the naming, the actual measured T_c values of individual samples for the purposes of doping determination are slightly different due to different definitions of T_c^* .

The samples are named according the convention,

B< T_c >K<Region><Crystal No.><Sample No.>

*The source crystals were defined based on the zero value T_c , the T_c for doping purposes is defined as the mid-point of the transition with an error based on the difference between the mid-point and the zero-point.

Table 5.1: Growth details for the BSCO₂₂₀₁ samples. OD, OP and UD stand for over, optimally and under doped respectively. T_c values are nominal.

Nominal composition								Annealing conditions
Bi	Pb	Sr	La	Cu	O	T_c	Reg.	
1.72	0.38	1.85	0.0	1.0	6+d	<2	OD	400 °C, 96 h in 2.5 atm. O ₂
1.72	0.38	1.85	0.0	1.0	6+d	7	OD	750 °C, 24 h in air
1.72	0.38	1.85	0.0	1.0	6+d	16	OD	550 °C, 72 h in flowing N ₂
1.35	0.85	1.47	0.38	1.0	6+d	30	OD	As grown
1.35	0.85	1.47	0.38	1.0	6+d	32	OP	650 °C, 72 h in flowing N ₂
1.2	0.90	1.30	0.55	1.0	6+d	30	UD	As grown
1.2	0.90	1.30	0.55	1.0	6+d	28	UD	650 °C, 72 h in flowing N ₂

so for example ‘B00KOD2A’ refers to the sample ‘A’ taken from the crystal ‘B00KOD2’ — the second overdoped crystal with a T_c of 0 K.

5.2 Size determination

Thicknesses were determined for some of the samples using the FIB or the optical microscope as described in the methods section. The thicknesses used to calculate absolute values of R_H are listed in table 5.2 and are marked in grey. FIB results are given for areas as close to the two voltage contacts that were visible in the scans. As can be seen in the example scan shown in figure 5.2.1, there is some variation in the depth along the sample length. Measurements are therefore taken as close to the voltage legs as possible and where appropriate suitable errors are estimated.

The two scans shown are of good quality, however for the purpose of estimating errors in the thickness some of the scans presented problems. Samples B26KOD1A, B28KUD3A, B30KOD2 and B30KUD3 were obscured with the grease applied as part of the pulsed field measurements. Other samples were not correctly earthed such as B28KUD3B which made the images dark, whilst samples B07KOD2 and B32KOP3 were very flaky under close scrutiny. A scan of B30KOD3 showed that it was partially split in the ab plane which may contribute to systematic error in thickness estimate. In all these cases, the estimate in the thickness error was adjusted accordingly to compensate. A more comprehensive set of FIB scans, including images of the split in the layers can be found in Appendix C.

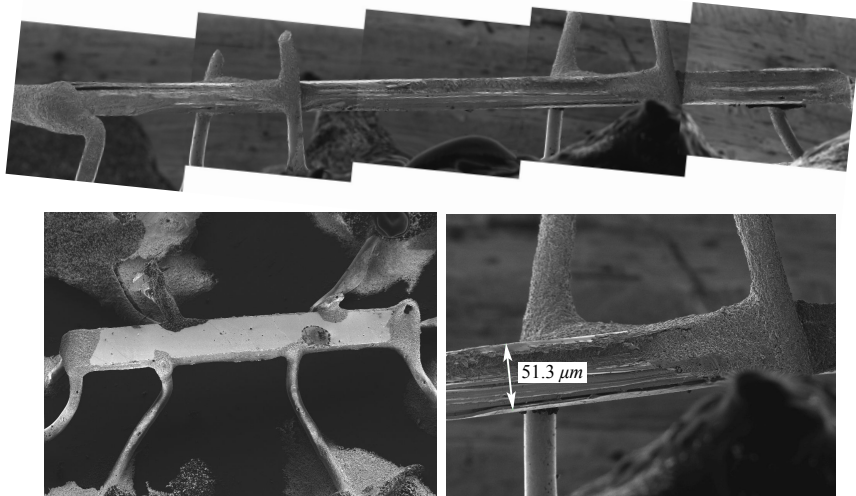


Figure 5.2.1: Top shows an image composited from several FIB scans along the length of sample B00KOD1A, with bottom right showing a detail of the right voltage leg. Bottom left shows an oblique top down view of sample B30KOD3.

The oblique view of B30KOD3 in figure 5.2.1 shows a clear misalignment of the voltage legs to the right of the image. This illustrates why it is necessary to take both positive and negative field sweeps in order to separate the magnetoresistance from the Hall components. This also explains why the length and width determinations were subject to large errors which affects the absolute value of the in-plane resistivity calculations.

5.3 Doping determination

Figure 5.3.1 shows measurements of the in-plane resistivity, $\rho(T)$, of the samples in zero field taken in the VTI in the Polo magnet. The mid-transition T_c values were extracted from the plots with the error determined from the difference between the mid point and the zero resistance point. Results are listed in table 5.3 as well as the normalised T_c values, $T_c/T_c(\text{max})$, with $T_c(\text{max}) = 36 \text{ K}$. The derivatives of the same resistivity curves in figure 5.3.1 are plotted in figure 5.3.2 along with derivatives to temperature sweeps taken at 13 T. Here we can see in the overdoped samples the distinct slope downwards towards T_c which signifies the coherent quasiparticle

Table 5.2: Sample measurements as determined by optical microscope measurements and thickness as determined by FIB. Samples highlighted in grey were used for determining absolute values of R_H . A and B refer to each of the two contacts visible to the FIB scan. Measurements are in micrometres.

Sample	Length	Width	Thick.	FIB	
				Contact A	Contact B
B00KOD1A	781 ± 123	157 ± 49	N/A	45 ± 1	50 ± 5
B00KOD1B	627 ± 49	196 ± 44	39 ± 5	43 ± 1.5	45 ± 1.5
B07KOD1	1277 ± 74	392 ± 49	29 ± 10	N/A	N/A
B07KOD2	1061 ± 69	333 ± 74	N/A	20 ± 5	30 ± 1
B16KOD1A	795 ± 34	299 ± 34	N/A	24 ± 1	24 ± 1
B16KOD2A	358 ± 29	172 ± 54	9 ± 1	N/A	N/A
B16KOD3	1122 ± 44	368 ± 83	N/A	25 ± 2	24 ± 2
B30KOD1	436 ± 34	250 ± 44	21 ± 2	N/A	N/A
B30KOD2	344 ± 44	137 ± 29	20 ± 5	15 ± 4	15 ± 4
B30KOD3	255 ± 49	98 ± 25	N/A	16.5 ± 1.5	19 ± 1
B32KOP1	658 ± 83	397 ± 34	N/A	6.5 ± 1.5	6.5 ± 1.5
B32KOP2	441 ± 25	226 ± 20	10 ± 1	N/A	N/A
B32KOP3	437 ± 34	118 ± 20	N/A	6 ± 1	6 ± 1
B32KOP4	427 ± 74	137 ± 39	N/A	9 ± 3	9 ± 3
B30KUD1A	622 ± 49	447 ± 25	36 ± 3	N/A	N/A
B30KUD1B	828 ± 34	471 ± 64	35 ± 3	N/A	N/A
B30KUD2	545 ± 69	152 ± 39	N/A	5 ± 1	5 ± 1
B30KUD3	476 ± 49	118 ± 34	N/A	7 ± 2	7 ± 2
B28KUD2A	657 ± 29	250 ± 39	11 ± 1	N/A	N/A
B28KUD3A	633 ± 49	142 ± 34	N/A	16 ± 3	16 ± 3
B28KUD3B	653 ± 44	216 ± 49	N/A	16 ± 3	16 ± 3

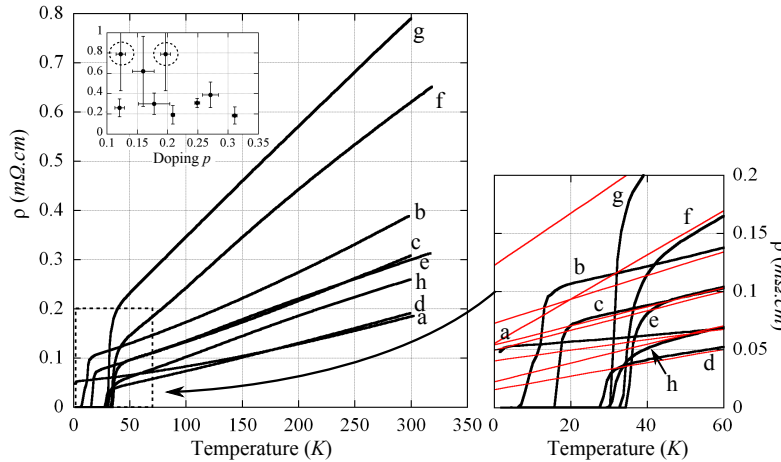


Figure 5.3.1: The in-plane resistivity measured in zero field. From nominally overdoped to underdoped, samples are (a) B00KOD1A, (b) B07KOD2, (c) B16KOD1A, (d) B30KOD3, (e) B32KOP1, (f) B32KOP4, (g) B30KUD3, (h) B28KUD3A. Right panel shows a zoomed portion of the curves at the transition temperatures along with continuations of fits to portion of the curve above T_c in red. Inset shows $\rho(300\text{ K})$ vs. doping with errors due to size determination.

region which begins at T_{coh} . This gradually levels out as doping is reduced until we observe a kink which marks the pseudogap temperature, T^* . The T^* kink is weaker in B30KUD3 than the optimally doped samples and in fact only appears, at a much lower temperature, when the field is applied. This suggests that it is in fact more doped than the optimally doped samples rather than less doped as the nominal composition would suggest. If we consider B30KUD3 to be overdoped rather than underdoped then this trend continues right across the range of samples.

Figure 5.3.3 shows the dopings as determined by the three different methods outlined in the experimental methods chapter. The dopings of the crystals range for $p = 0.12$ to $p = 0.31$ hole per Cu atom with significant discrepancies between the methods. The Ando determination bunches the doping values around a much narrower range, whereas the dopings determined by comparing with the Tl_{2201} dHvA data, spread the overdoped values over a wider range. The Tallon method sits between the two.

Figure 5.3.4 present Hall data at 300 K again taken in the Polo with comparable data from Konstantinović *et al.* [92]. It is clear that the Ando assignment of dopings is too confined with the data not at all following the

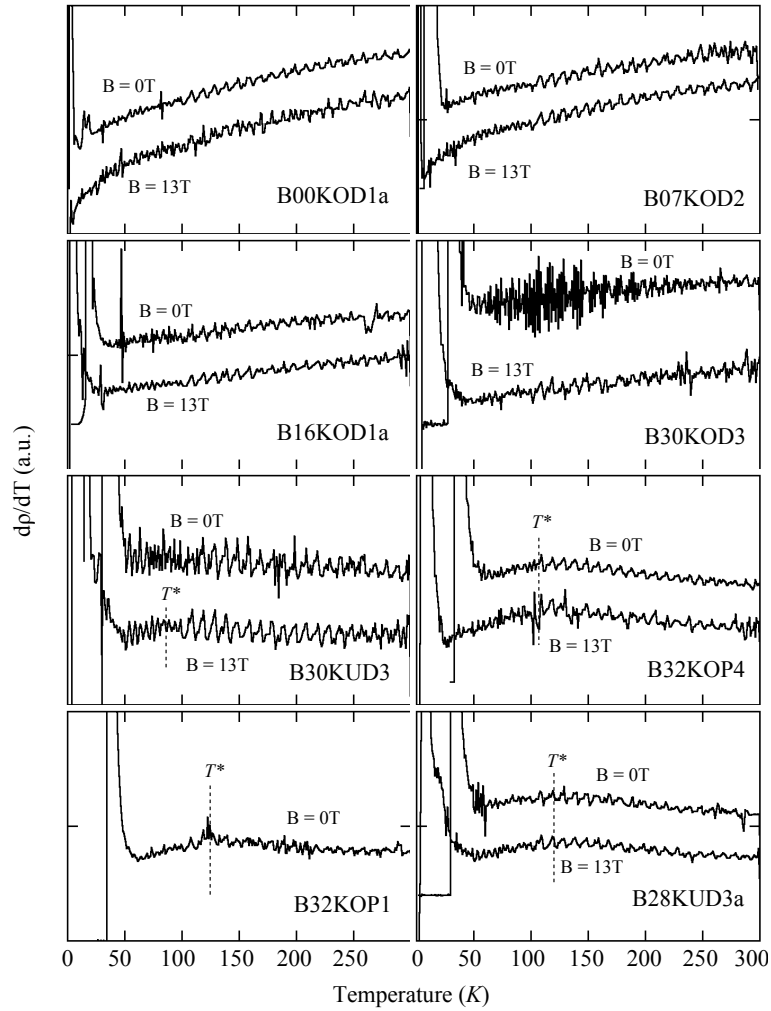


Figure 5.3.2: $d\rho(T)/dT$ curves for each of the samples taken in 0 T and 13 T field. Note the evolution of the T_{coh} gradient in the overdoped samples which give way to the T^* kink in the underdoped samples, B30KUD3 has been repositioned to follow this trend.

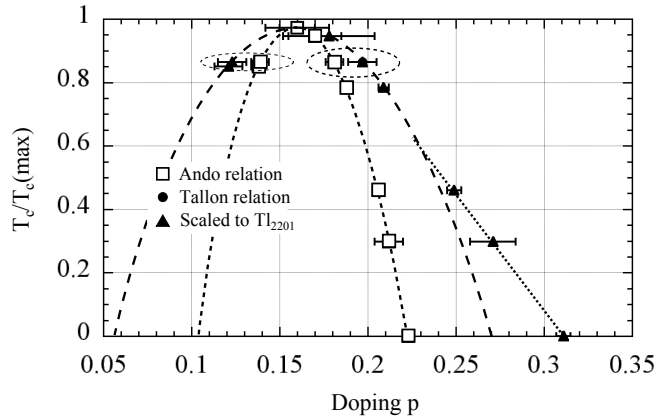


Figure 5.3.3: Doping distributions for the three different methods. From left to right, B28KUD3A, B30KUD3 (Assume UD), B32KOP1, B32KOP4, B30KUD3 (Assume OD), B30KOD3, B16KOD1A, B07KOD2, B00KOD1A. Broken lines are a guide to the eye. Circled points are B30KUD3 for both the overdoped and underdoped scenarios.

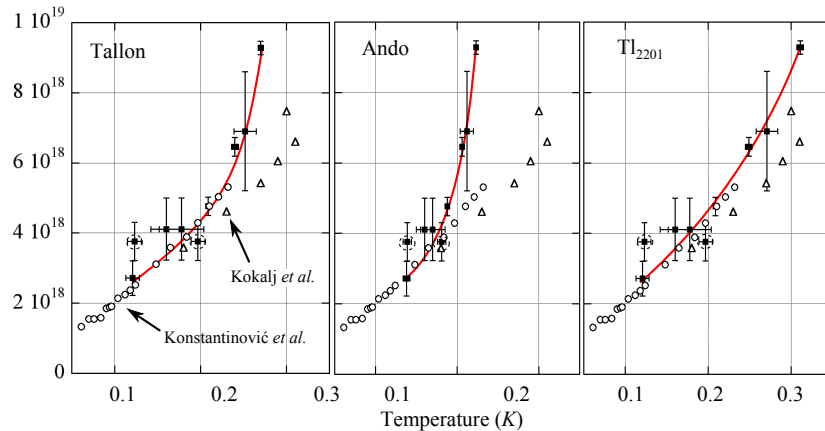


Figure 5.3.4: Hall data at 300 K compared with similar data taken from refs. [Kokalj2012, 92] using different doping assignments. From left: Tallon relation, Ando relation and scaling to Tl_{2201} data. Red lines are guides to the eye, circled points are B30KUD3 in the overdoped and underdoped positions.

respective curves whereas the Tallon relation follows much close the shape of the curve, although, perhaps this is not surprising given that the dopings in the Konstantinovoć paper were also assigned using the Tallon relation. However what is most interesting is that when compared with Tl_{2201} data from Kokalj *et al.* [Kokalj2012] which we know is appropriate to scale to the Tl_{2201} doping scheme, we see that of the three methods, scaling the $BSCO_{2201}$ to the Tl_{2201} dHvA data matches the closest. On this rationale, we continue assuming that the Tl_{2201} doping assignments are the correct ones.

Also, referring to the circled points, we see that again the data is more consistent if we consider the B30KUD3 to be overdoped rather than underdoped. Looking back to the inset of figure 5.3.1 we see that there is large scatter in the data points due to uncertainty in the dimensions which were determined by optical microscope, however there is an approximate downward trend with doping which is similar to what is found in the literature [9, 10, 92, 93]. Although B30KUD3 is more consistent to this trend in the underdoped position, the trend still lies with the error bars of the overdoped position. Looking ahead to the inset of figure 5.5.4 which shows R_H values at 300 K vs. doping, which depend only on the measurement of depth — which was much more accurately determined by the FIB — we see that the underdoped position lies far outside the overall trend even when considering the error bars.

5.4 Temperature sweeps

Figure 5.3.1 shows the in-plane resistivity, $\rho(T)$ for each of the samples in zero field taken in the VTI in the Polo magnet. From this plot we can characterise the T_c of the samples and find the residual resistivity, ρ_0 by using simple linear fits to the data above the transition temperatures and extrapolate back to zero. Table 5.3 show the fit parameters for each of the samples. The residual resistivities are very good with only one being above 100 $\mu\Omega\text{cm}$ and most below 70 $\mu\Omega\text{cm}$ which has been cited as being exceptionally good for $BSCO_{2201}$ [9]. Moreover the T_c of the optimally doped sample is 36 K which is amongst the highest reported [9] which again is testament to the crystal quality. ρ_0 generally increases as you move away from critical doping which lends support to the notion of the La doping

Table 5.3: Fits parameters to $\rho = \rho_0 + \rho_1 T$ for zero field resistivity data above T_c as well as T_c values determined from the same plots. Fits at low T are shown in inset to figure 5.3.1.

Sample	$\rho_0(\mu\Omega\text{cm})$	$\rho_1(\mu\Omega\text{cm})$	$T_c(\text{K})$	$T_c/T_c(\text{max})$
B00KOD1A	40.7	0.454	0 ± 1.0	0.00 ± 0.03
B07KOD2	73.0	1.026	11 ± 3.8	0.31 ± 0.11
B16KOD1A	49.9	0.843	17 ± 1.0	0.47 ± 0.03
B30KOD3	15.9	0.578	29 ± 0.5	0.81 ± 0.01
B32KOP1	54.2	0.824	36 ± 1.0	1.00 ± 0.03
B32KOP4	55.6	1.904	35 ± 2.0	0.97 ± 0.06
B30KUD3	123.0	2.233	32 ± 1.0	0.89 ± 0.03
B28KUD3A	22.6	0.806	32 ± 1.0	0.89 ± 0.03

increasing the disorder in the CuO layers.

The inset to figure 5.3.1 shows the $\rho(300 \text{ K})$ values for the samples along with error bars due to uncertainty in the size determination. As we saw in the previous section, there is significant misalignment and overall width to the voltage contacts which lead to large systematic errors which affect scaling only. Nonetheless, there appears to be an downward trend in resistivity as doping is increased. The circled points are B30KUD3 in both the overdoped and underdoped position and although the position is perhaps more fitting in the underdoped position, there error bars leave the overdoped point well within the overall trend.

5.5 Hall plots

Figures 5.5.1, 5.5.2 and 5.5.3 show the Hall coefficients extracted as described in the methods section for samples progressing from overdoped, optimally doped to underdoped respectively. Where appropriate, the data is compared to that from Ando *et al.* [9]. Red lines in the plots are guides to the eye.

For the samples of $T_C \geq 28 \text{ K}$ there are some data which did not reach sufficient field to obtain linear behaviour which are circled with a dashed line in the plots. For sample B30KOD2, many of the sweeps for $T < 45^\circ\text{C}$ showed significant hysteresis due to temperature drift. Despite temperature correction, many of the fits did not pass through the origin (circled in the

figure) which is a good indicator that the true field suppressed linear Hall has not been obtained. The same goes for the circled points on the B30KUD2 plot and another data point at $T = 1.5$ K and $R_H = 7.3 \times 10^{-3} \text{ cm}^3$ from the first trip to LNCMI which is outside the plot boundary as well as data points on the plot for B28KUD3B. The data sets are combined, minus the points highlighted in the previous paragraph, in the main panels of figure 5.5.4 alongside the data from the Ando paper.

With reference to figure 5.5.4 and in particular the new low temperature data points, we see that doping strongly affects the qualitative shape of the R_H curves. Whilst the trend appears to be that $R_H(300 \text{ K})$ decreases as doping increases as to be expected, the $R_H(0 \text{ K})$ values all tend toward approximately similar values of around $0.5 \times 10^{-3} \text{ cm}^3$ to $1.5 \times 10^{-3} \text{ cm}^3$. The most pronounced difference between high and low temperature values though is with the optimally doped samples which are around $\times 2.75$ greater at high temperature. Right down to 0 K there is no sign change in R_H , which suggests that the hole pockets have higher mobility than the electron pockets across the range of dopings studied.

The error bars on the data points do not include error from the thicknesses which are systematic across the data points. The inset of figure 5.5.4 shows the R_H values at 300 K vs. doping for each of the samples with these error bars applied. The overall trend is downward with doping with the progression being approximately monotonic, however the exception is B16KOD1A which has a slightly lower R_H than would be expected from a linear trend.

The Hall angle is plotted for each of the samples where $B = 0 \text{ T}$ in-plane resistivity data is available in figure 5.5.5 with temperature raised to a fitted exponent, α . In the original Chien analysis, $\alpha = 2$ but is allowed to vary here to observe deviations from the expected T^2 behaviour. Similar analysis was performed for resistivity data taken at $B = 13 \text{ K}$ and although these plots are not shown, the fitted α values are plotted in the bottom left subplot along with the $B = 0 \text{ T}$ values. A nominal unitary field was used when calculating $\cot \theta_H$ and only data above the superconducting transition was fitted and is shown in the plots. Note that for the $B = 13 \text{ T}$ case, the Hall data for the optimally doped sample B32KOP1 was compared with resistivity data for sample B32KOP4 which explains the slightly different doping value assigned to it. In this particular instance, it appears that the

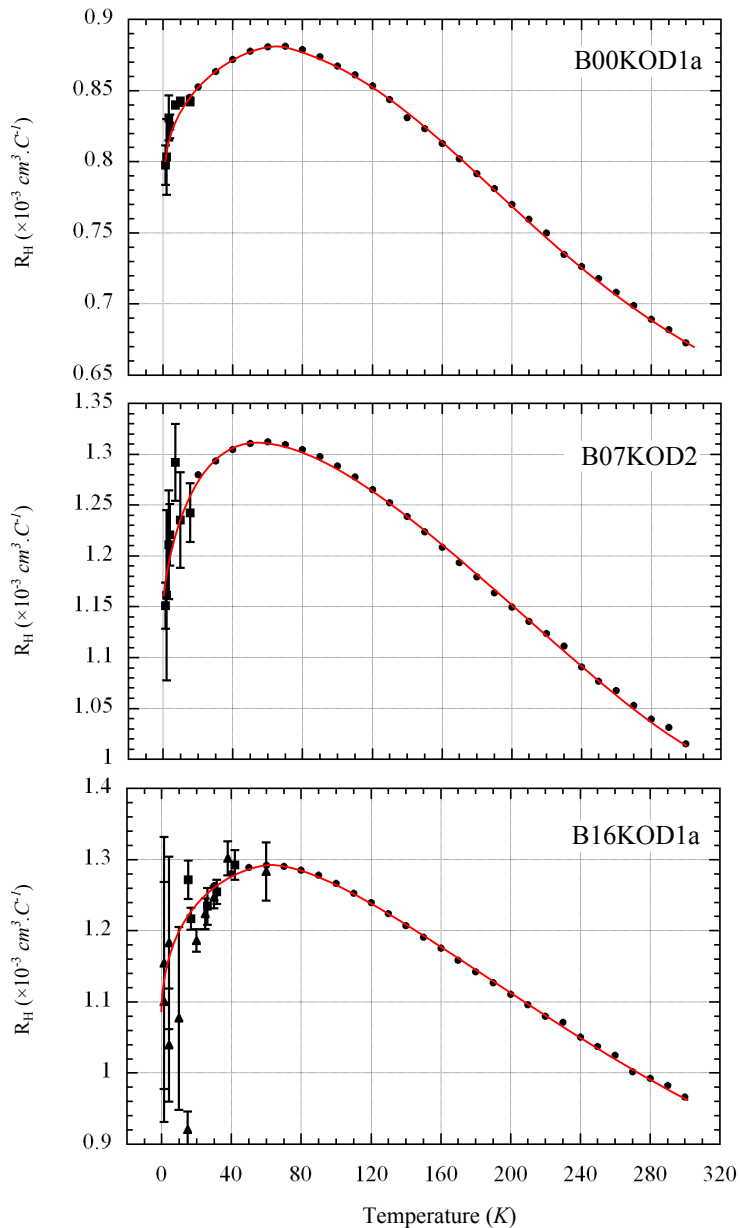


Figure 5.5.1: R_H for underdoped samples of BSCO_{2201} . Plots show results from, • Polo in June 2010, ▲ LNCMI in June 2009, ▼ LNCMI in Feb 2010, ■ Nijmegen in May 2010. Symbols for comparable samples are marked on the plots. Red lines are a guide to the eye.

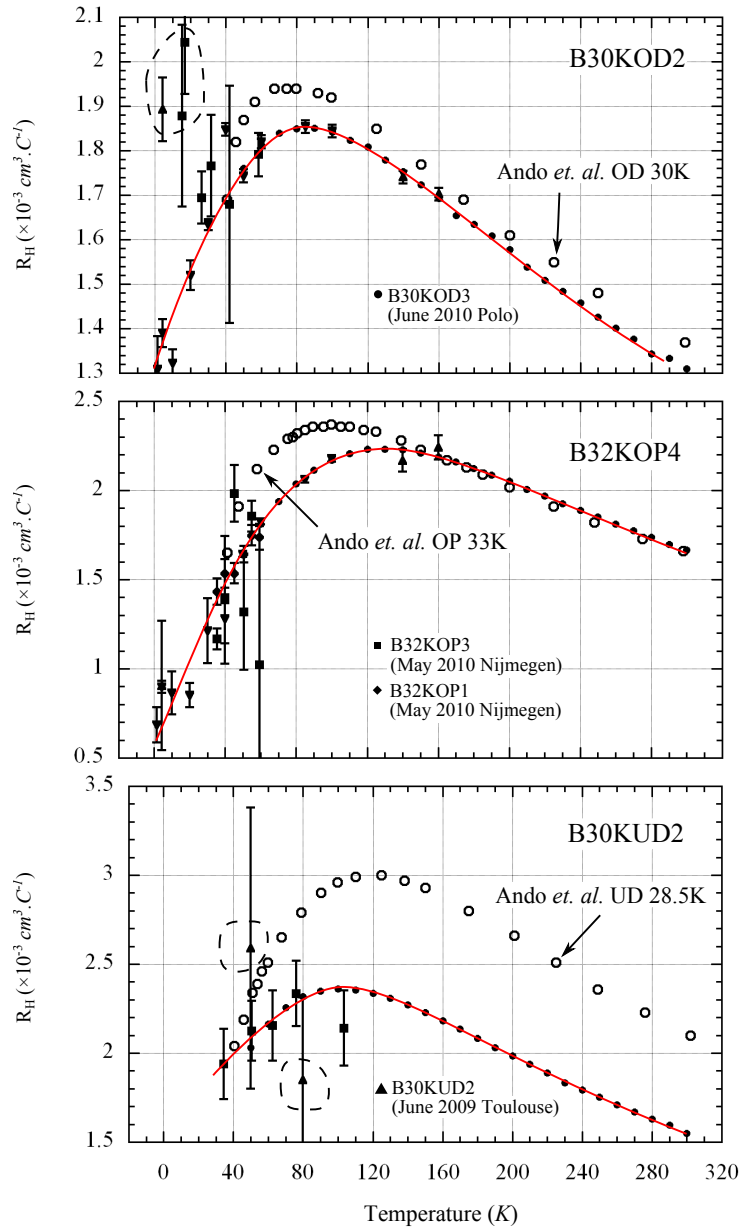


Figure 5.5.2: R_H for underdoped samples of $BSCO_{2201}$. Plots show results from, • Polo in June 2010, ▲ LNCMI in June 2009, ▼ LNCMI in Feb 2010, ■ Nijmegen in May 2010. Symbols for comparable samples are marked on the plots. Dashed lines indicate points where the field was not sufficient to achieve linear behaviour. Red lines are a guide to the eye.

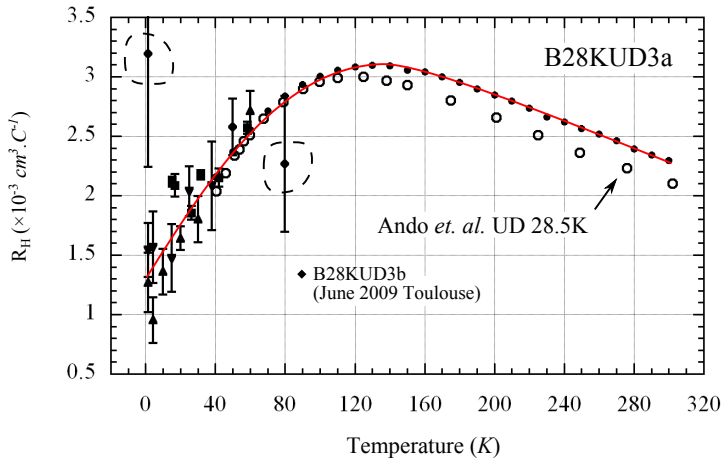


Figure 5.5.3: R_H for underdoped samples of BSCO_{2201} . Plots show results from, • Polo in June 2010, ▲ LNCMI in June 2009, ▼ LNCMI in Feb 2010, ■ Nijmegen in May 2010. Symbols for comparable samples are marked on the plots. Dashed lines indicate points where the field was not sufficient to achieve linear behaviour. Red lines are a guide to the eye.

assignment of the sample B30KUD3 would be more suited to underdoped rather than overdoped.

With reference to the plot in the lower left, the fitted exponents approximately follow the same downward trend with doping as in BSCO_{2201} data from Konstantanović *et al.* [94] up to around $p = 0.27$. In particular the $B = 13 \text{ T}$ follows the curve reasonably closely before the upturn at $p = 0.31$. Downward deviation from the T^2 behaviour at high temperatures (as indicated from a drop in the α exponent) at this point in the phase diagram has been previously interpreted to be due to the saddle point in the DOS which is approaching from below the Fermi energy [95] which would also explain why there is a recovery toward T^2 behaviour between $p = 0.27$ and $p = 0.31$ as the flat portion of the DOS passes above the Fermi energy. This would suggest that the van-Hove singularity peaks in the BSCO_{2201} phase diagram at around $p = 0.25$, approximately where the B16KOD1A sample lies and where the room temperature R_H value was also found to be slightly lower than expected. However this occurs at a higher doping than the Hashimoto paper would suggest [14] (see figure 1.1.6) and given the proximity of the van-Hove singularity, the low Hall coefficient should not be interpreted a simple indicator of carrier density.

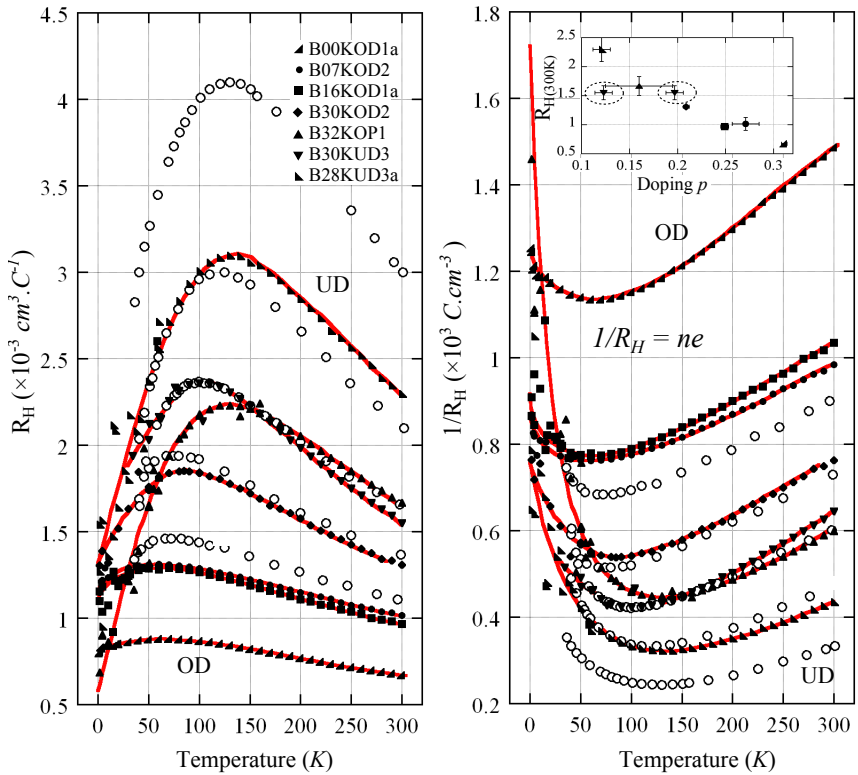


Figure 5.5.4: Hall data in context with data from Ando *et al.* [9] (open circles) which are in order of increasing R_H , 24KOD, 30KOD, 33KOP, 28.5KUD, 20KUD. Right panel shows the inverse hall data which relates to carrier density. Red lines are the same guides to the eye used in previous figures. Inset shows R_H at 300 K plus systematic error bars due primarily to uncertainty in thickness vs. doping scaled to Tl_{2201} data. B30KUD3 (circled) is plotted in both the overdoped and underdoped positions.

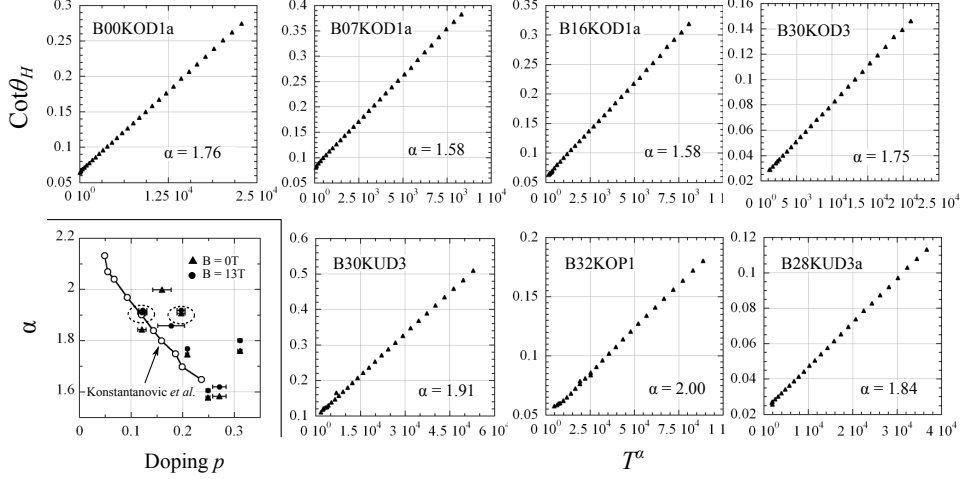


Figure 5.5.5: Hall angle calculated with a nominal field of unity from resistivity data taken in zero field. Plot in bottom left shows the fitted exponent, α , vs. doping compared with similar data on BSCO_{2201} from Konstantanović *et al.* [94] for both zero field resistivity data and resistivity data taken at 13 K ($\cot \theta_H$ plots for $B = 13$ T not shown)

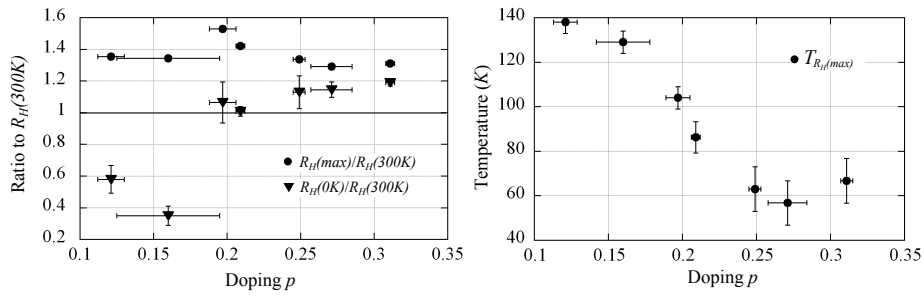


Figure 5.5.6: Left shows ratio of R_H values at the maximum of the Hall curves and at $T = 0\text{ K}$ to the $T = 300\text{ K}$ R_H values. Errors in $R_H(0\text{ K})$ estimated from Hall plots, the value for B30KUD2 is estimated based on linear extrapolation. Right shows the temperature where the maximum R_H occurs.

An alternate explanation based on the Narduzzo paper [70] goes as follows. For $p \gtrsim 0.19$, $R_H(0\text{ K}) > R_H(300\text{ K})$ as illustrated in figure 5.5.6. If we assume there is not temperature dependent change of the Fermi surface such that would affect \mathbf{v}_F , then this can be explained by an temperature dependent change in scattering that preferentially affects one of the two regions of curvature (hole-like or electron-like) on the Fermi surface i.e. a change in anisotropic scattering. As detailed in the introduction, such scattering is thought to originate in the overdoped side of the phase diagram and is seemingly closely tied to superconductivity. The Narduzzo paper explores this possibility but ultimately could not definitively conclude that the scattering rate is proportional to $\cos^2(2\phi)$ as is the case in the Abdel-Jawad paper [96] detailed in the introduction.

To explain the anisotropy in the van-Hove scenario where the change is thought to come about from a change in the carrier numbers, we must surmise that the flat band does not lie at the same energy all around the Fermi surface in order to achieve this anisotropy — in effect this leads to a momentum dependent carrier term. This has been observed in cuprates with Plat   et al. [76] demonstrating in Tl_{2201} a momentum dependence of the energy of the flat region of the bandstructure that range between -25 meV and -40 meV. However, along the (π, π) direction in this case, the van-Hove peak was suppressed suggesting that scattering too is anisotropic.

When we consider the ratio of the maximum R_H to the 300 K value also plotted in figure 5.5.6 then we see that these values do not vary much at all with doping indicating that the scattering process that suppresses the low temperature Hall values only becomes dominant below the temperature where $R_H(\text{max})$ occurs. Moreover we note that the low temperature behaviour of R_H which, although not possible to ascertain for certain due to the scatter in points, appears linear in temperature below $R_H(\text{max})$, which suggests that the same process explored above is T -linear in behaviour.

A final observation is that when the temperatures of the maximums in R_H are plotted in figure 5.5.6, they show a similar doping behaviour to the α fitted exponents.

5.6 Conclusions

High quality crystals of Pb and Sr doped BSCO_{2201} were sourced and studied in the normal state by magnetotransport measurements down to low temperatures, thereby determining the low temperature Hall behaviour. We found evidence that determining the doping in BSCO_{2201} by normalising to a hybrid combination of the Tallon relation for optimal and underdoped samples and to the Tl_{2201} data for overdoped samples gives dopings which are more consistent with the literature.

Two possible scenarios could explain the Hall behaviour in these BSCO_{2201} measurements. The first is the proximity of the van-Hove singularity, the second is an anisotropic scattering rate. The evidence for anisotropy could be explained in the former case by an anisotropy in the saddle point flat regions of the bandstructure, in the latter case the explanation is anisotropy in the scattering rate.

Assuming the latter, some interesting constraints are established for the scattering processes affecting in the Hall coefficient as follows,

1. Preferentially affects the electron or the hole portions of the Fermi surface
2. If it primarily affects the hole portions (along the $k = (\pi, \pi)$ vector), then the temperature dependence of the scattering weakens with doping
3. If it primarily affects the electron portions (along the $k = (\pi, 0)$ vector), then the temperature dependence of the scattering strengthens with doping
4. The scattering process is dominant below the temperature at which $R_H(\max)$ occurs, hardly affecting the data above this temperature
5. The scattering process appears linear in temperature

A natural continuation of this work would include a more precise determination of the low field region to determine with more certainty if the low temperature behaviour is truly T -linear as this would support the notion of an anisotropic parameter. A second possible experiment would be to measure the low temperature Hall in a material where the van-Hove does

not have a significant momentum dependence in order to determine if the low temperature R_H continued to decay down to a level less than the room temperature term.

Bibliography

- [1] J. Custers et al. *Nature* **424** (2003), pp. 524–7. DOI: [10.1038/nature01774](https://doi.org/10.1038/nature01774).
- [2] W. Warren et al. *Physical Review Letters* **62** (1989), pp. 1193–1196. DOI: [10.1103/PhysRevLett.62.1193](https://doi.org/10.1103/PhysRevLett.62.1193).
- [3] S Hüfner et al. *Reports on Progress in Physics* **71** (2008), p. 062501. DOI: [10.1088/0034-4885/71/6/062501](https://doi.org/10.1088/0034-4885/71/6/062501).
- [4] J Tallon. *Physica C: Superconductivity* **349** (2001), pp. 53–68. DOI: [10.1016/S0921-4534\(00\)01524-0](https://doi.org/10.1016/S0921-4534(00)01524-0).
- [5] M. Abdel-Jawad et al. *Nature Physics* **2** (2006), pp. 821–825. DOI: [10.1038/nphys449](https://doi.org/10.1038/nphys449).
- [6] L. Taillefer. *Nature Physics* **2** (2006), pp. 809–810. DOI: [10.1038/nphys478a](https://doi.org/10.1038/nphys478a).
- [7] M. Norman. *Physics* **3** (2010). DOI: [10.1103/Physics.3.86](https://doi.org/10.1103/Physics.3.86).
- [8] R. A. Cooper et al. *Science* **323** (2009), pp. 603–7. DOI: [10.1126/science.1165015](https://doi.org/10.1126/science.1165015).
- [9] Y. Ando and T Murayama. *Physical Review B* **60** (1999), R6991–R6994. DOI: [10.1103/PhysRevB.60.R6991](https://doi.org/10.1103/PhysRevB.60.R6991).
- [10] Y. Ando et al. *Physical Review B* **61** (2000), R14956–R14959. DOI: [10.1103/PhysRevB.61.R14956](https://doi.org/10.1103/PhysRevB.61.R14956).
- [11] C. Torardi et al. *Physical Review B* **38** (1988), pp. 225–231. DOI: [10.1103/PhysRevB.38.225](https://doi.org/10.1103/PhysRevB.38.225).
- [12] D. C. Peets et al. *New Journal of Physics* **9** (2007), pp. 28–28. DOI: [10.1088/1367-2630/9/2/028](https://doi.org/10.1088/1367-2630/9/2/028).
- [13] T. Kondo et al. *Physical Review Letters* **98** (2007), pp. 1–4. DOI: [10.1103/PhysRevLett.98.267004](https://doi.org/10.1103/PhysRevLett.98.267004).
- [14] M. Hashimoto et al. *Physical Review B* **77** (2008), pp. 1–9. DOI: [10.1103/PhysRevB.77.094516](https://doi.org/10.1103/PhysRevB.77.094516).
- [15] J. Bardeen, L. N. Cooper, and J. R. Schrieffer. *Physical Review* **108** (1957), pp. 1175–1204. DOI: [10.1103/PhysRev.108.1175](https://doi.org/10.1103/PhysRev.108.1175).
- [16] J. F. Annett. *Superconductivity, Superfluids and Condensates*. Oxford University Press, 2010, 22ff. ISBN: 978-0-19-850756-7.
- [17] D. Osheroff, R. Richardson, and D. Lee. *Physical Review Letters* **28** (1972), pp. 885–888. DOI: [10.1103/PhysRevLett.28.885](https://doi.org/10.1103/PhysRevLett.28.885).
- [18] J. G. Bednorz and K. A. Müller. *Zeitschrift für Physik B Condensed Matter* **64** (1986), pp. 189–193.

- [19] Y. Kamihara et al. *Journal of the American Chemical Society* **130** (2008), pp. 3296–7. DOI: [10.1021/ja800073m](https://doi.org/10.1021/ja800073m).
- [20] J. F. Annett, N. Goldenfeld, and S. Renn. *Physical Review B* **43** (1991), pp. 2778–2782. DOI: [10.1103/PhysRevB.43.2778](https://doi.org/10.1103/PhysRevB.43.2778).
- [21] D. J. Van Harlingen et al. *Physica C: Superconductivity* **235** (1994), pp. 122–125.
- [22] Y. Wang et al. *Physical Review B* **83** (2011), pp. 4–8. DOI: [10.1103/PhysRevB.83.054509](https://doi.org/10.1103/PhysRevB.83.054509).
- [23] O. M Froehlich et al. *Europhysics Letters* **36** (1996), pp. 467–472. DOI: [10.1209/epl/i1996-00253-5](https://doi.org/10.1209/epl/i1996-00253-5).
- [24] L. Boeri, O. V. Dolgov, and a. a. Golubov. *Physical Review Letters* **101** (2008), pp. 1–4. DOI: [10.1103/PhysRevLett.101.026403](https://doi.org/10.1103/PhysRevLett.101.026403).
- [25] I. I. Mazin et al. *Physical Review Letters* **101** (2008), pp. 1–4. DOI: [10.1103/PhysRevLett.101.057003](https://doi.org/10.1103/PhysRevLett.101.057003).
- [26] K. Haule, J. H. Shim, and G. Kotliar. *Physical Review Letters* **100** (2008), pp. 3–6. DOI: [10.1103/PhysRevLett.100.226402](https://doi.org/10.1103/PhysRevLett.100.226402).
- [27] S. Jiang et al. *Journal of Physics: Condensed Matter* **21** (2009), p. 382203. DOI: [10.1088/0953-8984/21/38/382203](https://doi.org/10.1088/0953-8984/21/38/382203).
- [28] S. Kasahara et al. *Physical Review B* **81** (2010), pp. 1–5. DOI: [10.1103/PhysRevB.81.184519](https://doi.org/10.1103/PhysRevB.81.184519).
- [29] K. Hashimoto et al. *Physical Review Letters* **108** (2012), pp. 1–5. DOI: [10.1103/PhysRevLett.108.047003](https://doi.org/10.1103/PhysRevLett.108.047003).
- [30] Y Zhang et al. *Nature Materials* **10** (2011), pp. 273–7. DOI: [10.1038/nmat2981](https://doi.org/10.1038/nmat2981).
- [31] H. Ding et al. *Europhysics Letters* **83** (2008), p. 47001. DOI: [10.1209/0295-5075/83/47001](https://doi.org/10.1209/0295-5075/83/47001).
- [32] K Terashima et al. *Proceedings of the National Academy of Sciences* **106** (2009), pp. 7330–3. DOI: [10.1073/pnas.0900469106](https://doi.org/10.1073/pnas.0900469106).
- [33] J. Fletcher et al. *Physical Review Letters* **102** (2009), pp. 1–4. DOI: [10.1103/PhysRevLett.102.147001](https://doi.org/10.1103/PhysRevLett.102.147001).
- [34] X Qiu et al. *arxiv.org* (2011), p. 4. eprint: [1106.5417](https://arxiv.org/abs/1106.5417).
- [35] C.-L. Song et al. *Science* **332** (2011), pp. 1410–3. DOI: [10.1126/science.1202226](https://doi.org/10.1126/science.1202226).
- [36] J. K. Dong et al. *Physical Review Letters* **104** (2010), pp. 1–4. DOI: [10.1103/PhysRevLett.104.087005](https://doi.org/10.1103/PhysRevLett.104.087005).
- [37] Y. Zhang et al. *Nature Physics* **8** (2012), pp. 371–375. DOI: [10.1038/nphys2248](https://doi.org/10.1038/nphys2248). eprint: [1109.0229](https://arxiv.org/abs/1109.0229).

- [38] M. Yamashita et al. *Physical Review B* **84** (2011), pp. 1–4. DOI: 10.1103/PhysRevB.84.060507.
- [39] K. Suzuki, H. Usui, and K. Kuroki. *Journal of the Physical Society of Japan* **80** (2011), p. 013710. DOI: 10.1143/JPSJ.80.013710.
- [40] Y. J. Uemura. *Nature Physics* **8** (2009), pp. 253–255.
- [41] N. Berk and J. Schrieffer. *Physical Review Letters* **17** (1966), pp. 433–435. DOI: 10.1103/PhysRevLett.17.433.
- [42] D. Scalapino. *Physics Reports* **250** (1995), pp. 329–365. DOI: 10.1016/0370-1573(94)00086-I.
- [43] J. Paglione and R. L. Greene. *Nature Physics* **6** (2010), pp. 645–658. DOI: 10.1038/nphys1759.
- [44] Y. Nakai et al. *Physical Review Letters* **105** (2010), pp. 31–34. DOI: 10.1103/PhysRevLett.105.107003.
- [45] T. Yamazaki et al. *Physical Review B* **81** (2010), pp. 1–5. DOI: 10.1103/PhysRevB.81.224511.
- [46] E. Colombier et al. *Physical Review B* **79** (2009), pp. 1–9. DOI: 10.1103/PhysRevB.79.224518.
- [47] P. L. Alireza et al. *Journal of Physics: Condensed Matter* **21** (2009), p. 012208. DOI: 10.1088/0953-8984/21/1/012208.
- [48] L. E. Klintberg et al. *Journal of the Physical Society of Japan* **2** (2010), p. 5. DOI: 10.1143/JPSJ.79.123706. eprint: 1009.2716.
- [49] H. Shishido et al. *Physical Review Letters* **104** (2010), pp. 1–4. DOI: 10.1103/PhysRevLett.104.057008.
- [50] C. van der Beek et al. *Physical Review Letters* **105** (2010), pp. 4–7. DOI: 10.1103/PhysRevLett.105.267002.
- [51] J. G. Analytis et al. *Physical Review Letters* **105** (2010), pp. 1–4. DOI: 10.1103/PhysRevLett.105.207004.
- [52] J. G. Analytis et al. *Physical Review Letters* **103** (2009), pp. 1–4. DOI: 10.1103/PhysRevLett.103.076401.
- [53] T. Kondo et al. *Physical Review B* **81** (2010), pp. 1–4. DOI: 10.1103/PhysRevB.81.060507.
- [54] T. Terashima et al. *Physical Review Letters* **107** (2011), pp. 1–5. DOI: 10.1103/PhysRevLett.107.176402. eprint: 1103.3329.
- [55] J. G. Analytis et al. *Physical Review B* **80** (2009). DOI: 10.1103/PhysRevB.80.064507. eprint: 0902.1172.
- [56] D. Schoenberg. *Magnetic oscillations in metals*. Cambridge University Press, 1984. ISBN: 978-0-521-11878-1.

- [57] N. Ashcroft and N. Mermin. *Solid State Physics*. Thomson Learning, 1976. ISBN: 0-03-083993-9.
- [58] S. Blundell. *Magnetism in Condensed Matter*. Oxford University Press, 2001.
- [59] P. M. C. Rourke et al. *New Journal of Physics* **12** (2010), p. 105009. DOI: 10.1088/1367-2630/12/10/105009.
- [60] T. Moriya. *Spin fluctuations in itinerant electron magnetism*. Springer Verlag, 1985, 25 ff. ISBN: 3-540-15422-1.
- [61] M Dressel and G Gruner. *Electrodynamics Of Solids*. Cambridge University Press, 2002, p. 126. ISBN: 0 521 59726 9.
- [62] M. Luders. *Electrons In Solids*. 2010.
- [63] K. Burke. *The ABC of DFT*. 2003.
- [64] P. Hohenberg. *Physical Review* **136** (1964), B864–B871. DOI: 10.1103/PhysRev.136.B864.
- [65] M. Levy. *Proceedings of the National Academy of Sciences* **76** (1979), pp. 6062–6065. DOI: 10.1073/pnas.76.12.6062.
- [66] C. G. Broyden. *Mathematics of Computation* **19** (1965), p. 577. DOI: 10.2307/2003941.
- [67] J. P. Perdew, K. Burke, and M. Ernzerhof. *Physical Review Letters* **77** (1996), pp. 3865–3868. DOI: 10.1103/PhysRevLett.77.3865.
- [68] J. P. Perdew and W. Yue. *Physical Review B* **33** (1986), pp. 8800–8802. DOI: 10.1103/PhysRevB.33.8800.
- [69] O. K. Andersen. *Physical Review B* **12** (1975), pp. 3060–3083. DOI: 10.1103/PhysRevB.12.3060.
- [70] a. Narduzzo et al. *Physical Review B* **77** (2008), pp. 4–7. DOI: 10.1103/PhysRevB.77.220502.
- [71] T Kondo et al. *Journal of Electron Spectroscopy and Related Phenomena* **137-140** (2004), pp. 663–668. DOI: 10.1016/j.elspec.2004.02.104.
- [72] C. M. J. Andrew. “The Fermi surface of iron pnictides”. PhD thesis. University of Bristol, 2010.
- [73] P Blaha et al. *WIEN2K, An Augmented Plane Wave + Local Orbitals Program for Calculating Crystal Properties*. Karlheinz Schwarz Techn. Universitat, 2001. ISBN: 3-9501031-1-2.
- [74] T. Chien, Z. Wang, and N. Ong. *Physical Review Letters* **67** (1991), pp. 2088–2091. DOI: 10.1103/PhysRevLett.67.2088.
- [75] M. Presland et al. *Physica C: Superconductivity* **176** (1991), pp. 95–105. DOI: 10.1016/0921-4534(91)90700-9.

- [76] M. Platé et al. *Physical Review Letters* **95** (2005), p. 077001. DOI: 10.1103/PhysRevLett.95.077001.
- [77] P. M. C. Rourke et al. *New Journal of Physics* **12** (2010), p. 4. DOI: 10.1088/1367-2630/12/10/105009. eprint: 1005.0573.
- [78] M. Rotter, C. Hieke, and D. Johrendt. *Physical Review B* **82** (2010), pp. 1–7. DOI: 10.1103/PhysRevB.82.014513. eprint: arXiv:1005.1411v2.
- [79] A Mewis. *Z. Naturforsch* **35b** (1980), p. 141.
- [80] A. Carrington et al. *Physica C: Superconductivity* **469** (2009), pp. 459–468. DOI: 10.1016/j.physc.2009.03.045.
- [81] A. Coldea et al. *Physical Review Letters* **103** (2009), pp. 1–4. DOI: 10.1103/PhysRevLett.103.026404.
- [82] T. Yoshida et al. *Physical Review Letters* **106** (2011), p. 4. DOI: 10.1103/PhysRevLett.106.117001. eprint: 1008.2080.
- [83] R. Mittal et al. *Physical Review B* **83** (2011), pp. 1–11. DOI: 10.1103/PhysRevB.83.054503.
- [84] C. Bergemann et al. *Physical Review Letters* **84** (2000), pp. 2662–5.
- [85] L. Ortenzi et al. *Physical Review Letters* **103** (2009), pp. 1–4. DOI: 10.1103/PhysRevLett.103.046404.
- [86] W. D. Wise et al. *Nature Physics* **5** (2009), pp. 213–216. DOI: 10.1038/nphys1197.
- [87] W. D. Wise et al. *Nature Physics* **4** (2008), pp. 696–699. DOI: 10.1038/nphys1021.
- [88] T. Kondo et al. *Physical Review B* **72** (2005), pp. 1–9. DOI: 10.1103/PhysRevB.72.024533.
- [89] T. Kondo et al. *Nature Physics* **7** (2010), pp. 21–25. DOI: 10.1038/nphys1851.
- [90] T. Kondo et al. *Nature* **457** (2009), pp. 296–300. DOI: 10.1038/nature07644.
- [91] T. Kondo et al. *Physical Review B* **74** (2006), pp. 1–9. DOI: 10.1103/PhysRevB.74.224511.
- [92] Z. Konstantinović, Z. Li, and H. Raffy. *Physica C: Superconductivity* **351** (2001), pp. 163–168. DOI: 10.1016/S0921-4534(00)01733-0.
- [93] S. Ono et al. *Physical Review Letters* **85** (2000), pp. 638–641. DOI: 10.1103/PhysRevLett.85.638.
- [94] Z. Konstantinović, Z. Li, and H. Raffy. *Physical Review B* **62** (2000), R11989–R11992. DOI: 10.1103/PhysRevB.62.R11989.

- [95] Y. Ando et al. *Physical Review Letters* **92** (2004), pp. 13–16. DOI: [10.1103/PhysRevLett.92.197001](https://doi.org/10.1103/PhysRevLett.92.197001).
- [96] M. Abdel-Jawad et al. *Physical Review Letters* **99** (2007), pp. 10–13. DOI: [10.1103/PhysRevLett.99.107002](https://doi.org/10.1103/PhysRevLett.99.107002).

Appendix A

‘Microfit’ parameters

Angle (deg.)	Band	Frequency (T)	Fit Periods	Filter Range	Notes
12	α_1	1210	1.5	1100–1240	
28	α_1	1269	1.5	1200–1310	
46	α_1	1532	1.5	1430–1585	
12	α_2	1372	1.5	1320–1440	
28	α_2	1530	1.5	1450–1650	
46	α_2	2017	1.5	1970–2100	
28	β_2	1365	1.5	1320–1440	
12	β_1	2180	1.5	2100–2270	
12	β_2	2500	1.5	2450–2550	
28	β_2	2605	1.5	2555–2670	
46	β_2	3347	1.5	3250–3370	Twinned peak
46	β_2	3381	1.5	3365–2500	Twinned peak
12	β_3	2350	1.5	2270–2450	
28	β_3	2475	1.5	2400–2560	
46	β_3	2970	1.5	2850–3100	
12	δ	1270	1.5	1250–1310	
46	δ	1626	1.5	1590–1690	
28	γ_1	912	1.5	850–970	
46	γ_1	1320	1.5	1270–1370	
46	γ_2	4497	1.5	4400–4600	

Appendix B

Lindhard susceptibility calculation code

The following is MATLAB code known to run on release 2008b.

```
function [ total_re_x0 total_im_x0 ] = calc_x0( fs , T, delta , omega, ...
q_space , energy_ind_combs , out_filestem )

% A function to calculate the non-interacting susceptibility according to
% the Lindhard function. Matrix elements are assumed to be unity.
%
% energy_ind_combs: Optional Nx2 matrix of band pairs (default: empty,
% All band pairs are calculated)
% temperature: Temperature (default: Absolute zero - slightly
% quicker to calculate)
% delta: Quasiparticle lifetime, if zero this will give
% zero for the imaginary portion of the
% susceptibility (default: zero)
% omega: Perturbation frequency (default: zero)
% out_filestem: Filestem for all the individual band combinations
% Default: 'x0'
% q_space: Indices of Q space to calculate passed as a cell array
% of 3 vectors, first for the Qx indices, second
% for the Qy indices, third for the Qz indices. An
% empty cell array or an empty vector in the cell
% array defaults to the full extent of grid of energy
% points. N.B. Since we are dealing with indices,
% not k-space values, 1 corresponds to a zero
% in q-space (i.e. qx = (n-1)*dk_x where n is the
% number passed)
%
% RETURNS:
% re_x0: Real values of x0
% im_x0: Im values of x0
%

% Use to test the code. Generates free electron energy dispersion and
% calculates a susceptibility. Actually not straightforward since free
% electron dispersion is not periodic.
TEST_FREE_ELECTRON = false ;
DIMENSIONS = 3;

if TEST_FREE_ELECTRON
```

```

clear fs;
free_electron_dispersion = @(kx, ky, kz) (kx.^2 + ky.^2 + kz.^2);
delta = 1e-9;
omega = 1e-9;
MAX_L = 1;
MIN_L = -1;
NUM PTS = 100;
fs.dL = (MAX_L - MIN_L) / (NUM PTS - 1);
fs.FermiLevel = 0.09;
L = linspace(MIN_L, MAX_L, NUM PTS);
if DIMENSIONS == 3
    [fs.cartX, fs.cartY, fs.cartZ] = meshgrid(L, L, L);
    q_space = {[[], [], []]};
    % Calculate distance each grid point is from centre in order
    % to build the symmetry mask
    [x y z] = meshgrid(1:NUM PTS, 1:NUM PTS, 1:NUM PTS);
    r = hypot(hypot(x - NUM PTS ./ 2, y - NUM PTS ./ 2), ...
        z - NUM PTS ./ 2);
elseif DIMENSIONS == 2
    [fs.cartX, fs.cartY, fs.cartZ] = meshgrid(L, L, 0);
    q_space = {[[], [], 1]};
    [x y] = meshgrid(1:NUM PTS, 1:NUM PTS);
    r = hypot(x - NUM PTS ./ 2, y - NUM PTS ./ 2);
else
    error('Number_of_dimensions_not_supported');
end
% Symmetry mask based on Fermi function, ensures that the
% symmetry is spherical for the non-repeating free-electron case
MASK_TRIM = 1.5;
MASK_DECAY = 10;
sym_mask = 1 ./ (exp((r - (NUM PTS ./ 2 - MASK_TRIM)) ...
    * MASK_DECAY) + 1);
fs.cartE = {};
fs.cartE{1} = free_electron_dispersion(fs.cartX, fs.cartY, ...
    fs.cartZ);
end

% Set the temperature
if isempty(T)
    T = 0;
end
disp(sprintf('Temperature_set_to: %.3f', T));

% Set the lifetime
if isempty(delta)
    delta = 0;
end
disp(sprintf('Quasiparticle_lifetime_set_to: %.3f', delta));

% Set omega
if isempty(omega)
    omega = 0;
end

```

```

disp(sprintf('Plasma_frequency_set_to : %.3f', omega));

% Set the output filestem
if isempty(out_filestem)
    out_filestem = 'x0';
end
disp(['Filestem_set_to : ' out_filestem]);

% Set the size of the Q region to be calculated
[num_qx num_qy num_qz] = size(fs.cartE{1});
if isempty(q_space)
    q_space = {[[] [] []]};
end
if isempty(q_space{1})
    qx_range = 1:num_qx;
else
    qx_range = q_space{1};
end
if isempty(q_space{2})
    qy_range = 1:num_qy;
else
    qy_range = q_space{2};
end
if isempty(q_space{3})
    qz_range = 1:num_qz;
else
    qz_range = q_space{3};
end
disp(sprintf('Size_of_q_space_is : %dx%dx%d', num_qx, num_qy, num_qz));

% Set the combinations of bands to be calculated
% Replace if necessary
if isempty(energy_ind_combs)
    % Compile a list of combinations of the bands in terms of indices
    n = length(fs.cartE);
    energy_ind_combs = zeros([n 2]);
    i = 0;
    for ind1 = 1:n
        for ind2 = 1:n
            i = i + 1;
            energy_ind_combs(i,1) = ind1;
            energy_ind_combs(i,2) = ind2;
        end
    end
end
disp('Band_combinations_to_be_calculated_and_summed_over : ');
disp(energy_ind_combs);

%K_BOLTZ = 1.3806503e-23;
K_BOLTZ = 6.3336e-6; % In Rydbergs

total_im_x0 = zeros(num_qx, num_qy, num_qz);
total_re_x0 = zeros(num_qx, num_qy, num_qz);

```

```

% This will be 'Inf' if T=0 but will not be used later if this is
% the case
beta = 1 ./ (K_BOLTZ .* T);

for inds = energy_ind_combs'
    % Assign the two coupled bands to be calculated
    energies = fs.cartE{inds(1)};
    q_energies = fs.cartE{inds(2)};
    % Initialise the results matrices
    im_x0 = zeros(num_qx, num_qy, num_qz);
    re_x0 = zeros(num_qx, num_qy, num_qz);
    % Iterate over all Q vectors
    for k = qz_range
        for j = qy_range
            disp(sprintf('Bands %d->%d: _k=%d\ tj=%d', inds', k, j));
            for i = qx_range
                % Determine the energies at k+Q
                if TEST_FREE_ELECTRON
                    qx = (i - 1) .* fs.dL;
                    qy = (j - 1) .* fs.dL;
                    qz = (k - 1) .* fs.dL;
                    energies_prime = free_electron_dispersion(fs.cartX ...
                        + qx, fs.cartY + qy, fs.cartZ + qz);
                else
                    energies_prime = circshift(q_energies, [i - 1, ...
                        j - 1, k - 1]);
                end
                % x0 (non-interacting susceptibility) is of form
                % A / (B + iC)
                % Re(x0) is of form AB / (B^2 + C^2)
                % Im(x0) is of form -CA / (B^2 + C^2)

                % Quicker approximation for T=0 that also avoids Inf in
                % calculation
                if T == 0
                    A = (energies <= fs.FermiLevel) - (energies_prime ...
                        <= fs.FermiLevel);
                else
                    A = 1 ./ (exp(beta) .* (energies - fs.FermiLevel)) ...
                        + 1 ) - 1 ./ (exp(beta) .* (energies_prime - ...
                        fs.FermiLevel)) + 1 );
                end

                B = energies_prime - energies - omega;
                C = delta; % Is -delta in formula, but this is cancelled
                % by a negative when finally calculating Im(x0)

                D = A ./ (B.^2 + C.^2);

                im_result = C .* D;
                re_result = B .* D;

                % Remove NaNs (usu. from 0/0 operations)

```

```

im_result(isnan(im_result)) = 0;
re_result(isnan(re_result)) = 0;

if TEST_FREE_ELECTRON
    im_result = im_result .* sym_mask;
    re_result = re_result .* sym_mask;
end

im_x0(i, j, k) = sum(im_result (:));
re_x0(i, j, k) = sum(re_result (:));
end
end
% Save this band pair data individually before combining with overall
% x0
save(sprintf([out_filestem '_Bands=%d-%d'], inds), 're_x0', 'im_x0');
total_im_x0 = total_im_x0 + im_x0;
total_re_x0 = total_re_x0 + re_x0;
end
end

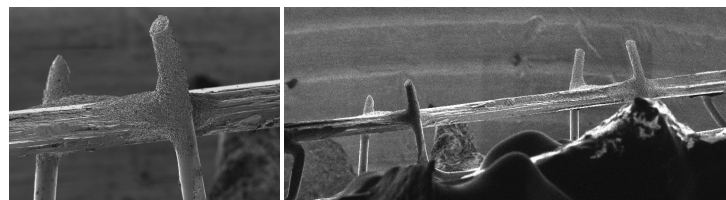
```


Appendix C

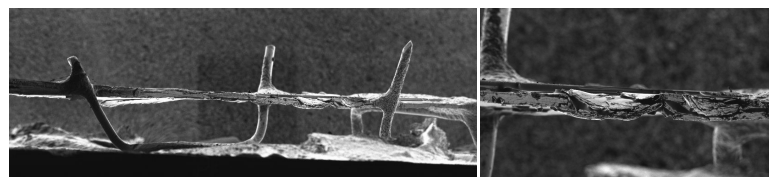
FIB scans

Exemplary images from the FIB scans performed with the help of Dr. P. Heard.

B00KOD1a



B07KOD2



B16KOD1a



B30KOD3

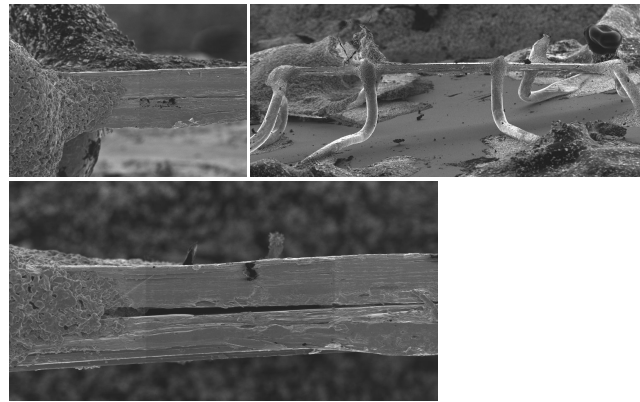


Figure C.0.1

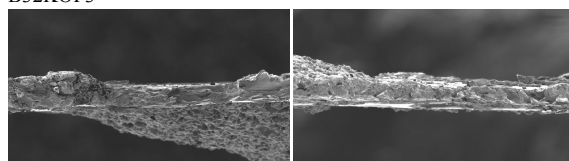
B30KOD2



B32KOP1



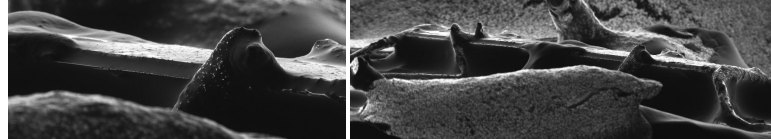
B32KOP3



B32KOP4



B28KUD3a



B28KUD3b

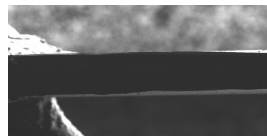


Figure C.0.2